

Managing Coastal Aquifers in Selected Pacific SIDS (MCA Project)

Development of a numerical groundwater model to assist with groundwater management in Laura, Majuro Atoll, Republic of Marshall Islands

Tybaud Goyetche, María Pool, Jordi Guimerà and Elena Abarca



22/03/2024

Final Report

Version 1

◆ 3586_PC_Marshall_Model_A21_IF_v1 ◆

In bibliography, this report will be cited as follows:

Tybaud Goyetche, María Pool, Jordi Guimerà and Elena Abarca (2024) Development of a numerical groundwater model to assist with groundwater management in Laura, Majuro Atoll, Republic of Marshall Islands. Report code: 3586_PC_Marshall_Model_A21_IF_v1

Amphos 21 Consulting S.L.

C. Veneçuela, 103, 08019 Barcelona (Spain)

+34 935 830 500

www.amphos21.com

Prepared by	Reviewed by	Validated by
Tybaud Goyetche María Pool	Elena Abarca	Elena Abarca

Index

Executive summary	15
1 Introduction	20
1.1 Background	20
1.2 Objectives.....	20
2 Collection and analysis of information	21
2.1 Documents and data	21
2.2 Meteorological data.....	21
2.3 Sea-level.....	23
2.4 Monitoring wells.....	24
2.5 Abstractions.....	25
2.6 Resistivity profiles.....	27
2.7 Topobathymetric elevation	29
2.8 Review of previous studies	30
3 Conceptual model	31
3.1 Study area	31
3.2 Geological features	32
3.3 Sea-level temporal series.....	33
3.4 Recharge estimation	33
3.5 Abstractions.....	35
3.6 Tidal analysis and filtering.....	39
3.6.1 Data filtering:	39
3.6.2 Time shift determination.....	40
3.6.3 Tidal efficiency (TE) or damping	41

3.6.4	Hydraulic diffusivity	42
3.7	Hydraulic and transport parameters	46
3.8	Freshwater lens and piezometry.....	46
3.9	Water balance	48
4	Numerical model	49
4.1	Methodology.....	49
4.2	Numerical code	50
4.3	Geometry.....	50
4.4	Spatial and temporal discretization.....	51
4.5	Boundary conditions.....	53
4.5.1	Recharge.....	53
4.5.2	Connection with the ocean and lagoon	54
4.5.3	Bottom of the model.....	56
4.5.4	Abstractions.....	56
4.6	Parametrization	57
4.7	Initial conditions.....	58
4.8	Observations wells	58
5	Numerical calibration.....	59
5.1	Quasi-Steady State calibration	59
5.2	Transient calibration.....	61
5.2.1	Hourly Transient Model.....	61
5.2.2	Daily Transient Model	63
5.3	Calibrated parameters.....	67
6	Sensitivity analysis	69

6.1	Hydraulic conductivity	69
6.1.1	Upper Sediments.....	70
6.1.2	Lower Sediments.....	72
6.1.3	Lower Limestones	73
6.2	Seepage conductance	74
6.3	Dispersion.....	75
6.4	Porosity.....	77
6.5	Abstractions.....	79
6.6	Summary	83
7	Simulation of predictive scenarios	84
7.1	Drought recovery.....	87
7.1.1	Scenarios description.....	87
7.1.2	Effect on the freshwater lens volume and recovery	90
7.1.3	Effect and recovery on pumping wells	93
7.2	Sea-level rise (SLR)	99
7.2.1	Scenario description.....	99
7.2.2	Impact of SLR.....	100
7.3	Inundation events.....	103
7.3.1	Scenario description.....	103
7.3.2	Effect on the freshwater lens volume and recovery	105
7.3.3	Effect and recovery in pumping wells	109
7.4	Scenarios main conclusions	111
8	Management strategies and conclusions	120
8.1	To drought.....	120

8.2	To Sea Level Rise	120
8.3	To inundation events	121
8.4	Other improvements	121
9	References	122
A.	Conceptual Model	125
A.1	Monitoring wells	125
A.2	Recharge estimation	129
A.3	Hydraulic Parameters	130
B.	Numerical Model.....	131
B.1	Governing Equations.....	131
B.2	Pumping wells	133
B.3	Observation wells	133
C.	Model Calibration	135
C.1	Daily Transient Model	135

List of Tables

Table 2-1: Meteorological data available at Laura and Majuro Airport	22
Table 2-2: Tide gauge data available at Majuro	24
Table 2-3: Available pumping data	26
Table 2-4: Previous studies extractible information.....	30
Table 3-1: Soil parameters used to perform the daily water balance in the soil.	34
Table 3-2: Components of the water balance and their corresponding values derived from various studies found in the literature. Data presented in mm/yr for the considered period.	35
Table 3-3: Pumping (m ³ /d) for water-supply wells in the Laura area.	36
Table 3-4: Hydraulic diffusivity derivation from tidal analysis at monitoring wells.	44
Table 3-5: Freshwater lens volume.	48
Table 4-1: Period and maximum time step for the different transient simulations.....	52
Table 4-2: Initial horizontal and vertical permeabilities and porosity implemented in the numerical model.....	57
Table 5-1: Calibration statistics for the calibration of the Daily Transient Model.....	66
Table 5-2: Values of initial and calibrated model parameters.	69
Table 6-1: Freshwater lens volume and relative change when increasing pumping rates.....	79
Table 6-2: Pumping rates considered and resulting electrical conductivity for each well. The grey colour indicates when salinity exceeds the drinking water limit.	80
Table 6-3: Summary of sensitivity analysis effect.	84
Table 7-1: Summary of future scenarios with the main variations included in each simulation.	86
Table 7-2: Inundation scenarios.	104
Table 7-3: Summary of futures simulation scenarios results: Volume of the freshwater lens.	114

Table 7-4: Summary of futures simulation scenarios results: Salinity at the pumping wells. 116

Table 9-1: Monitoring wells short term data for the HYCOS campaign..... 125

Table 9-2: Monitoring wells long term data for the HYCOS campaign 126

Table 9-3: Monitoring wells data for the MCAP campaign 126

Table 9-4: Counts of manual measurements and measured parameters. 127

Table 9-5: Hydraulic and transport parameters extracted from the literature. 130

Table 9-6: Pumping wells coordinates and pumping rates considered for the steady state simulation. 133

Table 9-7: Observation wells details..... 133

List of Figures

Figure 2-1: Temperature at Majuro Airport (1950 - 2023).....	22
Figure 2-2: Climograph of Majuro. Average data over 64 years (1951-2023).....	23
Figure 2-3: Annual rainfall deviation from the mean rainfall.....	23
Figure 2-4: Map of monitoring wells and pumping wells.	25
Figure 2-5: Electrical Resistivity Tomography profiles	28
Figure 2-6: One-meter topobathymetric elevation map of Majuro.	29
Figure 2-7: Topobathymetric elevation (m) around Laura Island.....	30
Figure 3-1: Location of Laura, Majuro (RMI).	31
Figure 3-2: Geological features of Laura Island (Hamlin and Anthony, 1987).....	32
Figure 3-3: Completed daily temporal evolution of sea-level from 2007 to 2022.	33
Figure 3-4: Yearly calculated recharge.....	35
Figure 3-5: 2007 temporal evolution of abstractions.....	38
Figure 3-6: 2016 temporal evolution of abstractions.....	¡Error! Marcador no definido.
Figure 3-7: Resulting time series from Python code application at monitoring well 3-38B. ...	40
Figure 3-8: Tidal harmonics identified in the sea and monitoring well 3-38B.	40
Figure 3-9: Measured level at Sea and MW3-18 and identified highest correlation for lag determination.....	41
Figure 3-10: Example of tidal efficiency analysis, (a) Synchronized Sea level and MW3-28 series. (b) Distribution of tidal efficiency frequencies.	42
Figure 3-11: Distance from the coast.....	43
Figure 3-12: Hydraulic conductivity calculated from Dh with a specific storage of 1e-5.....	45
Figure 3-13: Plan view of the freshwater lens thickness.	47
Figure 3-14: Hydrogeological conceptual model of Laura Island freshwater lens.....	48

Figure 4-1: (Left) Majuro Atoll and Laura at the western end, and (Right) model domain. 51

Figure 4-2: Recharge zonation defined in the numerical model. Zone 2 considers a decreased recharge with a reduction of 10%. 53

Figure 4-3: Daily head records at piezometer 1-43 (red dots), daily average sea level (black line) and estimated recharge (green line) for the period from 01/09/2008 to 15/12/2008. 54

Figure 4-4: Boundary condition to represent the contact with the ocean and lagoon. 55

Figure 4-5: Head responses to tidal oscillations observed during the HYCOS campaign showing the existence of upward vertical gradients. 58

Figure 5-1: Cross sections showing the electrical conductivity inferred from the geophysical profiles (solid lines) and results from the numerical model (dashed lines). 60

Figure 5-2: (left) Head distribution obtained from the numerical model and (right) the one defined for April 1973 by Hamlin and Anthony (1987). 61

Figure 5-3: Calculated (blue line) and measured (red dots) normalized heads at eight selected shallow multi-level observation wells from the calibrated Hourly Transient Model. 62

Figure 5-4: Modelled versus observed heads (top) and frequency distribution of the residuals (bottom) for the calibrated Daily Transient Model. 64

Figure 5-5: Modelled versus observed concentrations (top) and frequency distribution of the residuals (bottom) for the calibrated Daily Transient Model. 65

Figure 5-6: Spatial distribution of the horizontal permeability obtained from the calibration process of the Daily Transient Model. 68

Figure 6-1: Vertical salinity profile in the central part of Laura (Hydraulic conductivity sensitivity analysis). White lines represent 5% and 50% seawater isoconcentration contours. First column corresponds to the upper sediments, the second to the lower sediments, and the third to the lower limestone layer. The calibrated model is presented in the fourth column. Results for decreased ($K/2$) and increased ($K*2$) hydraulic conductivity is shown in the first and second rows, respectively. 71

Figure 6-2: Vertical cross section showing the isoconcentration contours of 5% (dotted lines) and 50% (solid lines) of seawater in the central part of Laura Island for the calibrated model (black lines), increasing the permeability of the Upper Sediments (red lines) and decreasing the permeability (green lines). 72

Figure 6-3: Vertical cross section showing the isoconcentration contours of 5% (dotted lines) and 50% (solid lines) of seawater in the central part of Laura Island for the calibrated model (black lines), increasing the permeability of the Lower Sediments (red lines) and decreasing the permeability (green lines)..... 73

Figure 6-4: Vertical cross section showing the isoconcentration contours of 5% (dotted lines) and 50% (black lines) of seawater in the central part of Laura Island for the calibrated model (black lines), increasing the permeability of the Lower Limestones (red lines) and decreasing the permeability (green lines)..... 74

Figure 6-5: Seepage conductance impact over discharge..... 75

Figure 6-6: Vertical salinity profile in the central part of Laura Island (Dispersion sensitivity analysis). White lines represent 5% and 50% seawater isoconcentration contours. 76

Figure 6-7: Vertical cross section showing the isoconcentration contours of 5% and 50% of seawater in the central part of Laura Island for the calibrated model (black lines), increasing the dispersion (red lines) and decreasing the dispersion (green lines)..... 77

Figure 6-8: Simulated concentration for porosity sensitivity analysis. 78

Figure 6-9: Porosity and freshwater lens volume. 79

Figure 6-10: Concentration distribution obtained for the Sensitivity analysis of the abstractions considering a multiplier factor of 1.2, 1.5 and 1.75..... 81

Figure 6-11: Concentration distribution obtained for the Sensitivity analysis of the abstractions considering a multiplier factor of 2.5, 5 and 10..... 82

Figure 7-1: Deviation from monthly rainfall historic data from 1980 to 2022. Months above the monthly average rainfall are indicated in blue, while those below average are in red. Grey shaded part indicates the reference drought from Dec-1982 to Nov 1984..... 88

Figure 7-2: Drought scenarios recharge series. (a) Scenario A: Dry recovery; (b) Scenario B: Average recovery; (c) Scenario C: Double drought. Dotted blue represents the reference case, with no modification in the recharge. 89

Figure 7-3: Freshwater lens volume in response to drought scenarios. (a) Scenario A1: Dry recovery; (b) B1: Average recovery; (c) C1: Double drought..... 91

Figure 7-4: Freshwater lens volume recovery and recharge. 92

Figure 7-5: Freshwater lens volume in response to drought scenarios with abstraction increased. (a) Scenario A: Dry recovery; (b) Scenario B: Average recovery; (c) Scenario C: Double drought. Increased abstraction scenarios are represented by red dashed lines. 93

Figure 7-6: Pumping wells response to Scenario A1: Dry recovery. The grey lines on the secondary y-axis represent abstraction and the red dashed line the 2500 $\mu\text{S}/\text{cm}$ limit. 94

Figure 7-7: Pumping wells response to Scenario B1: Average recovery. The grey lines on the secondary y-axis represent abstraction and the red dashed line the 2500 $\mu\text{S}/\text{cm}$ limit. 95

Figure 7-8: Pumping wells response to Scenario C1: Double drought. The grey lines on the secondary y-axis represent abstraction and the red dashed line the 2500 $\mu\text{S}/\text{cm}$ limit. 96

Figure 7-9: Pumping wells response to Scenario A2: Dry recovery. The grey lines on the secondary y-axis represent abstraction and the red dashed line the 2500 $\mu\text{S}/\text{cm}$ limit. 97

Figure 7-10: Pumping wells response to Scenario B2: Average recovery. The grey lines on the secondary y-axis represent abstraction and the red dashed line the 2500 $\mu\text{S}/\text{cm}$ limit. 98

Figure 7-11: Pumping wells response to Scenario C2: Double drought. The grey lines on the secondary y-axis represent abstraction and the red dashed line the 2500 $\mu\text{S}/\text{cm}$ limit. 99

Figure 7-12: Freshwater lens volume in response to drought scenarios. (a) Sea-level used for SLR scenarios. (b) Recharge used for SLR scenarios (c) Freshwater lens volume for the four SLR scenarios and the referenced case (dashed blue line) for comparison. 100

Figure 7-13: Water ponding areas with the water table above topography. 101

Figure 7-14: Vertical profile in the central part of Laura Island. 101

Figure 7-15: Pumping wells response to SLR scenarios. The grey lines on the secondary y-axis represent abstraction and the red dashed line the 2500 $\mu\text{S}/\text{cm}$ limit. 102

Figure 7-16: Map of inundation height. 104

Figure 7-17: Recharge during inundations scenarios. 104

Figure 7-18: Freshwater lens volume in response to inundation scenarios in wet conditions. (a) Recharge used for scenarios (b) Freshwater lens volume. 105

Figure 7-19: Vertical salinity profile in the central part of Laura Island at different times after the storm surge in wet conditions. 106

Figure 7-20: Freshwater lens volume in response to inundation scenarios in dry conditions. (a) Recharge used for scenarios (b) Freshwater lens volume..... 107

Figure 7-21: Vertical salinity profile in the central part of Laura Island at different times after the storm surge in wet conditions. 108

Figure 7-22: Pumping wells response to inundation scenarios in wet conditions: recharge function, freshwater lens volume and concentration at PW1, PW2, PW3, PW5, PW6 and PW7. The grey lines on the secondary y-axis represent abstraction and the red dashed line the 2500 $\mu\text{S}/\text{cm}$ limit..... 109

Figure 7-23: Pumping wells response to inundation scenarios in dry conditions: recharge function, freshwater lens volume and concentration at PW1, PW2, PW3, PW5, PW6 and PW7. The grey lines on the secondary y-axis represent abstraction and the red dashed line the 2500 $\mu\text{S}/\text{cm}$ limit..... 110

Figure 9-1: Completed rainfall series, temperature, PET and Calculated Recharge. 129

Figure 9-2: Calculated (blue line) and measured (red dots) normalized heads at three multi-level observation wells (1-43, 4-48 and 9-43) for the HYCOS (left) and MCAP (right) campaigns from the calibrated Daily Transient Model. 135

Figure 9-3: Calculated (blue line) and measured (red dots) normalized heads at three multi-level observation wells (9-33, 6-43 and 3-28) for the HYCOS (left) and MCAP (right) campaigns from the calibrated Daily Transient Model. 136

Figure 9-4: Calculated (blue line) and measured (red dots) normalized concentration at six multi-level observation wells (2-33, 3-18, 4-58, 5-18, 6-43 and 8-28) from the calibrated Daily Transient Model. 137

Figure 9-5: Calculated (blue line) and measured (red dots) normalized concentration at six multi-level observation wells (1-33, 1-43, 2-23, 2-43, 3-28, 3-38B) from the calibrated Daily Transient Model. 138

Figure 9-6: Calculated (blue line) and measured (red dots) normalized concentration at six multi-level observation wells (3-48, 4-18, 4-48, 4-68, 5-33, 5-48) from the calibrated Daily Transient Model..... 139

Figure 9-7: Calculated (blue line) and measured (red dots) normalized concentration at six multi-level observation wells (7-53, 7-63, 8-38, 9-43, 10-13, 10-43) from the calibrated Daily Transient Model. 140

Figure 9-8: Calculated (blue line) and measured (red dots) normalized concentration at the pumping wells from the calibrated Daily Transient..... 141

Figure 9-8: Calculated and measured normalized heads obtained from the calibration of the Daily Transient model. 142

Figure 9-8: Calculated and measured concentrations obtained from the calibration of the Daily Transient model..... 143

Figure 9-8: Calculated and measured concentrations obtained from the calibration of the Daily Transient model..... 144

Figure 9-8: Calculated and measured concentrations obtained from the calibration of the Daily Transient model..... 145

Executive summary

The Pacific Community (SPC) in collaboration with UNDP is implementing the Managing Coastal Aquifers (MCA) Project funded by the Global Environment Facility (GEF). The regional project takes place in the Republic of Marshall Islands (RMI), Republic of Palau, and Tuvalu and aims at improving the understanding, use, management and protection of coastal aquifers towards enhanced water security, in the context of a changing climate.

In the MCA project, A21 has collaborated in the development and calibration of a three-dimensional numerical model with variable-density flow and salinity transport in Laura, Majuro Atoll, with the participation of key stakeholders in RMI, including MWSC, RMI EPA, National Disaster Management Office, Laura Lens Committee, and SPC MCA project. The model is used as management tool to provide guidance on management and operation strategies for the freshwater lens and to quantify future impacts of external influences such as abstraction, storm surge inundation, and climatic stresses.

First, after reviewing and analysing all available information the conceptual model of Laura has been defined. The conceptual model includes the three-dimensional geometry of the different hydrogeological units, their parametrization, and the definition of the flow mass balance (inflows and outflows) of the system. Once the conceptual model is established, a three-dimensional numerical model has been developed with the software COMSOL Multiphysics. The model has been set-up to reproduce the historical response of the freshwater lens and head distribution to variations in the recharge, sea level and abstraction from January 2007 to November 2022.

The performance of the calibration process has been analyzed in terms of the fit to temporal series of head and concentration measurements and the plausibility of the estimated hydraulic conductivity fields. Satisfactory head fits are obtained from the calibration with the 90% of the residuals ranging between -0.1 and 0.1 m. On the other hand, the comparison between simulated concentrations and measurements indicates that, overall, the model accurately reproduces major features of the concentration distribution and its dynamics for all the wells. The absolute mean error (MAE) values for heads and normalized concentrations are relatively small, standing at 0.1 m and 0.024, respectively. These errors are considered adequate for a regional scale model. Moreover, the normalized root mean square error (normalized RMSE) for concentrations is lower than 5 %, indicating acceptable errors between computed and measured data.

Once the calibrated model adequately reproduces the historical behaviour of the system, future scenarios have been simulated for predicting impacts on the freshwater lens and time recovery

under transient conditions. The defined future scenarios focus on three key aspects: (i) the impact of extended drought periods, (ii) the effects of sea level rise, and (iii) the impact of rapid inundation due to storm surge events. For all scenarios, the reduction of the freshwater lens volume and the time required for its recovery has been evaluated.

- **Drought Events:**

Significant reductions in freshwater volume (up to 76%) are observed during droughts, with rapid recovery ranging from 6 to 15 months. During drought events most of the pumping wells show salinities above the drinking water limit and only a few water-supply wells can provide drinking water. However, numerical results show that salinity at the pumping wells is significantly controlled by the abstraction strategy and the effect is very local. Thus, once pumping rates decrease, the salinity at the wells return to acceptable salinity levels.

Higher pumping rates (30% of increase) during droughts exacerbate the increase in salinity near wells. The most vulnerable wells, i.e., those exceeding drinking water limits, are wells PW1, PW2, and PW7. However, when abstractions increase the change in the freshwater lens volume is negligible (less than a 3% reduction) because pumping only impacts locally the concentration distribution around the wells.

- *Management strategy:*

The proposed strategy is to extract a similar volume of water but distributing the rates evenly in time, i.e., avoiding peaks of high abstraction rates. It is recommended, however, not exceeding a threshold rate of 150 or 200 m³/day per well to maintain acceptable salinity levels. Moreover, spatial redistribution of pumping rates could improve the existing abstraction scheme. Thus, increasing abstractions during dry periods from wells least sensitive to salinization located in the inner part of the island (e.g., PW3) could minimise the impact of droughts.

In addition to that, abstraction from new wells located in the least vulnerable areas (innermost part of the inland) can be a source of water during droughts and inundation periods. Specifically, the area between wells PW 3 and PW5 is proposed as a favourable location. However, these new wells should be positioned far enough to the existing ones, to avoid the combination of upconing effects.

Artificial recharge of groundwater during non-drought periods is proposed as an alternative solution to accelerate the recovery of the lens volume after droughts and enhance groundwater storage and resilience during droughts. Thus, artificial recharge might increase available resources and also protect inland wells.

- **Sea-Level Rise (SLR):**

Sea level rise (without inundation events) has negligible impact on both the salinity at the pumping wells and the freshwater lens volume, with a reduction of less than 5% for 1 meter of sea level rise. However, SLR causes two effects that should be considered: (i) an inland migration of the interface with a movement of the freshwater lens of about 200 m at the middle of the island and (ii) an increase in the piezometric levels which might result in ponded groundwater in surface depressions.

- *Management strategy:*

Due to their vulnerability to ponding due to sea level rise, a sustainable land use in the lowest topographical areas should be defined avoiding new constructions and promoting its use as freshwater management areas. An alternative approach is to use these areas as freshwater reservoirs, employing green-blue nature-based structures. These structures can serve dual purposes, acting as temporary flooding parks during periods of high-water levels and functioning as recharge ponds during low-water seasons, facilitating groundwater replenishment.

- **Inundation Events:**

Inundation events caused by storm surges lead to saltwater infiltration that results in a 30% to 99% decrease in the volume of the freshwater lens, depending on the inundation extent. However, the freshwater lens shows resilience with a relatively rapid recovery within 2 or 3 years. Inundation events impact salinities at the pumping wells, with the wells PW1, PW2 and PW5 being the most vulnerable in exceeding the drinking water limits. However, a relatively rapid recovery is observed at the wells ranging from 7 to 12 months post-inundation.

- *Management strategy:*

The implementation of coastal protection measures might help to minimize inland inundation such as vegetated foreshore, seawalls and dikes. After an inundation event, abstractions to satisfy the demand of freshwater should shift to non-inundated areas, i.e., to the innermost wells (e.g. PW 3). However, pumping from wells in inundation areas might help to remove saltwater and restore drinking water quality near the coastline.

In addition to that, construction of new wells in the innermost part of the inland (between PW3 and PW5) might help for improved access to groundwater during draughts and inundation periods.

In general, the implementation of a robust early warning system together with continuous monitoring of groundwater levels and salinity is essential for early detection of saltwater intrusion following storm surges.

Limitations of the model

Numerical models of actual systems are usually based on a limited amount of data and, therefore, it is necessary to assume simplifications in the model design and parameterization. While the groundwater model developed for Laura Island provides valuable insights into the behaviour of the freshwater lens system, several limitations exist that must be discussed to understand what type of questions the model can provide accurately and reliably.

The main limitation of the model is the very limited temporal resolution of the abstraction data that made necessary to make assumptions to complete the data series. Salinities at the pumping wells are heavily dependent on the pumping rates. But those are only available for the years 2007 and 2016. Averaged and interpolated data were used to complete the abstraction functions. As a result, model predictions on salinities at the pumping wells might have a high degree of uncertainty, limiting the model to design optimized groundwater management strategies.

Other limitations include the relatively large scale of the model as well as the uncertainty related to the geometry and parametrization of the Hydrogeological Units. In particular, the geometry of the hydrogeological units largely control the shape of the freshwater lens. In this model a unique geometry was considered.

Key recommendations to improve model predictions include:

- Data Availability and Quality: The model's accuracy heavily relies on the availability and quality of input data, including groundwater flow dynamics and aquifer characteristics. Conduct comprehensive field surveys and monitoring programs to collect high-quality data on groundwater levels, salinities and pumping rates is essential for the optimization of abstraction schemes during droughts or inundation events.
- Hydrological Processes: The model might oversimplify hydrological processes, such as recharge mechanisms or the connection observed between the ocean-lagoon and the system. Considering the influence of land use and land cover on recharge estimations.
- Geometry of the hydrogeological units. The definition of the geological layers is based on a unique geological cross-section and based on it, the depth of the layers is extrapolated to the whole island extent. Moreover, the connectivity of the units with the sea in the inner part of the lagoon is not well characterized. The geometry largely controls the shape of the freshwater

lens. Therefore, further field investigations such as geophysics, construction and description of new boreholes and long-term pumping tests are required to characterize in detail (i) the unconfined behaviour of system and (ii) vertical variations of the hydraulic properties of the system. Studies to characterize the geometry and parametrization of the Hydrogeological Units would be required to increase the precision of the model and decrease prediction uncertainty

- Model Calibration and Validation: Numerical results indicate that the freshwater lens is mainly controlled by the recharge and the geometry and parametrization of the Hydrogeological Units, whereas heads variations are mainly controlled by sea level fluctuations. Moreover, salinities at the pumping wells are strongly controlled by the abstractions that are only available for the years 2007 and 2016. The uncertainties associated with parameter estimation and simplifications adopted with pumping rates may affect the model performance. Therefore, detailed records of abstractions, together with continuous monitoring of groundwater levels and salinity.

1 Introduction

1.1 Background

Small Island Developing States (SIDS) are particularly vulnerable to increased stresses on their water resources. The limitations of land, population, and water resources and the need for economic development and social well-being place particular pressures on them. Furthermore, a particular feature of SIDS, which sets them apart from their continental neighbours, is the close interconnection between land and sea and the role of water as the medium of connection between them.

The Pacific Community (SPC) in collaboration with UNDP is currently implementing the Managing Coastal Aquifers (MCA) Project funded by the Global Environment Facility (GEF), a regional project taking place in the Republic of Marshall Islands (RMI), Republic of Palau, and Tuvalu. The project aims at improving the understanding, use, management and protection of coastal aquifers towards enhanced water security, including in the context of a changing climate. More specifically it aims at (i) identifying the extent, threats and the development potential of groundwater resources, (ii) increasing awareness of groundwater as a water security supply source, (iii) providing options for improved access to groundwater, and (iv) improving aquifer protection and management, within Pacific Small Island Developing States.

The Managing Coastal Aquifers in Selected Pacific SIDS project (MCA Project) will directly and positively impact the communities in which it is being implemented as well as the broader network of customers that Majuro Water and Sewer Company (MWSC) supplies water and the key stakeholders in Republic of Marshall Islands (RMI). To be able to better map the groundwater sources that are available to Majuro Atoll and to forecast these resources for better management, the development of a groundwater model for Laura, Majuro Atoll, RMI is required. The process to develop the numerical model has involved the participation of key stakeholders in RMI, including MWSC, RMI EPA, National Disaster Management Office, Laura Lens Committee, and SPC MCA project.

1.2 Objectives

The objective of this project is to develop and calibrate a three-dimensional groundwater model for the Laura lens in consultation with the SPC MCA project team and key stakeholders in RMI. The numerical approach focuses on providing guidance on management and operation strategies for the freshwater lens in Laura that can be used by small water operators, communities and regulators and disaster management agencies to help maximize groundwater abstraction, especially during droughts and seawater inundation from storm

surge, and manage saltwater intrusion deteriorating the abstracted water quality. To this end, the calibrated model is used as a numerical tool to quantify future impacts of external influences such as abstraction, storm surge inundation, and climatic stresses.

The present study is organized in three activities:

- Activity 1: Review of existing information (Chapter 2) and development of the groundwater conceptual model (Chapter 3).
- Activity 2: Groundwater model construction (Chapter 4), calibration (Chapter 5) and sensitivity analysis (Chapters 6).
- Activity 3: Quantification of the impacts of future climatic, storm surge and sea level rise scenarios on the freshwater lens (Chapters 7 and 8).

2 Collection and analysis of information

2.1 Documents and data

The initial task involved thoroughly reviewing all the information provided by PC, including:

- Comprehensive documentation: This included detailed reports, studies, and assessments covering various aspects of Laura Island and some other relevant literature.
- Data sets: A repository containing data related to groundwater levels and salinity, inundation scenarios, meteorological data, tidal gauge data.
- GIS layers: Spatially referenced information represented as map layers, depicting crucial elements such as the location of observation and pumping wells, as well as the pumping well arms geometry, geophysical profile lines, and topobathymetry.

2.2 Meteorological data

The system is recharged by direct precipitation. Rainfall data is available from two meteorological stations at Majuro Atoll: Laura station and Majuro Airport station. Temperature data is available only at Majuro Airport station (Figure 2-1).

Table 2-1 summarizes the data availability and quality at each station. Majuro Airport station has the longest period of record, with a long-term dataset exceeding 64 years with no missing data. Laura station has limited rainfall data, but a high correlation is observed between the

rainfall measurements at both stations. Therefore, Majuro Airport station can be used for recharge estimation in Laura Island.

Table 2-1: Meteorological data available at Laura and Majuro Airport

Monitoring point		Rainfall	Temperature	Source
Laura	Frequency	Daily	No records	Received from PC
	Records	5299		
	Date range	01/08/1990 – 30/06/2019		
	Missing data	5261 (50%)		
	Units	Inches		
Majuro Airport	Frequency	Daily	Daily	Received from PC
	Records	22134	24113	
	Date range	09/02/1951 – 31/03/2023	11/02/1951 – 31/03/2023	
	Missing data	3184 (12%)	2233 (8%)	
	Unit	Inches	Fahrenheit	

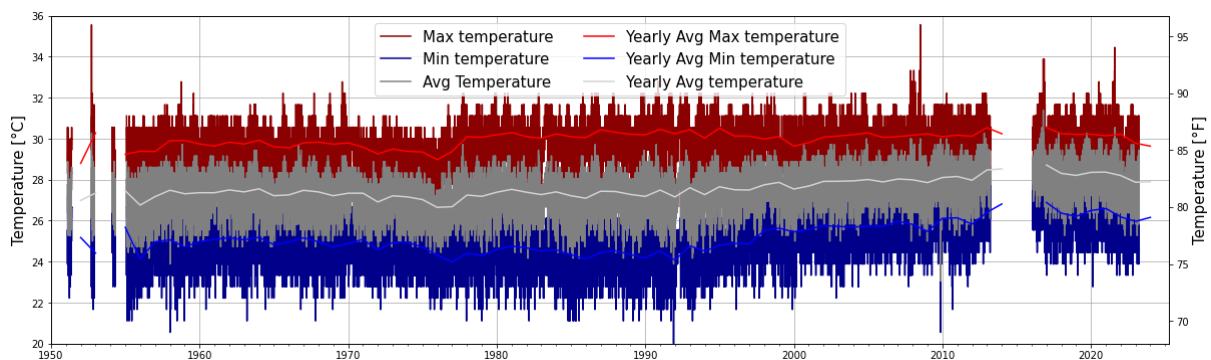


Figure 2-1: Temperature at Majuro Airport (1950 - 2023)

The average annual precipitation collected at Majuro Airport station for the period 1951 - 2023 is 3522 mm. The monthly average precipitation shows a seasonal pattern with relatively dry and wet seasons (Figure 2-2). October is the wettest month with a monthly mean precipitation of 363 mm, and February is the driest with a monthly mean precipitation of 180 mm. This seasonality is further evident in the rainfall trend throughout the year and impacts on the thickness of the freshwater lens.

The climate in Majuro is tropical, characterized by mild to warm temperatures. Temperature data shows minor fluctuations throughout the year, with the highest temperatures for the wettest months.

The annual rainfall deviation from the mean rainfall for all years is shown in Figure 2-3. There is a considerable variability throughout the time series, with 3 to 5 successive years below average rainfall. Although some years present considerably more rainfall than average (exceeding 1000 mm) and others show substantial deficits (below average rainfall by more than 1000 mm), no clear patterns of consistent increase or decrease over time are observed. The years 1970, 1983, and 1992 stand out as the driest years on record. From 1997 to 2013, most years appears to be below average rainfall compared to the later years, which tend to be above average.

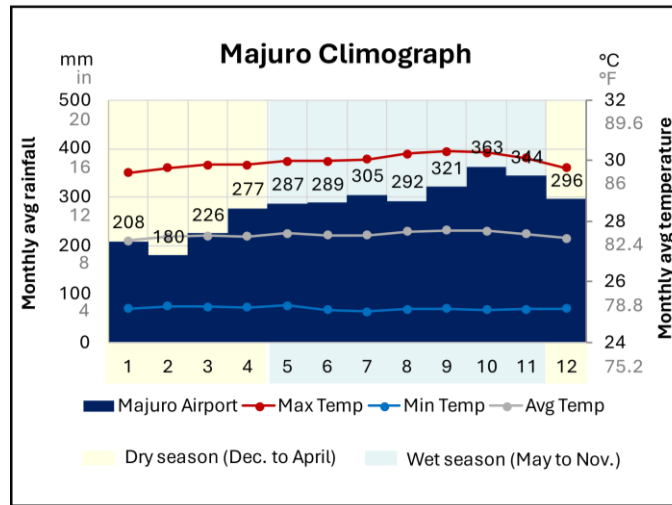


Figure 2-2: Climograph of Majuro. Average data over 64 years (1951-2023).

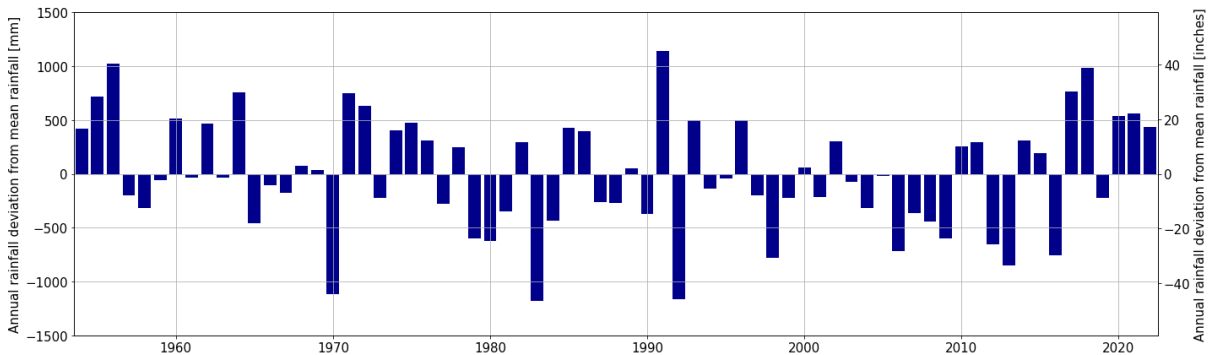


Figure 2-3: Annual rainfall deviation from the mean rainfall.

2.3 Sea-level

Sea-level is available from two monitoring locations at Uliga: Uliga tide gauge and PacIOOS. Tide gauge details are presented in Table 2-2.

At the Uliga monitoring location, data has been recorded hourly since January 1, 2007, with minimal gaps until August 7, 2022. The PacIOOS gauge records sea level every 4 minutes, providing a higher resolution dataset. However, PacIOOS dataset covers a shorter period, from February 28, 2022, to November 11, 2022, with 21% of the observations missing. It is important to mention that the time recorded by the tide gauge at Uliga is in Coordinated Universal Time (UTC). Consequently, to synchronize both datasets, 12 hours have been added to the recorded time series of Uliga. This adjustment ensures that the data reflects the appropriate local time frame.

Table 2-2: Tide gauge data available at Majuro

Monitoring point		Sea-level	Source
Tide gauge - Uliga, Majuro	Frequency Records Date range (UTC Time) Missing data Units	Hourly 135604 01/01/2007 00:00 - 08/07/2022 23:00 3908 (3%) Sea level in m	Received from PC
Tide gauges PacIOOS nss_007	Frequency Records Date range Missing data Units	Every 4 min 81604 28/02/2022 00:00 - 10/12/2022 23:56 21355 (21%) Water column above sensor in m	Downloaded from PacIOOS

2.4 Monitoring wells

Groundwater levels and salinity (measured as electrical conductivity) are monitored from 35 monitoring wells at 11 sites, that were constructed in May 1998, see Figure 2-4. Each site consists of 2 to 4 monitoring wells at different depths to determine the thickness of the freshwater lens. The shallowest well at each monitoring-well site penetrates the freshwater lens by only a few meters. The intermediate and deepest wells at each site were driven to better delineate the freshwater – saltwater mixing zone.

The available information (heads and electrical conductivity measurements) at the monitoring wells has been used for the calibration of the numerical model.

Monitoring has been conducted through three distinct campaigns:

- The short-term HYCOS campaign (January and February 2008) is characterized by highly regular data collection every 1 and 5 minutes over a single day.
- The long-term HYCOS campaign involves monitoring over longer time intervals from February 2008 to June 2009.

- The MCAP campaign extends from May to November 2022.

Additionally, manual measurements of different variables, including water depth and electrical conductivity, are also available.

Details about the HYCOS and MCAP campaigns as well as the manual measurements are included in the Appendix A.1.

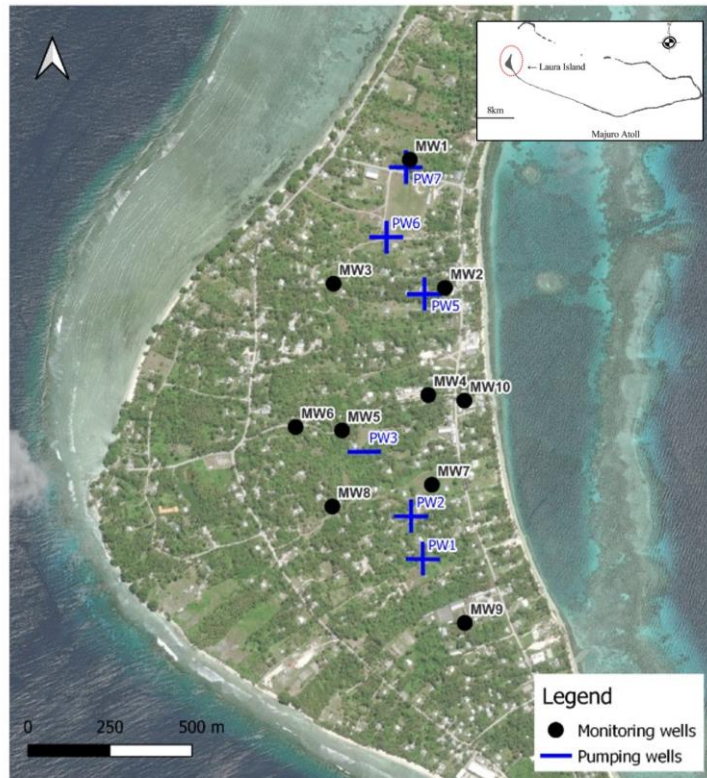


Figure 2-4: Map of monitoring wells and pumping wells.

A database has been created in separate Excel files for each campaign: HYCOS, MCAP, and for the manual dataset.

2.5 Abstractions

Water-supply wells were designed to collect water from the top of the freshwater lens by using shallow horizontal galleries installed approximately 2-3 feet below the water table. These galleries consist of 4-inch (0.1 m) perforated pipes that extend approximately 150 feet (46 m) in opposite directions from a central deeper concrete-lined sump. The deeper location of the sump allows water to flow into it by gravity from the horizontal pipes. Then, water is pumped from the sump by a surface mounted suction pump.

Pumping records are available for the years 1998, 2007, and 2016 (Table 2-3). For the year 1998, monthly data are available from January to December (Hamlin and Anthony, 1987 and Presley, 2005). For 2007, daily records are available from January to June, except for the wells PW5 and PW6, which were not in use during this period. For 2016, daily data is available from January to December, excluding March, where data is not available. Although there is a lack of continuous measurements, pumping records suggest a general reduction in pumping activity between 1998 and 2016. Note that the average total pumping was higher in 1998 compared to the ones for the years 2007 and 2016 due to the demand for drinking water during the 1998 Drought.

Table 2-3: Available pumping data

Bore name	Start time (month/year)	End time (month/year)	Records	Average (gal/d)	Average (m ³ /d)
PW1	Jan-1998	Dec-1998	12	46420	175.7
	Jan-2007	June-2007	181	37516	142.0
	Jan-2016	Dec-2016	211	11813	37.9
PW2	Jan-1998	Dec-1998	12	35983	136.2
	Jan-2007	June-2007	181	13423	50.8
	Jan-2016	Dec-2016	211	15728	51.9
PW3	Jan-1998	Dec-1998	12	35412	134.0
	Jan-2007	June-2007	181	15651	59.2
	Jan-2016	Dec-2016	211	7828	23.2
PW5	Jan-1998	Dec-1998	12	17305	65.5
	Jan-2007	June-2007	-	-	-
	Jan-2016	Dec-2016	211	7720	25
PW6	Jan-1998	Dec-1998	12	43346	164.0
	Jan-2007	June-2007	-	-	-
	Jan-2016	Dec-2016	211	8199	27.2
PW7	Jan-1998	Dec-1998	12	34718	131.4
	Jan-2007	June-2007	181	26823	101.5
	Jan-2016	Dec-2016	211	13340	42.0
TOTAL AVERAGE	Jan-1998	Dec-1998	-	213933	809.8
	Jan-2007	June-2007	-	93412	353.60
	Feb-2016	Sept-2016	-	64628	207.3

2.6 Resistivity profiles

Six East-West Electrical Resistivity Tomography (ERT) profiles performed across Laura Island are available to delineate the thickness of the freshwater lens (Figure 2-5). These profiles provide valuable information about the underground distribution of electrical resistivity.

Figure 2-5 presents the vertical profiles. Values of high resistivity at the top of the profile indicate the presence of freshwater, whereas low resistivity values at depth indicate the presence of seawater. The interface between freshwater and seawater seems to be located approximated 15 meters below the surface in the northern part of the island and around 20 meters at the mid-island area. In contrast, the southernmost profile shows complex patterns with significant heterogeneity, rendering its interpretation challenging.

The interpretation of the ERT profiles was used for the calibration of the shape and depth of the freshwater lens in the Steady State Model.

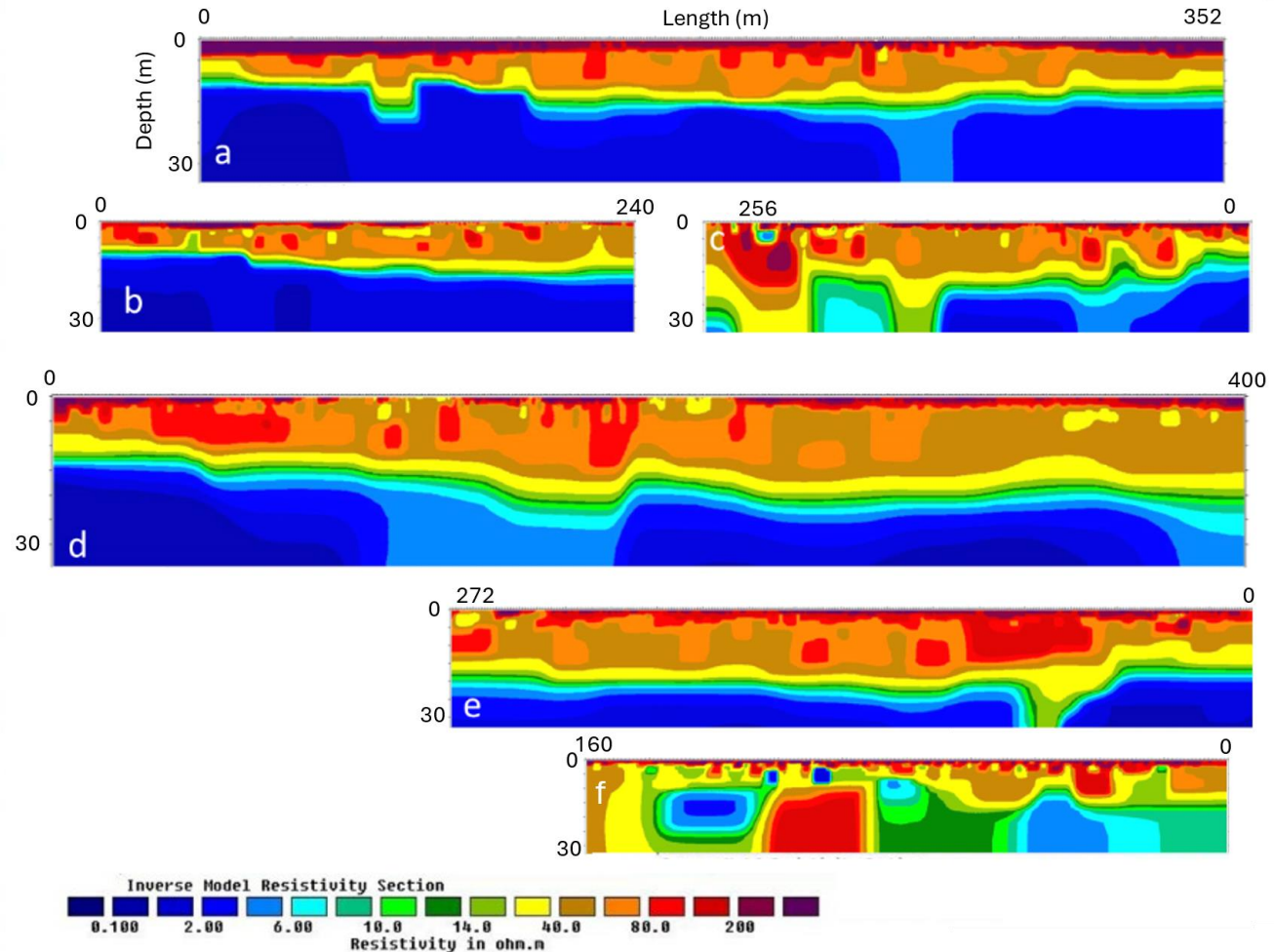


Figure 2-5: Electrical Resistivity Tomography profiles

2.7 Topobathymetric elevation

The one-meter topobathymetric elevation map of Majuro reveals a classic atoll morphology characterized by distinct elevation zones (Palaseanu-Lovejoy et al. (2017), see Figure 2-6. Atolls, as low-lying islands, are particularly susceptible to sea-level rise and inundations. At the core of the atoll lies a shallow seawater lagoon often referred to as “the heart of the atoll”, with depths ranging from a few meters to approximately 30 m. Surrounding the lagoon is the atoll rim, a low-lying reef-carbonate land area, which emerges only a few meters above the sea level.

The highest elevation of Majuro atoll is located at Laura Island reaching up to 3.45 meters above sea level. Along the ocean side, there is a short reef flat preceding a significant slope that extends outwards rapidly up to more than 1600 m (Figure 2-7). The reef flat plays a vital role in protecting coastlines against erosion and storms, acting as a natural barrier to dissipate wave energy before it reaches the coast. This information has been used to define the geometry of the numerical model, ensuring accuracy in representing the island's topography and bathymetry, as well as to impose the boundary conditions.



Figure 2-6: One-meter topobathymetric elevation map of Majuro.

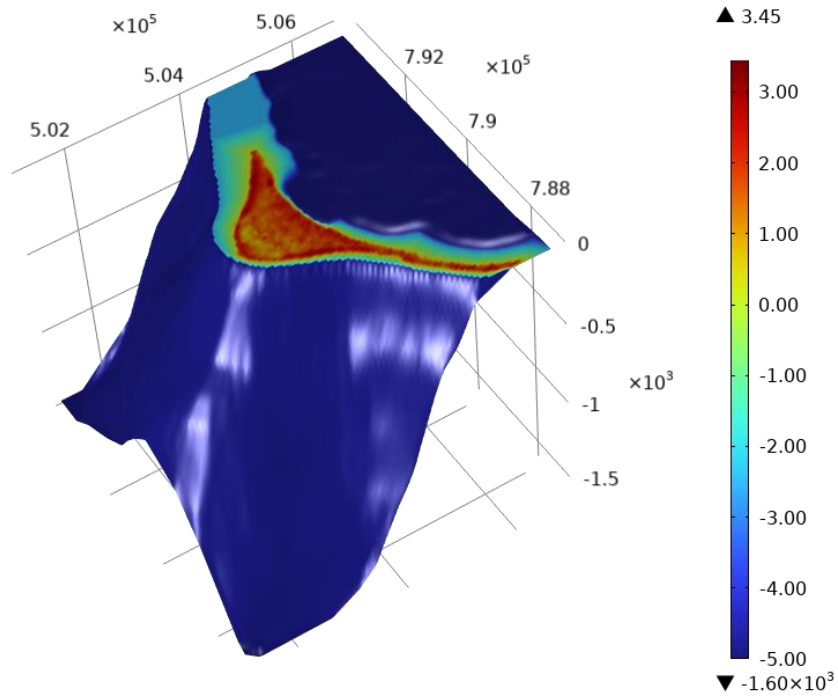


Figure 2-7: Topobathymetric elevation (m) around Laura Island.

2.8 Review of previous studies

From the information received, we highlight six previous studies conducted in Laura Island, Majuro (Marshall Islands). Table 2-4 summarizes the information that was extracted from each document to define the conceptual and numerical models.

Table 2-4: Previous studies extractible information

Reference	Hamlin and Anthony (1987)	Mink (1996)	Presley (2005)	Antoniou (2008)	SPC (2017)	Jansen (2021)	Koda (2017/2018)
Geological description	X						
Water budget	X	X	X	X	X	X	
Hydraulic parameters	X	X				X	X
FW-SW Interface depth	X	X	X	X	X		X
Tidal analysis	X			X	X		
Chemistry	X	X	X	X	X		
Geophysics	X			X			
Numerical model		X				X	X

3 Conceptual model

3.1 Study area

Laura Island is located on the western coast of Majuro Atoll in the Republic of the Marshall Islands (RMI). Situated in the central Pacific Ocean, approximately 2,500 miles southwest of Hawaii, the Marshall Islands are part of the Micronesia region and consists of numerous atolls and islands. The capital of the RMI is on Majuro Atoll. The population of Majuro was estimated in 2021 by the Pacific Community (SPC) at 23,156 (Republic of the Marshall Islands 2021, census report), representing over half the nation's total population.

Most of the population of Majuro resides on the Dalap-Uliga-Darrit (DUD) area located at the eastern end of the atoll. The DUD area is the commercial, residential and population centre of Majuro and the seat of the Marshall Islands government. Laura, with population of approximately 1,547 in 2021 (<https://www.citypopulation.de/en/marshall/>), is located at the western end of the atoll and is characterized by its rural and agricultural character. Landowners there engage in the cultivation of crops like coconut, banana, breadfruit, and/or taro (Presley, 2005; Figure 3-1).



Figure 3-1: Location of Laura, Majuro (RMI).

3.2 Geological features

The aquifer in the Laura area is composed by different lithologic units that have been identified from test drilling information. The main geological features of the area include distinct layers of calcareous sediments and limestone formations with a slope of 3 to 4 degrees from the ocean towards the lagoon side (Figure 3-2). The stratigraphy on the lagoon side was defined by Hamlin and Anthony (1987) and consists of Upper sediments beneath the soil layer composed of unconsolidated Holocene calcareous sands, with a thickness ranging from 6 to 12 meters (20 to 40 feet). Below this layer lies the Lower Sediments, characterized by a more cohesive mixture of lagoonal deposits from the Late Pleistocene/Early Holocene, consisting of calcareous silts, sands, and coarse-coraline materials, with a thickness ranging from 10 to 12 meters (33 to 40 feet). A significant reduction in material size is noted in the sediment units from the ocean side to the lagoon side, transitioning from coarse-grained materials to finer grained sands. Along the ocean side Upper Limestone outcrops emerge, formed of beach-rock and reef plate deposits. The underlying unit is a dense, highly permeable, and well-consolidated limestone (Lower Limestone), providing structural support for the entire units.

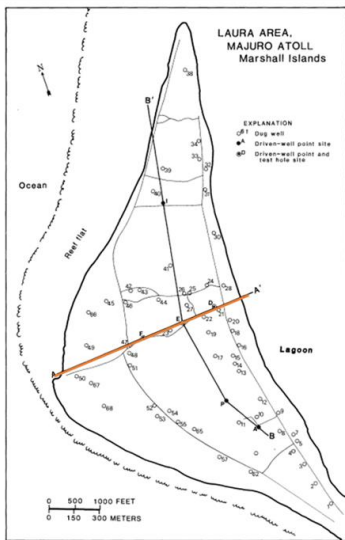


Figure 4. Locations of dug wells, well-point, and test hole sites.

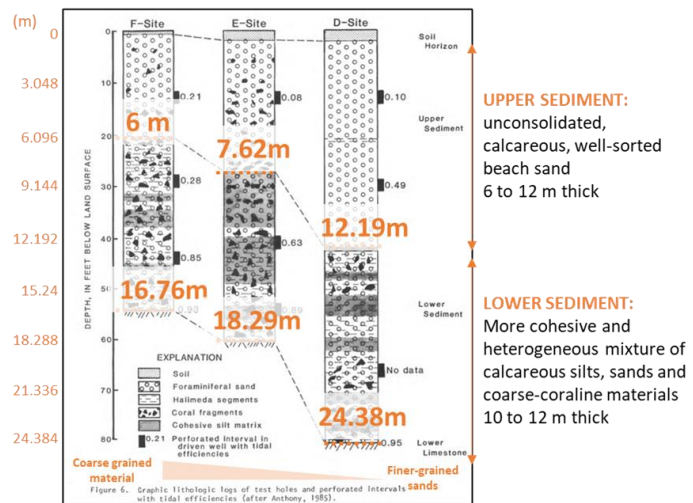


Figure 6. Graphic lithologic logs of test holes and perforated intervals with tidal efficiencies (after Anthony, 1985).

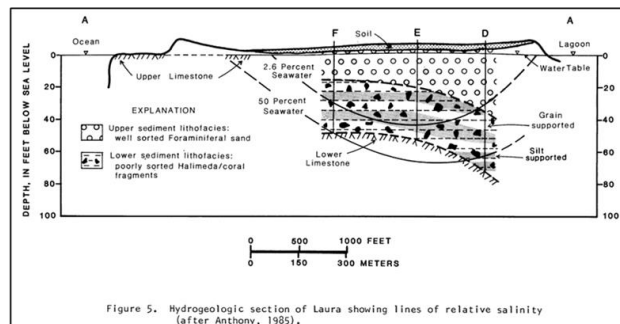


Figure 5. Hydrogeologic section of Laura showing lines of relative salinity (after Anthony, 1985).

Figure 3-2: Geological features of Laura Island (Hamlin and Anthony, 1987).

3.3 Sea-level temporal series

As presented in section 2.3, sea level data is available from two monitoring points. At the Uliga monitoring location, data has been recorded since January 1, 2007, with minimal gaps. However, this dataset extends from January 1, 2007, to August 7, 2022, covering the HYCOS campaign but not the MCAP campaign (May to November 2022). Records from the PaclOOS gauge, also located at Uliga, were used to fill this gap.

However, two short-term gaps for the hourly time series persisted for July and October 2022. However, these gaps had little impact on the construction of the numerical model for the period of main interest, as hourly data were only used for calibrating the short-term HYCOS campaign in 2007, and daily data were used for the calibration of the long-term campaigns (Long-term HYCOS and MCAP). Moreover, the remaining gaps constitute a minor fraction of the entire time series and are unlikely to significantly impact on the long-term trends simulated. Therefore, a simple approach was used to define a continuous daily time series for the sea level by filling the gaps through linear interpolation, see Figure 3-3.

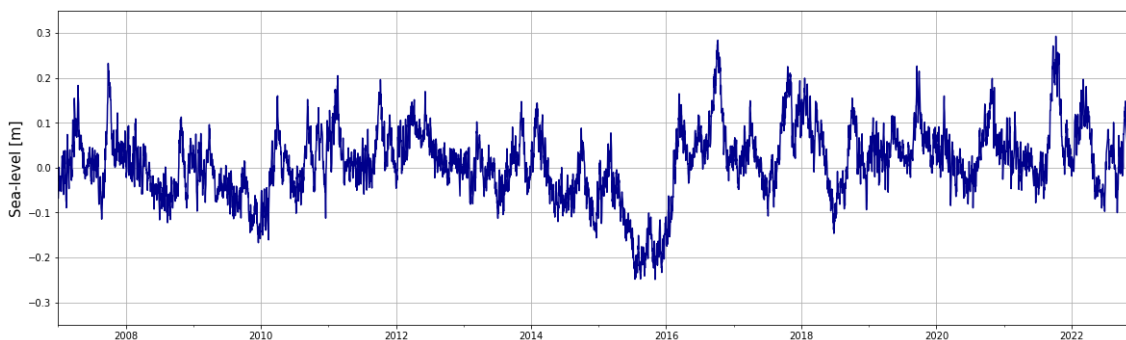


Figure 3-3: Completed daily temporal evolution of sea-level from 2007 to 2022.

Note that the sea level fluctuates daily with maximum amplitudes ranging from 20 to 30 cm. The highest sea levels usually occur from October to November, and the lowest from July to September.

3.4 Recharge estimation

Recharge (R) of the freshwater lens was estimated using the water balance model EasyBal for 68 years from 1954 to 2022. This program performs a daily soil water balance based on precipitation and evapotranspiration data and specific soil properties, see Table 3-1 and Appendix A.2. Since direct measurements of the evapotranspiration (ET) are not available at the meteorological stations, potential evapotranspiration (PET) was estimated by the Hargreaves-Samani (HS) method. This method uses different time series inputs such as

maximum (T_{Max}), minimum (T_{Min}) and average (T_{avg}) daily temperatures, as well as the mean extra-terrestrial radiation (R_a), which is latitude dependent, given the expression:

$$PET = 0.0023 \times R_a \times (T_{Max} - T_{Min})^{0.5} (T_{avg} + 17.8) \tag{Eq 3-1}$$

The method used by the EasyBal program for evaluating the soil water balance consists of calculating the effective rainfall and the actual evapotranspiration (AET) by solving the water balance equation. For the 2013-2015 period, yearly temperature averages calculated from the entire 64-year dataset were used in the PET calculations.

Table 3-1: Soil parameters used to perform the daily water balance in the soil.

Soil characteristics	Value	Reference
Field capacity (Volumetric contents)	0.12	Loamy Sand (Saxton and Rawls, 2006)
Initial soil moisture (Volumetric contents)	0.12	Starting from the field capacity
Root zone (m)	2.5	Jansen 2021 Comte et al. (2014)
Wilting point (Volumetric contents)	0.05	Loamy Sand (Saxton and Rawls, 2006)
Soil water capacity (mm)	175	Calculated
Initial water capacity (mm)	175	Calculated

Table 3-2 provides a comparative overview of water balance components, including precipitation, evapotranspiration, and recharge, across different studies and timeframes.

Figure 3-4 illustrates the annual recharge obtained for the period 1954 – 2022. The average precipitation was 3712 mm/yr ranging from 2550 mm/yr to 4896 mm/yr. The obtained annual recharge fluctuates between 50% and 76% of rainfall, with an average of 67% (approximately 1321 mm/yr, 3705 mm/yr and 2513 mm/yr, respectively). These results are in agreement with previous studies that estimated the evapotranspiration between 21% and 50% of rainfall, and recharge between 50% and 79% of rainfall. In this study as well as in previous ones, runoff was considered as negligible.

Table 3-2: Components of the water balance and their corresponding values derived from various studies found in the literature. Data presented in mm/yr for the considered period.

Reference	P	ET	R	Considered period	ET (%P)	R (%P)
Hunt and Peterson (1980)	-	-	-	-	50	50
Hamlin and Anthony (1987)	3560	1780	1780	Oct 1984 – Sept 1985	50	50
Mink (1996)	3403	1117	2286	n.s.	32	67
Antoniou (2008)	513	106	407	20 Nov 07 – 20 Dec 07 (1 month)	21	79
SPC (2017)	3254	1311	1943	Mean annual rainfall (1986-2015)	40	60
Jansen (2021)	3175	1423	1752	n.s.	45	55
This study	3712	1212	2500	1954 - 2022	33	67

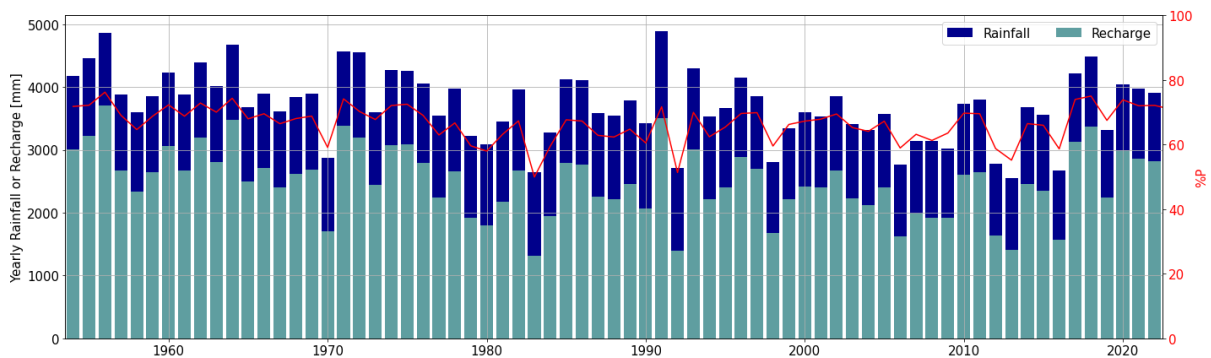


Figure 3-4: Yearly calculated recharge.

3.5 Abstractions

Two abstractions daily datasets are available within the period between 2007 and 2023, one between January and June 2007 and the other for the year 2016.

Table 3-3 shows the maximum, minimum and average pumping for each well from the available records. Monthly pumping data for 1998 are also included for comparison (Hamlin and Anthony, 1987 and Presley, 2005). The temporal evolution of the abstractions for each well is illustrated in Figure 3-5 for the dataset of 2007 and 2016.

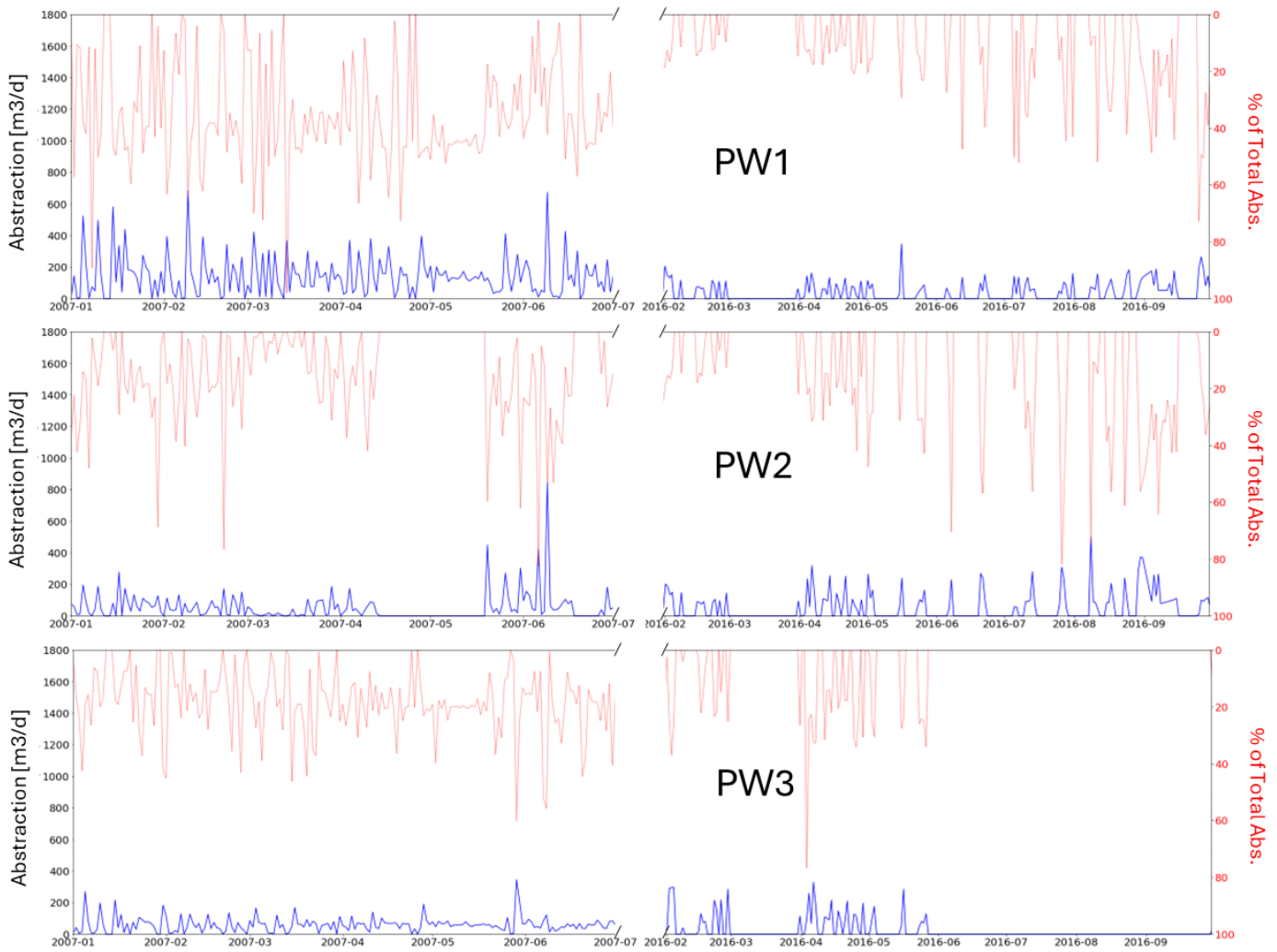
Table 3-3: Pumping (m³/d) for water-supply wells in the Laura area.

Well	1998 ^a	Pumping (m ³ /d) 2007			Pumping (m ³ /d) 2016		
	Average	Average	Maximum	Minimum	Average	Maximum	
PW1	175.5	142.0	682.5	1.9	37.9	346.7	14.4
PW2	136.0	50.8	845.7	0.4	51.9	497.0	8.3
PW3	133.9	59.2	344.9	0.4	23.2	328.2	8.7
PW5	65.4	0.0	0.0	0.0	25.0	484.7	3.7
PW6	163.8	0.0	0.0	0.0	27.2	635.9	1.1
PW7	131.2	101.5	434.9	1.9	42.0	444.0	34.1
Total	808.7	353.6	1600.1	17.8	207.3	1474.5	97.3

^a reported by Presley (2005) and Hamlin and Anthony (1987).

In 2007, only four wells (PW1, PW2, PW3 and PW7) were pumping, with a total monthly abstraction ranging from 1600.1 m³/d to 17.8 m³/d with an average of 353.6 m³/d. In 2016, although the six wells were pumping (PW1, PW2, PW3, PW5, PW6, and PW7, **Error! Reference source not found.**Figure 3-5) the total average pumping decreased to a value of 207.3 m³/d. Pumping was highest in water supply wells 2 and 7, and lowest in well 3.

Abstractions generally increase during droughts and dry seasons (December to April) to accommodate increasing demands. However, although pumping causes an upward movement of the interface leading to a decrease in the thickness of the freshwater lens, this impact is local because the total pumping is small compared to total recharge rates.



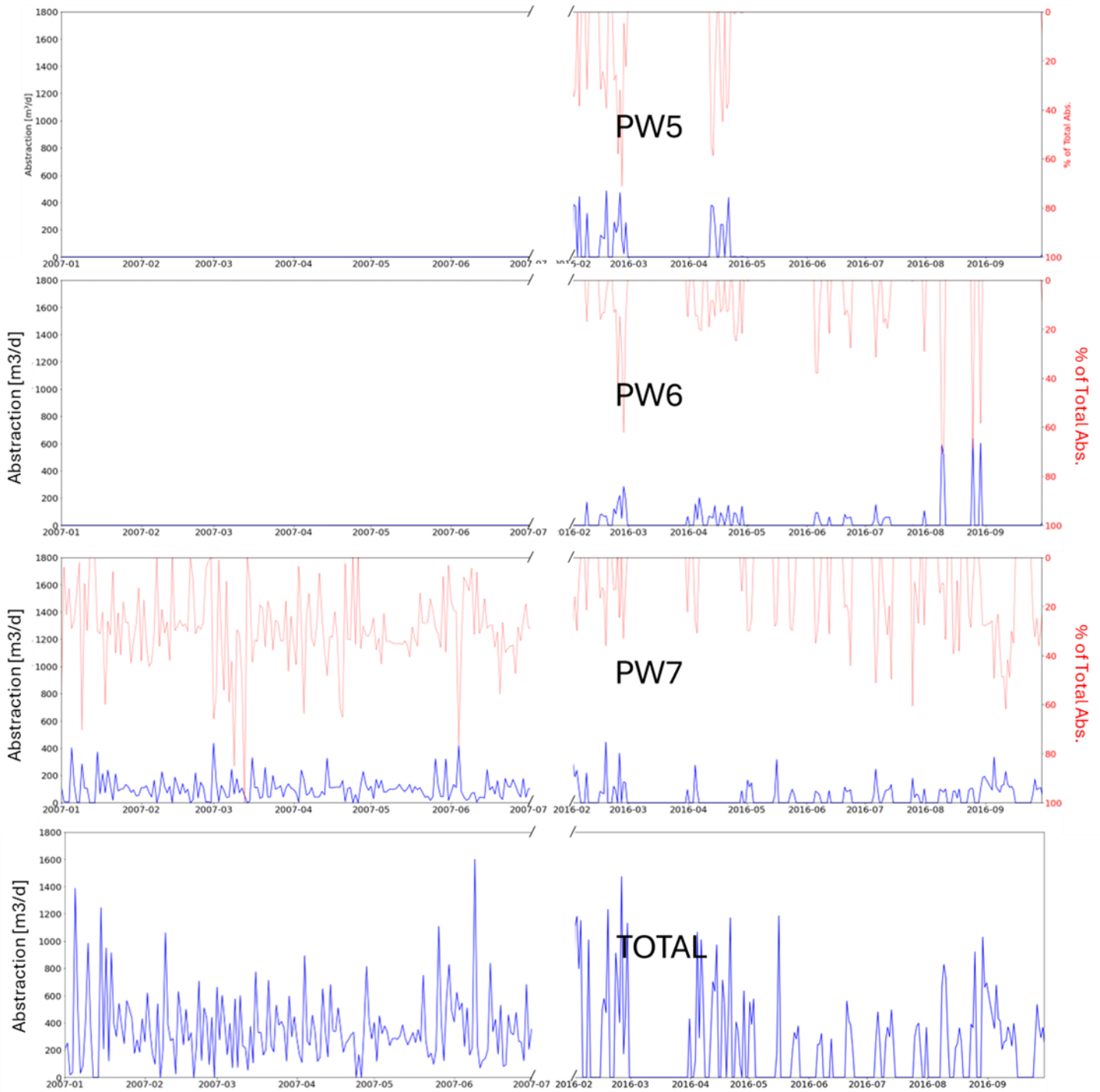


Figure 3-5: 2007 temporal evolution of abstractions.

Table -: Pumping (m³/d) for water-supply wells in the Laura area.

Well	1998 ^a	Pumping (m ³ /d) 2007			Pumping (m ³ /d) 2016		
	Average	Average	Maximum	Minimum	Average	Maximum	Minimum
PW1	175.5	142.0	682.5	1.9	37.9	346.7	14.4
PW2	136.0	50.8	845.7	0.4	51.9	497.0	8.3
PW3	133.9	59.2	344.9	0.4	23.2	328.2	8.7
PW5	65.4	0.0	0.0	0.0	25.0	484.7	3.7
PW6	163.8	0.0	0.0	0.0	27.2	635.9	1.1
PW7	131.2	101.5	434.9	1.9	42.0	444.0	34.1
Total	808.7	353.6	1600.1	17.8	207.3	1474.5	97.3

** reported by Presley (2005) and Hamlin and Anthony (1987).*

3.6 Tidal analysis and filtering

Water table records at the monitoring wells show a strong response to tidal fluctuations. Thus, the tidal signal observed at the wells is attenuated in time and magnitude with distance from the coastline. The tidal method is a technique for the characterization of coastal aquifers based on the analysis of groundwater responses to tidal fluctuations. In this project, the tidal method has been applied to estimate the hydraulic diffusivity of the aquifer.

3.6.1 Data filtering:

A series of Python scripts were developed for the filtering of the temporal series. These scripts include the filter proposed by Channel and Godín, (1972) and the methodology presented by Goyetche et al. (2023). The code employs a combination of low and high pass filters to remove diurnal, semidiurnal, and shorter-period components from a signal. Thus, the temporal series are split into tidal signal, noise, and general trend. It is important to mention that the transformation depends on two parameters: (I) the signal sampling frequency and (II) the total signal length. Figure 3-6 illustrates an example of the Python code application and provides a visual representation of the decomposition of the signal.

After filtering, the tidal signal is divided into harmonic constituents using a spectral analysis. Figure 3-7 displays the tidal harmonic spectrum for both the sea and monitoring well 3-38B. Note that the spectrum presents different tidal components in both the sea level fluctuations

and the wells, highlighting their frequencies and amplitude. As expected, the amplitudes are significantly reduced in the well compared to those observed in the sea.

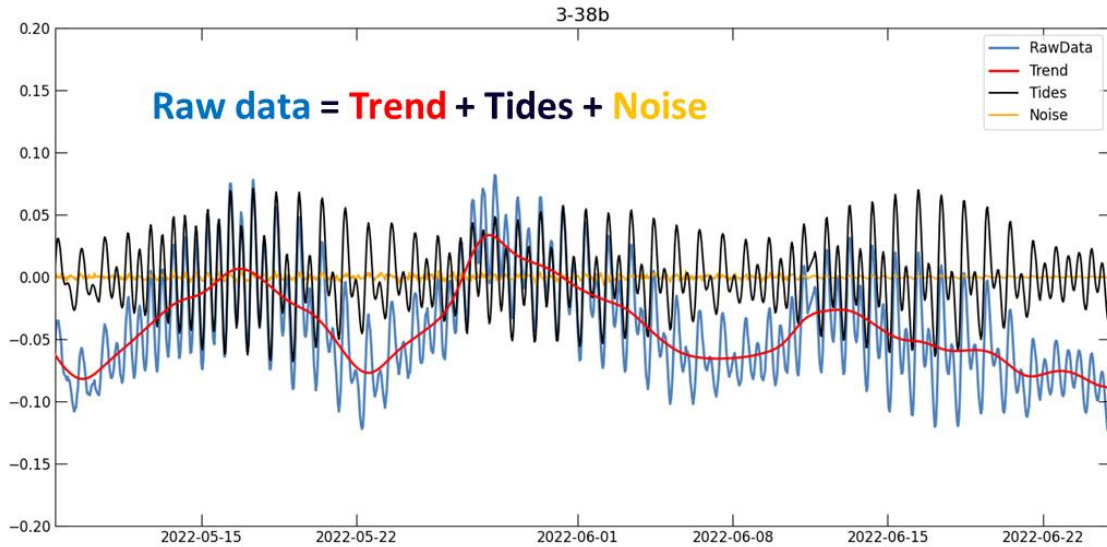


Figure 3-6: Resulting time series from Python code application at monitoring well 3-38B.

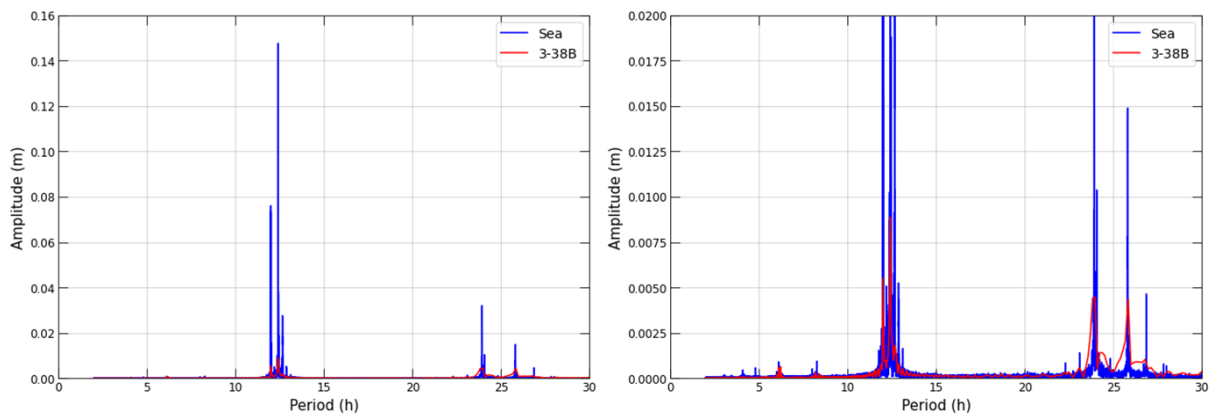


Figure 3-7: Tidal harmonics identified in the sea and monitoring well 3-38B.

3.6.2 Time shift determination

At observation wells, the amplitude of the tide-induced groundwater head fluctuations decays exponentially with distance from the coastline whereas the phase lag increases. This time shift or lag was determined using a cross-correlation analysis between sea level and monitoring well signals. A Python script was written to obtain the lag from the highest correlation, see Figure 3-8. In this process, only observations with a data resolution of at least 10 minutes were considered to ensure greater accuracy in the analysis.

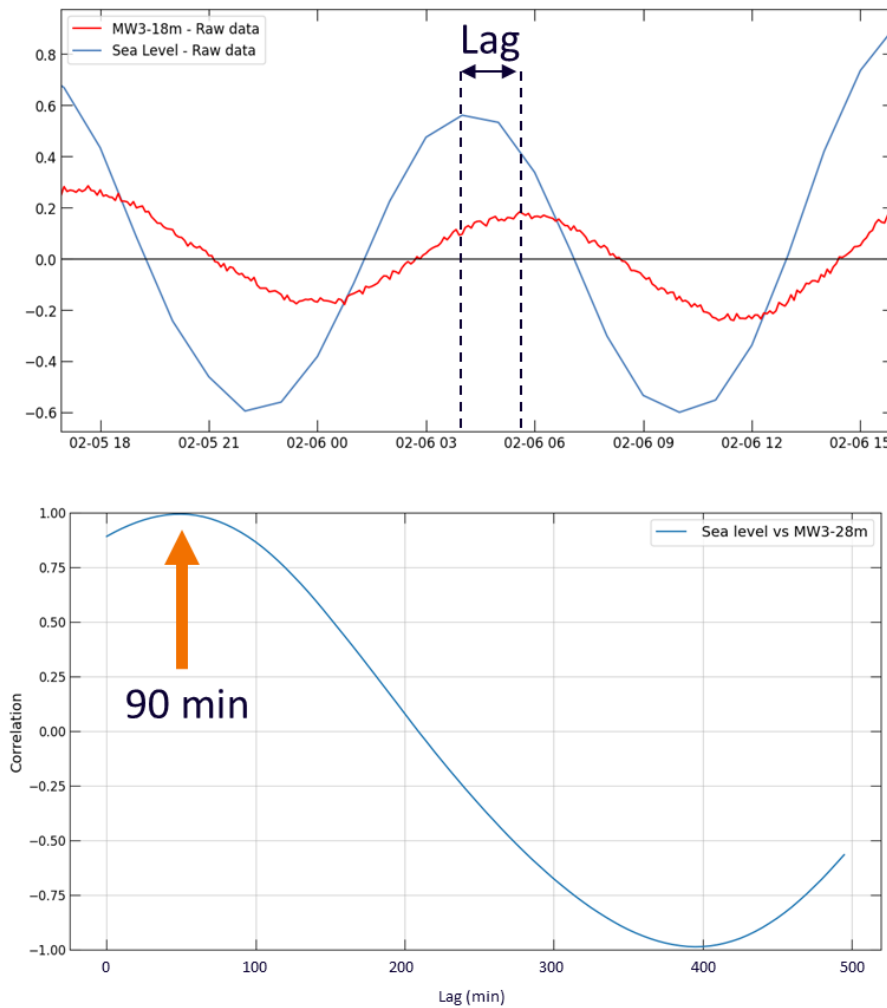


Figure 3-8: Measured level at Sea and MW3-18 and identified highest correlation for lag determination.

3.6.3 Tidal efficiency (TE) or damping

To calculate the amplitude attenuation, known as tidal efficiency or damping of the tidal signal between the sea and the monitoring well, the following steps were followed: Firstly, the temporal series of the monitoring wells were delayed by the computed lag so that their maximum and minimum values match with the ones for the sea level (Figure 3-9a). Next, both local maximums and minimums were evaluated obtaining the tidal efficiency (TE) with the expression $TE = A/A_0$, where A represents the amplitude of the signal at the monitoring well, and A_0 represents the amplitude of the signal of the sea. Since the tidal efficiency varies with tidal harmonics, to compute the hydraulic diffusivity the most frequent tidal efficiency was selected (Figure 3-9b).

Table 3-4 illustrates the lag and tidal efficiency obtained for each monitoring well.

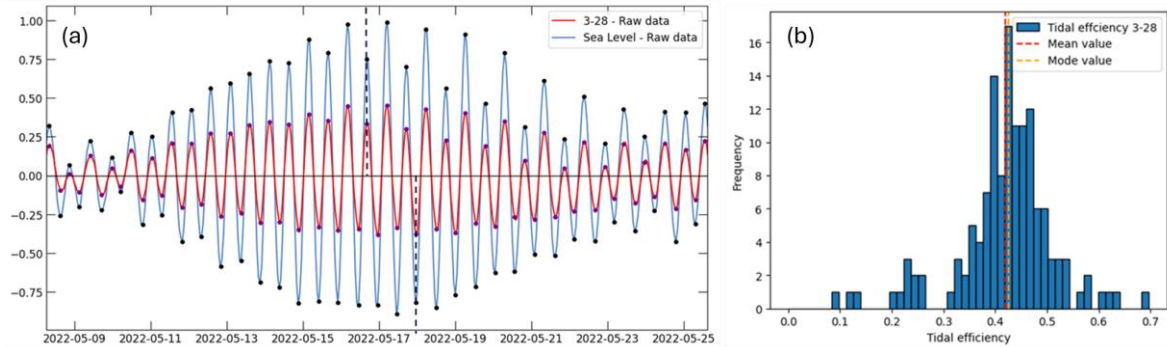


Figure 3-9: Example of tidal efficiency analysis, (a) Synchronized Sea level and MW3-28 series. (b) Distribution of tidal efficiency frequencies.

3.6.4 Hydraulic diffusivity

To estimate the hydraulic diffusivity for each monitoring well the Jacob (1950) and Ferris (1952) analytical solution was used. The solution considers a 1d infinite homogeneous system with uniform thickness. The fluid mass balance equation is given by:

$$\frac{\partial h(x, t)}{\partial t} = \frac{T}{S} \frac{\partial^2 h(x, t)}{\partial x^2} \tag{Eq 3-2}$$

with T the transmissivity and the S storage coefficient. This equation is subject to the following boundary condition at the contact with the sea $h_s(t) = h(x = 0, t) = \sum_i A_0 \cos\left(\frac{2\pi}{\tau} t\right)$, and $h(x = \infty, t) = 0$, with τ the tidal period. The solution of Eq 3-2 gives the head response inland as:

$$h(x, t) = A_0 e^{-x \sqrt{\frac{\pi}{D_h \tau}}} \sin\left(\frac{2\pi}{\tau} t - x \sqrt{\frac{\pi}{\tau D_h}}\right) \tag{Eq 3-3}$$

with D_h the hydraulic diffusivity defined as $D_h = T/S = k/S_s$. From the above equation two different expressions for the hydraulic diffusivity are obtained from the time-shift ($D_{h_{t_s}}$) and the tidal efficiency (D_{h_A}) reading as:

$$D_{h_{t_s}} = \frac{x^2 \tau}{4\pi t_s^2}, D_{h_A} = -\frac{x^2 \pi}{\tau (\ln(TE))^2} \tag{Eq 3-4}$$

where x represents the distance from the coast and $TE = A/A_0$, with A the amplitude of the signal at the monitoring well, and A_0 the tidal amplitude. The distance from the nearest coastline was determined for each monitoring well using GIS analysis (Figure 3-10).

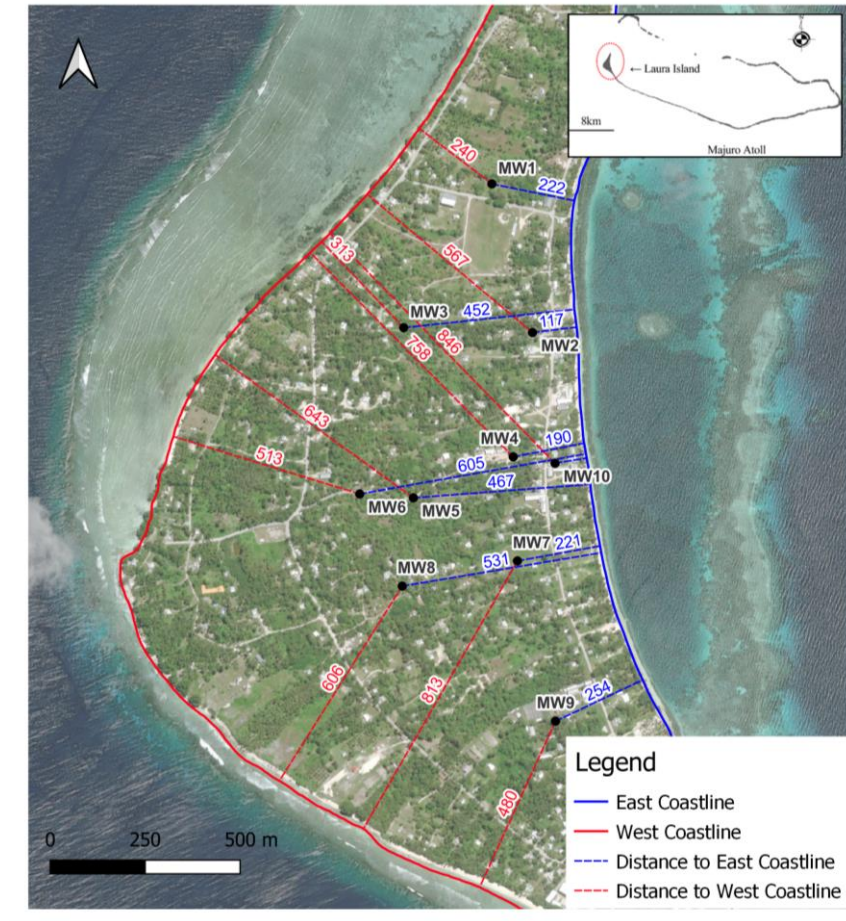


Figure 3-10: Distance from the coast.

Table 3-4 illustrates the estimates for the hydraulic diffusivity obtained at the monitoring wells. The asterisks (*) denote wells with limited tidal fluctuations, where the reliability of the results may be compromised. Numerous wells from the MCAP exhibit an absence of tidal fluctuations in their records, suggesting potential issues with either the sensor or the well itself, especially considering that previous campaigns had functioning records.

Table 3-4: Hydraulic diffusivity derivation from tidal analysis at monitoring wells.

Site	Bore name	Monitoring campaign	Shortest distance to the coast (m)	Time-shift (min)	TE (-)	D_{hA} (m ² /d)	D_{hTs} (m ² /d)
1	33	HYCOS Short MCAP	222	80	0.315	9287	655329
				-	-	-	-
	43	HYCOS Short HYCOS Long	117	55	0.391	14107	1386481
				60	0.397	14536	1165029
2	23	HYCOS Short	117	45	0.374	3583	577175
	33	HYCOS Short		25	0.501	7238	1870049
	43	HYCOS Short		20	0.603	13552	2921951
3	18	HYCOS Short	313	90	0.315	18501	1031440
	28	HYCOS Short MCAP		50	0.475	44688	3341865
				50	0.454	39712	3341865
	38B	HYCOS Short MCAP		155	0.253	13085	347749
				220	0.098	4575	172617
48	HYCOS Short	10	0.878	1460652	83546621		
4	18	HYCOS Short	190	140	0.077	1392	157056
	48	HYCOS Short HYCOS Long MCAP		15	0.684	63257	13681354
				10	0.715	80770	30783045
				-	-	-	-
	58	HYCOS Short		20	0.717	82152	7695761
68*	HYCOS Short	105	0.143	-	-		
5	18	HYCOS Short	467	90	0.290	36080	2300128
	28	HYCOS Short		70	0.380	59040	3802252
	33	HYCOS Short		25	0.665	332452	29809656
	48	HYCOS Short		25	0.752	680968	29809656
6	33	MCAP	513	-	-	-	-
	43	MCAP		60	0.581	225519	6242029
7	18*	HYCOS Short	221	235	0.074	-	-
	53	HYCOS Short		30	0.629	57456	4630650
	63	HYCOS Short		5	0.519	28687	166703402
8	28	HYCOS Short	531	50	0.229	32763	9635017
	38	HYCOS Short		45	0.326	56817	11895083
	48	HYCOS Short		30	0.573	230537	26763937
	58	HYCOS Short		130	0.416	92874	1425298
9	33	HYCOS Short MCAP	254	35	0.313	12058	4491170
				-	-	-	-
	43	HYCOS Short			0.587	57480	13754208

Site	Bore name	Monitoring campaign	Shortest distance to the coast (m)	Time-shift (min)	TE (-)	D_{hA} (m ² /d)	D_{hLS} (m ² /d)
		HYCOS Long		20		38348	13754208
	53	HYCOS Short		80	0.177	5424	859638
10	13*	HYCOS Short MCAP	84	180	0.196	-	-
				-	-	-	-
	43*	HYCOS Short MCAP		20	0.567	5610	1521534
				1670	0.236	866	218
	53*	HYCOS Short		155	0.364	-	-

Figure 3-11 shows the hydraulic conductivity calculated assuming a specific storage of 10^{-5} . Results suggest an increase in the hydraulic conductivity with the distance from the sea. Moreover, larger hydraulic conductivities are obtained for the monitoring wells located on the ocean side compared to the ones located on the lagoon side. Thus, monitoring wells on the lagoon side exhibiting values ranging from 0.05 to 1 m/d (multi-level wells 10 and 2), whereas those on the ocean side display values between 20 to 100 m/d (multi-level wells 3, 5, 6 and 8). This segmentation suggests that hydraulic conductivity is significantly higher near the ocean compared to the area near the lagoon. These results are consistent with the lithological description, where finer materials were found closer to the lagoon.

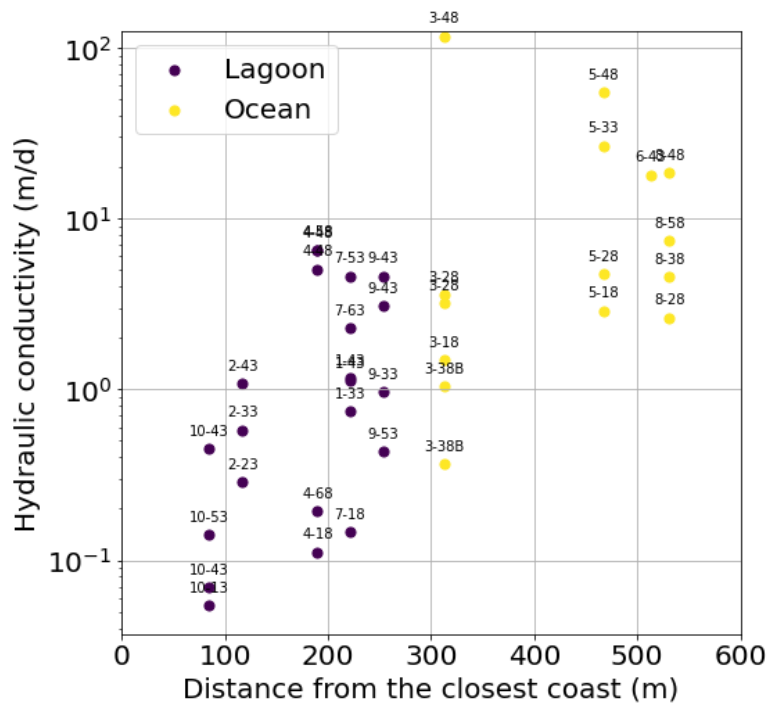


Figure 3-11: Hydraulic conductivity calculated from D_h with a specific storage of $1e-5$.

3.7 Hydraulic and transport parameters

Values for the hydraulic parameters found in the literature for the different hydrogeological units, including hydraulic conductivity, porosity, unit thickness, storage coefficient, and longitudinal and transversal dispersivities are illustrated in Appendix A.3.

Previous studies show a large contrast in permeability between the Upper and Lower sediments and the underlying Limestone (see e.g. Koda et al. 2017, 2018). Thus, the permeability increases with depth and this increase impact on the shape of the freshwater lens. Most of these studies assume a vertical anisotropy, ratio of vertical to horizontal hydraulic conductivity, to be approximately 1:10. Moreover, consistently with our results from the tidal method, Jansen (2021) obtained higher calibrated permeabilities on the ocean side compared to the ones on the lagoon side.

Limited information is available for the storage, that shows the unconfined nature of the system with values of approximately 0.17 and $1e-5$ for the specific yield and specific storage, respectively. Porosity also increases with depth from 0.2 for the Upper Sediments to 0.3 to the Lower Limestones.

3.8 Freshwater lens and piezometry

The thickness and shape of the freshwater lens at Laura were determined from a combination of data sources, including the average electrical conductivity readings obtained from both automatic sensors at HYCOS campaign and manual measurements and the depth inferred from the geophysical profiles. The freshwater limit on the ocean side defined by Antoniou (2008) was also considered. Then, an interpolation was performed to generate a three-dimensional representation of the freshwater lens. The freshwater lens was defined as the volume with electrical conductivity less than $2500 \mu\text{S}/\text{cm}$, a more conservative value than the one defined by White et al., (1999). Figure 3-12 illustrated the depth of the interface obtained.

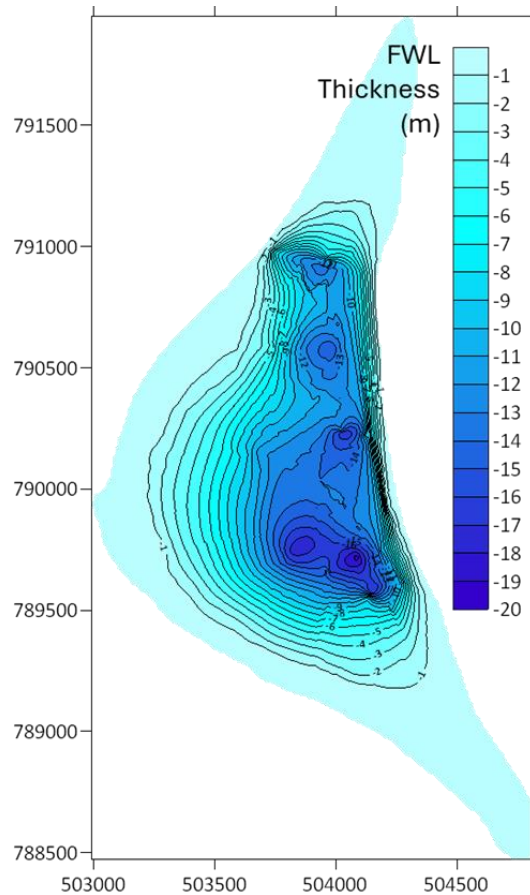


Figure 3-12: Plan view of the freshwater lens thickness.

Note that the depth of the freshwater lens ranges from 19 to 10 meters. Both, the north and the south ends of the freshwater lens are narrow, with the maximum thickness at the middle part of the island. Moreover, the thickness of the lens increases from the ocean side to the lagoon side, leading to an asymmetrical shape of the lens. This asymmetry is due to the geometry of the contact between the Upper and Lower Sediments with the underlying, highly permeable, Lower Limestones which is deeper at the lagoon side.

On the basis of available water-level data, creating an accurate piezometry map present several challenges due to the asynchronous nature of measurements from automatic sensors and the significant fluctuations in groundwater levels caused by tidal influences. The most reliable reference for the piezometric map is provided by Hamlin and Anthony (1987) with the water table distribution for April 1973. The piezometric contours range from 0.2 to 2.6 feet above sea level near the centre-East of the island, with the highest heads at the middle part of the island. Thus, groundwater flows from the centre of the island towards the ocean and the lagoon.

3.9 Water balance

The conceptualization of the system is shown in Figure 3-13. The freshwater lens underlies the 2.46 km² of Laura Island, following the island shape, with maximum thickness at the centre of the island. The low topographic gradient allows most precipitation to infiltrate, obtaining an annual recharge that fluctuates between 50% and 76% of rainfall.

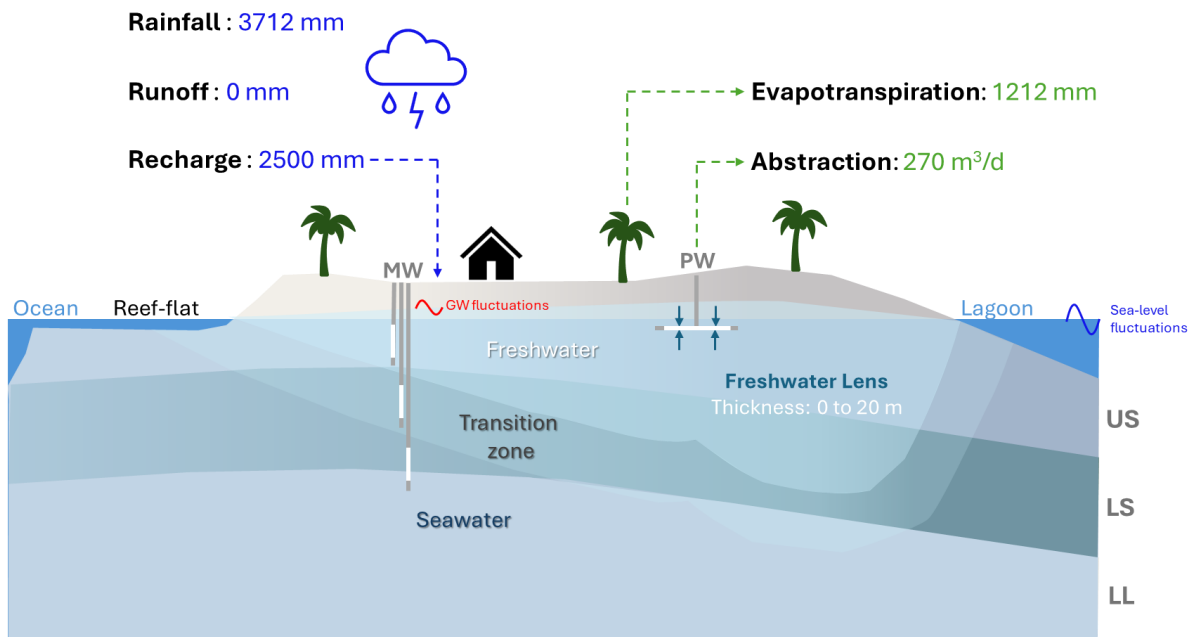


Figure 3-13: Hydrogeological conceptual model of Laura Island freshwater lens.

Reported values for the freshwater lens volume ranges from 1.70 to 2.68 hm³ considering freshwater as water containing less than 1.5% seawater (Table 3-5). The freshwater lens floats on denser seawater within the Upper Sediments. The salinity increases gradually downwards and laterally from the lens leading to a sharper mixing zone on the lagoon side.

Table 3-5: Freshwater lens volume.

Reference	Freshwater lens volume (hm ³)
Anthony et al. (1989)	1.70 2.10
Antoniou (2008)	2.68
SPC (2017)	2.00
Jansen (2020)	2.06

The aquifer is recharged by direct precipitation (ranging from 50% to 76% of the total rainfall) after accounting for evapotranspiration. The recharge varies seasonally, being highest during wet seasons. Discharge takes place primarily as submarine freshwater discharge and seepage along the lagoon and ocean boundaries driven by gravity and head gradients, particularly influenced by sea-level fluctuations. Additionally, abstractions contribute to outflows from the system. Closing the water balance, recharge accounts for 6.15 hm³/yr, and abstractions amount to 0.1 hm³/yr (representing 1.6% of recharge), resulting in a submarine groundwater discharge of 6.05 hm³/yr.

The thickness of the freshwater lens fluctuates is significantly affected by variations in recharge, sea-level fluctuations, and pumping activities. During periods of extended precipitation, the freshwater lens might thicken and expand laterally, whereas droughts conditions and increased pumping cause lens thickness to decrease. The response time of water table to sea level fluctuations (oscillations of metric order) is relatively rapid, but clear responses to recharge episodes are not evident from head records.

4 Numerical model

The purpose of the Activity 2 is to develop a three-dimensional numerical model with variable-density flow and solute transport for the Laura area to reproduce the historical variations in the freshwater lens and quantify the impact of future climatic and abstraction scenarios on the lens.

4.1 Methodology

Numerical modeling is an iterative process that integrates a specific conceptual model through the geometry and assignment of the hydraulic properties of the units and boundary conditions. For the numerical methodology, the following iterative approach has been used:

Firstly, after reviewing and analyzing all available information the conceptual model is defined. The conceptual model includes determining the 3D geometry of the different hydrogeological units, their parametrization, and characterizing the flow mass balance (inflows and outflows) of the system. Once the conceptual model is established, different simulations have been performed:

- **Quasi-Steady State Model.** This model simulates the dynamic equilibrium of the freshwater lens. The purpose of this model is to determine stable initial conditions for the transient simulations.

- **Transient Models.** Using the head and concentration distribution resulting from the quasi-steady state model, the Transient Model simulates transient effects to reproduce the historical response of the freshwater lens and head distribution to variations in the recharge, sea level and abstraction from January 2007 to November 2022, because sea level data are only available for that period.
- **Future Scenarios.** Once the previous models adequately reproduce the historical behavior of the system and present plausible hydrogeological parameters, future scenarios are simulated for predicting impacts on the freshwater lens and time recovery under transient conditions, including changes in recharge, drought periods, sea level changes and inundation events.

Both the Quasi-State Model and the Transient Model were calibrated manually through a trial-and-error procedure and subsequently validated using head and concentration data at the monitoring and abstraction wells.

4.2 Numerical code

COMSOL Multiphysics v6.1 (COMSOL, 2020) with the subsurface flow module was used to develop a three-dimensional model to simulate variable-density groundwater flow and solute transport.

COMSOL Multiphysics is a Multiphysics simulation platform that solves fully coupled Multiphysics and single physics based on Finite Element Analysis and Partial Differential Equations (<https://www.comsol.com/>). COMSOL supports structured and unstructured meshes with different element types including tetrahedra, hexahedra, and prisms. The Subsurface Flow Module allows to simulate flow, solute, heat and reactive transport problems in porous media, as well as coupled processes such as variable density flow and solute transport. The governing equations are detailed in Appendix B.1.

4.3 Geometry

The total area of the model domain is 4.4 km² (approximately 2400 km width, and 3500 km length) and covers the Laura area located at the western end of the atoll. The model includes the emerged portion and extends below the ocean and the lagoon (submerged portions) to minimize the impact of the aquifer truncation at the lateral boundaries on the prediction of the freshwater lens. The model extends from the land surface to a maximum depth of - 50 m to include the Upper and Lower Sediments, and part of the Lower Limestones, see Figure 4-1.

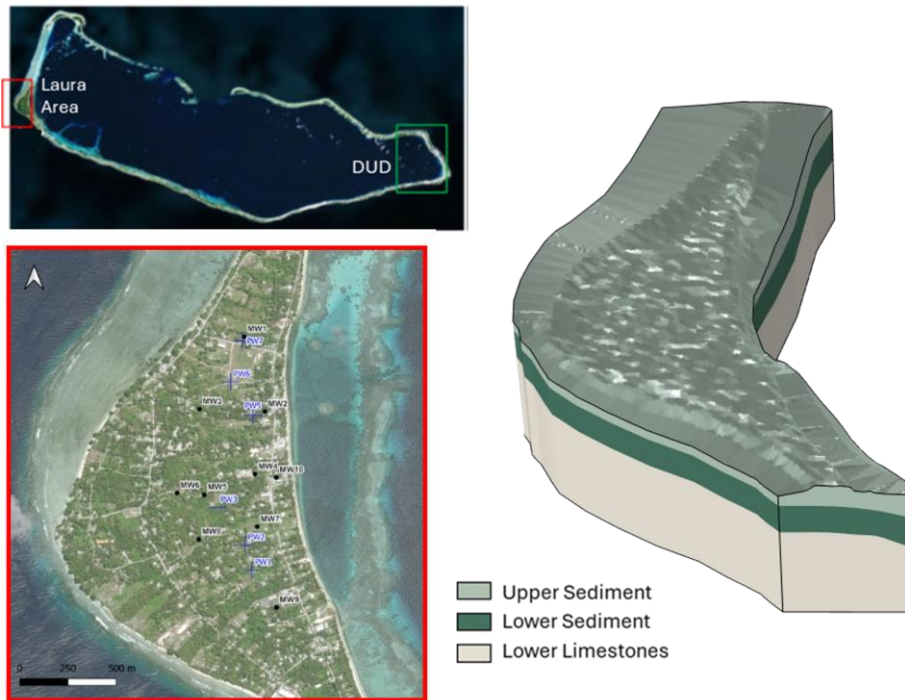


Figure 4-1: (Left) Majuro Atoll and Laura at the western end, and (Right) model domain.

4.4 Spatial and temporal discretization

The model domain was discretized using an unstructured mesh with a total of 382,396 prisms. The mesh was constrained vertically by the contact between the different hydrogeological units: Upper Sediments, Lower Sediments and Lower Limestone.

The element size in the vertical dimension decreases in the upper portion of the system to simulate accurately the thickness of the freshwater lens. Thus, the vertical element size ranges from 0.13 m to 15 m for the Upper Sediments, from 2.6 m to 15 m for the Lower Sediments and from 3.5 to 15 m for the Lower Limestones.

In the horizontal dimension, the mesh was refined near the observation and pumping wells and along the coastline where higher concentration gradients are expected. This refinement is a balanced compromise between precision and computation efficiency that allows to reproduce properly the dynamics of the system and capture the large-scale heterogeneity of the system, while keeping the computational effort tolerable. The top of the model reproduces the topography obtained from Palaseanu-Lovejoy et al. (2018).

Several transient simulations have been defined to calibrate the numerical model and simulate the future scenarios. In all the cases, an adaptive time-stepping scheme was used. The

adaptive time-stepping scheme allows the solver to automatically adjust the time step with an appropriate length based on the change in the primary variables (head and concentration, in this case) between two consecutive time steps. This approach ensures accurate and efficient simulations while maintaining convergence.

- Quasi-Steady State Model.

This model simulates 100 years with a maximum time step of 30 days to determine stable initial conditions for the transient simulations. This simulation was run until quasi steady state was reached. That is, no changes in head, salinity and mass balance were observed throughout the domain at the end of the simulation.

- Transient Model.

Using the steady-state simulation as initial conditions, two different transient simulations were defined to calibrate the historical system behavior at different time scales. First, a transient simulation was performed to simulate the head response to tidal effects. This simulation covers a period of 5 months (from 15/01/2008 to 15/05/2008) with a maximum time step of 1 hour to reproduce the hourly HYCOS campaign (Hourly Transient Model). Then, a longer time scale simulation was defined with a maximum time step of 1 day to reproduce the historical response of the freshwater lens to variations in the recharge, sea level and abstraction from January 2007 to November 2022 (Daily Transient Model).

- Future Scenarios.

The predictive simulations cover a period of approximately 18 years (from November 2022 to September 20238) with a maximum time step of 1 day to predict future climatic and abstraction impacts on the freshwater lens.

Table 4-1: Period and maximum time step for the different transient simulations.

Simulations		Start	End	Maximum time step	Inputs
Quasi-Steady State Model		15/01/1908	15/01/2008	30 days	R = constant SL = constant Abs = constant
Transient Model	Hourly	15/01/2008	15/05/2008	1 hour	R = daily SL = 10 min Abs = daily
	Daily	01/01/2007	08/11/2022	1 day	R = fortnightly SL = daily Abs = daily

Simulations	Start	End	Maximum time step	Inputs
Future Scenarios	08/11/2022	15/09/2038	1 day	R = fortnightly SL = daily Abs = daily

^a R – Recharge, SL – Sea level and Abs – Abstraction.

4.5 Boundary conditions

The groundwater dynamics of the system are mainly controlled by the recharge from rainfall and by the sea level fluctuations and abstraction.

4.5.1 Recharge

Precipitation within the study area is the primary source of groundwater recharge. The recharge from rainfall (evaluated in chapter 3.4) was implemented in the numerical model by a specified flux boundary condition with a concentration of the incoming water equal to 0 on the emerged portion of the system. Along the ocean side, a zone with decreased recharge with a reduction of 10% has been defined due to the existence of beach-rock and reef-plate outcrops (Upper Limestones) that cover parts of the west of the atoll (Anthony, 1985), see blue zone in Figure 4-2.

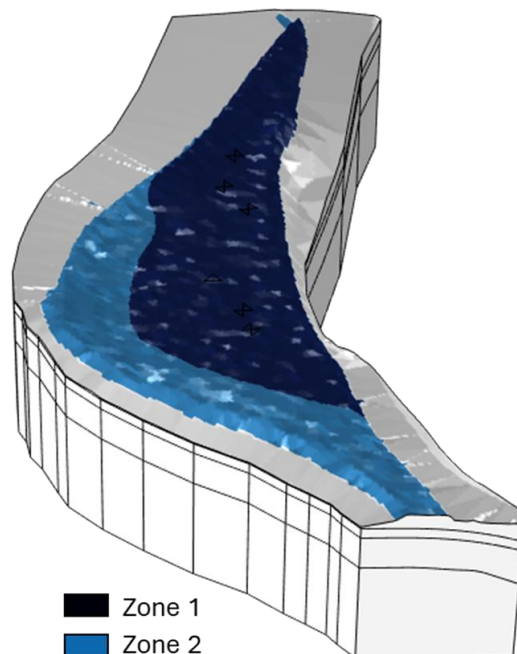


Figure 4-2: Recharge zonation defined in the numerical model. Zone 2 considers a decreased recharge with a reduction of 10%.

For the Quasi-Steady State Model, a constant recharge of 2474 mm/y was considered (average recharge for the period from 1951 to 2023).

However, a different approach was used for the Hourly and Daily Transient Models and for the future scenarios. This is because daily head records show little correlation with rainfall events. This behaviour might be attributed to storativity effects. Thus, unconfined aquifers usually are much more compressible than confined aquifers. The presence of beds of fine-grained compressible materials in the Upper Sediments may induce a rather slowly movement of the recharge front in the shallower portion of the system (few meters from the surface) leading to dampened head responses. Similar delay, named as ‘delayed gravity response’, has been observed in pumping tests performed in unconfined aquifers (Neuman, 1972). As a result, the recharge appears to be diffuse and head variations are mainly controlled by sea-level changes and tides, see(Figure 4-3. Because this effect cannot be captured with a regional scale model, a fortnightly recharge was implemented in the Transient model as well as for the future scenarios in order to simulate a more diffuse (non-instantaneous) recharge.

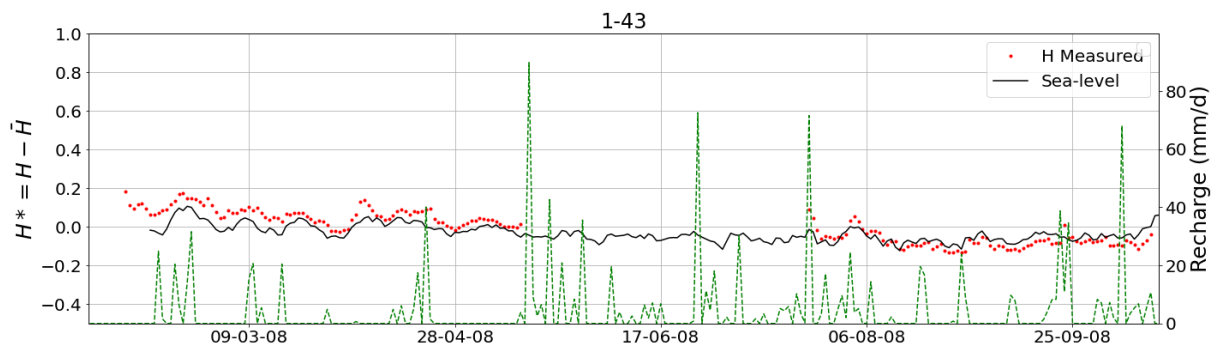


Figure 4-3: Daily head records at piezometer 1-43 (red dots), daily average sea level (black line) and estimated recharge (green line) for the period from 01/09/2008 to 15/12/2008.

4.5.2 Connection with the ocean and lagoon

The connection with the ocean at the west of the island and with the lagoon to the east along the intertidal and submerged zones were represented with a nonlinear Cauchy boundary condition accounting for seepage faces. The same boundary condition was assigned in the northern and southern boundaries. Thus, the inflow of seawater and groundwater discharge is calculated as:

$$\begin{cases} Q = \alpha(H_{sl} - h_i) & H_{sl} > z \\ Q = \alpha(z - h_i) & H_{sl} < z < h_i \\ Q = R & H_{sl} < z > h_i \end{cases}$$

Where h_i is the calculated head at the node i , H_{sl} is the prescribed external head which corresponds to the hourly (Hourly Transient Model) or the daily average (Daily Transient Model) sea level and α is the leakage coefficient [L^2T^{-1}]. The leakage coefficient, often referred to as the conductance, accounts for the resistance to groundwater-surface water interaction below the ocean bed. Thus, three cases may arise, see Figure 4-4: (1) if the node is below sea level ($H_{sl} > h_i$), two possibilities arise: seawater inflow (positive Q) or submarine groundwater discharge (SGD, negative Q), depending on the term $(H_{sl} - h_i)$, (2) if the node is above sea level and the calculated head at the node is higher than its elevation ($h_i > z > H_{sl}$) seepage occurs, and flow moves out of the domain, and (3) if the node is above sea level and the head at the node is lower than its elevation, a prescribed flow equal to the recharge is applied.

The leakage coefficient represents the resistance of the interface between the free water (ocean or lagoon) and the aquifer. A high value of α represents a small resistance to flow between the ocean and the aquifer and the boundary condition is equivalent to a Dirichlet boundary condition (prescribed head), whereas $\alpha = 0$ represents a non-conductive interface between the ocean and the aquifer and then the boundary condition is equivalent to a Neumann boundary condition (prescribed zero flux). The value of the leakage coefficient was manually calibrated in the Quasi-Steady State Model in order to reproduce the freshwater lens shape. Based on the calibration process, the leakage coefficient was set to $10^{-5} \text{ m}^2/\text{d}$.

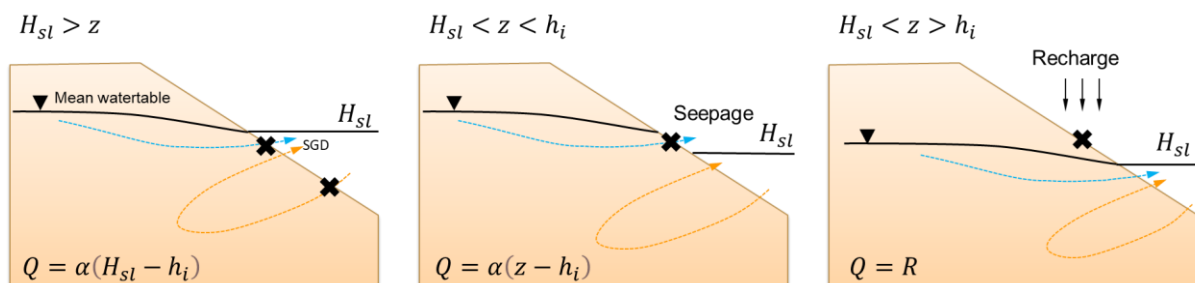


Figure 4-4: Boundary condition to represent the contact with the ocean and lagoon.

A nondispersion boundary condition has been defined for transport. Thus, the concentration of the incoming water is set to that of seawater (normalized concentration of $C=1$) for portions of the boundary where water is flowing into the domain. In the outflowing portion of the boundary, no concentration is specified since the water leaves the model domain with the resident concentration at each node.

4.5.3 Bottom of the model

The model domain extends from the land surface to a maximum depth of - 50 m below sea level. This choice was motivated by the fact that increasing the depth of the domain introduces an uncertainty in the hydraulic parameters of the materials of the Lower Limestones and would increase in the number of elements leading to a high computational cost. Moreover, the area of interest primarily lies within the Upper and Lower Sediments where the freshwater lens is developed. However, inflows and outflow are expected through the bottom boundary. To account for these inflows/outflows, a Cauchy boundary condition was implemented on the bottom of the model. Thus, similar to the connection with the ocean and the lagoon, the inflow or outflow through this boundary is calculated as $Q = \beta(H_{Ext} - h_i)$, where β is a leakage coefficient [L^2T^{-1}], h_i is the calculated head at the node i , and H_{Ext} is the prescribed external head which was assumed to be equal to the equivalent freshwater head at this depth.

The value of β was calibrated in the Quasi-Steady State Model in order to accurately reproduce the shape of the freshwater lens. Thus, a large value for β implies a high inflow from this boundary resulting in a very narrow freshwater lens constrained to the upper portion of the system, whereas $\beta = 0$ represents an impermeable bottom boundary causing the freshwater lens to propagate mainly in the vertical direction without any resistance that results in an overestimation of its thickness. A value of 10^{-8} m²/d was set for the leakage coefficient after the calibration process.

At the nondispersive transport boundary condition imposed at the bottom of the model, the concentration for the incoming water is defined as equal to the one for seawater ($C=1$).

4.5.4 Abstractions

The specific geometry of the of 6 abstractions wells were incorporated in the numerical model, including their horizontal arms, to accurately represent their influence on the freshwater lens system. The specific details of pumping wells (PW) are presented in Appendix B.2.

The model simulates abstractions by prescribing a negative flux at the pumping wells location. This negative flux represents the volumetric flow rate of water being extracted from the aquifer and it is equally distributed across the entire geometry associated to each PW, including the horizontal arms. In the steady-state model, the 2007 abstraction average was used to obtain a consistent initial condition for the state of the lens in 2007. In the transient model, the available temporal evolution was considered using data from 2007 and 2016. For the years between 2007 and 2016, a linear interpolation was applied between the averages of those years. After 2016, the average value from that year was maintained constant until the end of the simulation. This approach ensures a smooth transition in pumping rates over the specified

period, allowing to simulate a representation of groundwater extractions during the year without data.

4.6 Parametrization

The initial parametrization of the numerical model prior to the calibration process was based on the conceptual model defined and also on previous regional models of Laura Island (Jansen, 2021). Table 4-2 shows the initial hydraulic properties defined for each hydrogeological unit.

On the surface of the Laura area more permeable coarser sediments have been found on the ocean side and finer sediments on the lagoon side (Presley, 2005). This variation of the permeability leads to an asymmetrical shape for the freshwater lens. For this reason, a gradual decrease in the permeability was assumed prior to the calibration process in the numerical model from the west to the east for both the Upper and Lower Sediments. For the Upper Sediments the initial horizontal permeability decreased from 80 m/d at the seaside to 30 m/d at the lagoon side, whereas for the Lower Sediments the initial horizontal permeability decreased from 500 m/d at the seaside to 40 m/d at the lagoon side. The horizontal permeability for the Lower Limestone was set to 500 m/d because this unit is highly permeable and homogeneous.

Based on the calibrated parameters obtained in the model developed by Jansen (2021) the porosity was set to 0.2 for the Upper and Lower Sediments and 0.3 for the Lower Limestones. Initial values of 10 m and 5 were considered for the longitudinal and transverse dispersivities, respectively.

Table 4-2: Initial horizontal and vertical permeabilities and porosity implemented in the numerical model.

Unit	Parameter	Value
Upper Sediments	k_h (m/d)	30 - 80
	k_v (m/d)	3 - 15
	ϕ	0.2
Lower Sediments	k_h (m/d)	40 - 500
	k_v (m/d)	4 - 75
	ϕ	0.2
Lower Limestone	k_h (m/d)	500
	k_v (m/d)	50
	ϕ	0.3

4.7 Initial conditions

Initially, for the Quasi-Steady State Model hydrostatic pressure was set at each node with seawater concentration and zero pressure for all nodes along the top boundary, so that the simulation begins fully saturated of seawater. The resulting head and concentration distributions were then imposed as initial conditions for the Hourly and Daily Transient models. Finally, results obtained from the calibrated Transient Model (b) were used as initial conditions for all the future scenarios simulated.

4.8 Observations wells

The numerical model contains 33 observation wells located at different depth according to the placement of their screens, see details in Appendix B.3 . The pumping wells are also included as observations wells in simulations. At each observation well, the model computes two state variables: the hydraulic head and the concentration.

However, it should be pointed out that head time series-data from the HYCOS campaign, which comprises 11 boreholes equipped with multi-level observation wells, show clear evidence of substantial vertical gradients, with water level differences of about 0.5 m. While most of these gradients are downward, there are instances of upward gradients in some multi-level observation wells, as illustrated in Figure 4-5. These upward vertical gradients are likely attributable to small-scale heterogeneities.

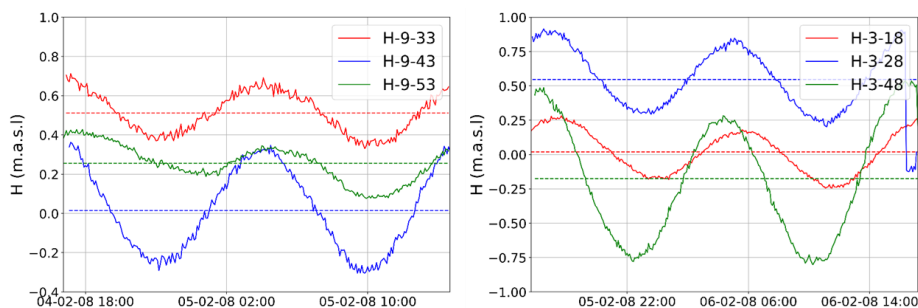


Figure 4-5: Head responses to tidal oscillations observed during the HYCOS campaign showing the existence of upward vertical gradients.

The scale of the model does not allow to capture these small-scale effects. Therefore, the calibration of the transient hourly model was carried out by comparing the amplitude and lags measurements instead of relying on the piezometric head data measured at the multi-level observation wells.

5 Numerical calibration

First, the numerical model is built based on the conceptual model. A Quasi-State Model is run using to obtain stable initial conditions for the Transient. Then, the different transient models are run and results are compared to actual observations (heads and concentrations). The quality of the fit is evaluated through (i) analysis based on visual inspection of the deviation between measurements and model results, (ii) from calibration statistics and (iii) from the distribution of the residuals (histogram). If the model fails to attain a satisfactory fit, the hydraulic parameters are adjusted manually based on the observed differences. An iterative procedure is followed until a satisfactory level of agreement is achieved between the simulated and observed behaviour of the system. The success of the calibration process relies on the quality and representativeness of the observations used for comparison. Once the previous models adequately reproduce the historical behavior of the system, future scenarios are simulated for predicting impacts on the freshwater lens and time recovery under transient conditions.

5.1 Quasi-Steady State calibration

Stable initial conditions (in terms of heads and concentrations) are required for conducting the transient simulations. Therefore, the Quasi-Steady State model was calibrated in order to obtain proper representation of the initial freshwater lens and head distribution.

For the steady state simulation, the permeabilities and storativity of the different Hydrogeological Units, the dispersivities and the conductance of the non-linear Cauchy boundary conditions (lateral and bottom) were calibrated.

The resulting geometry of the freshwater lens was qualitatively compared with the existing Electrical Resistivity Tomography (ERT) profiles, the HYCOS measurements as well as the geometry defined in the conceptual model (Figure 3-12). To validate the resulting head distribution, model results were compared with the piezometry defined by Hamlin and Anthony (1987) because the HYCOS measurements are strongly influenced by tidal oscillations. However, the piezometry defined by Hamlin and Anthony (1987) shows heads that fell outside the range measured in HYCOS, in particular at the north and west of the system. Therefore, in these areas a qualitative rather than quantitative comparison of the heads was performed.

Figure 5-1 shows the resulting freshwater lens and the comparison with the geophysical profiles. Note that the model matches reasonably well the asymmetrical geometry of the freshwater lens with the thickest portion located on the lagoon-side of the island.

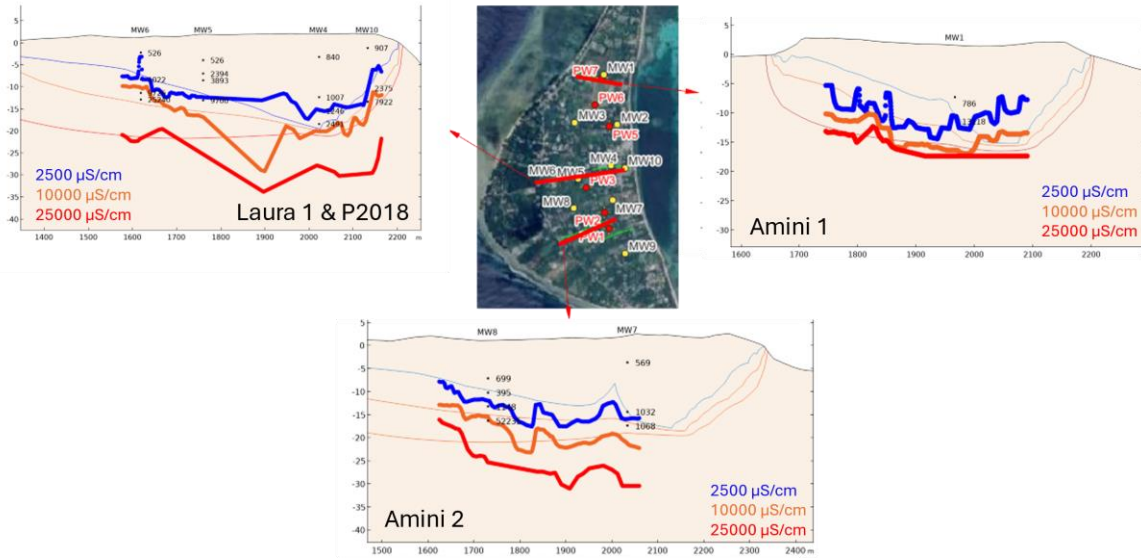


Figure 5-1: Cross sections showing the electrical conductivity inferred from the geophysical profiles (solid lines) and results from the numerical model (dashed lines).

Figure 5-2 illustrates the resulting piezometry obtained from the numerical model and the one defined for April 1973 (Hamlin and Anthony, 1987). Note that the piezometric distribution is in good agreement with the piezometry defined, with the highest heads at the centre of the island and higher hydraulic gradients and flow towards the lagoon.

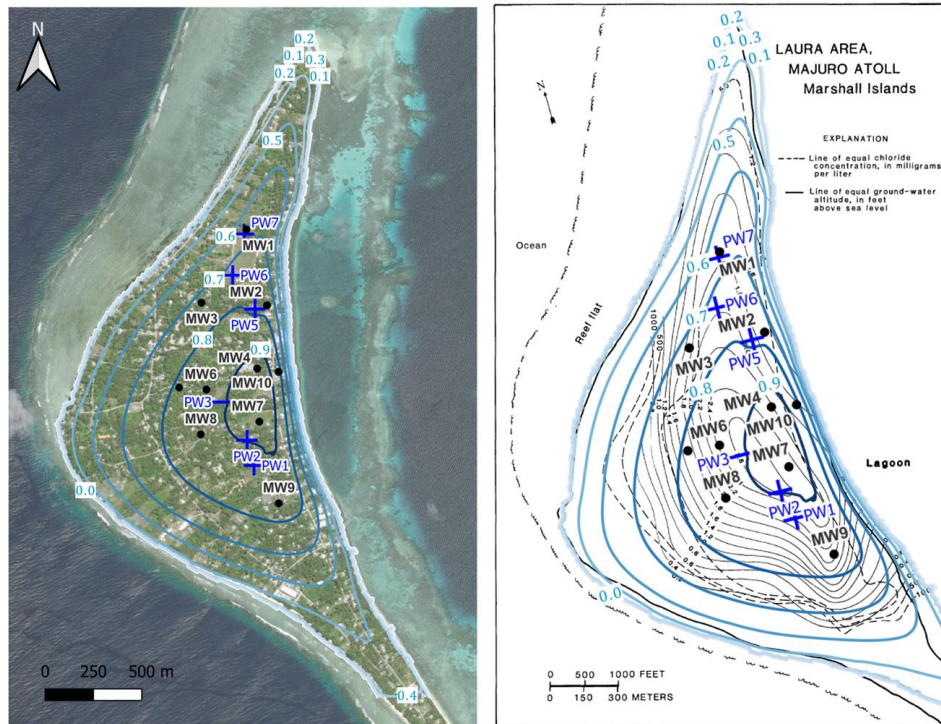


Figure 5-2: (left) Head distribution obtained from the numerical model and (right) the one defined for April 1973 by Hamlin and Anthony (1987).

In general, the model reproduces satisfactorily the head distribution controlled by the recharge and the geometry of the island, so that groundwater flows from the centre of the island towards the ocean and the lagoon. On the other hand, the model captures the geometry of the freshwater lens that is wide in the middle part of the island with narrow and thin ends at the south and the north.

5.2 Transient calibration

For the transient simulations, the permeabilities and storativities of the different Hydrogeological Units were calibrated to reproduce the historical system behavior at different time scales.

5.2.1 Hourly Transient Model

First, a short-term transient simulation was calibrated, Hourly Transient Model, to simulate head responses to tidal fluctuations. This simulation covers a period of 5 4 months (from 15/01/2008 to 15/05/2008) with a maximum time step of 1 hour.

As mentioned in Chapter 4.8, the calibration of the transient hourly model was carried out by comparing the amplitude and lags measurements instead of relying on the piezometric head data measured at the multi-level observation wells.

Figure 5-3 illustrates the comparison between measured and computed normalized heads, obtained by subtracting the mean value ($H^* = H - \bar{H}$), at different multi-level observation wells. The first observation that becomes apparent from the figure is that a reasonable fit between simulated and measured heads is obtained from the calibration. The simulated heads are consistent with measured data for most observation wells, showing similar responses to tidal fluctuations.

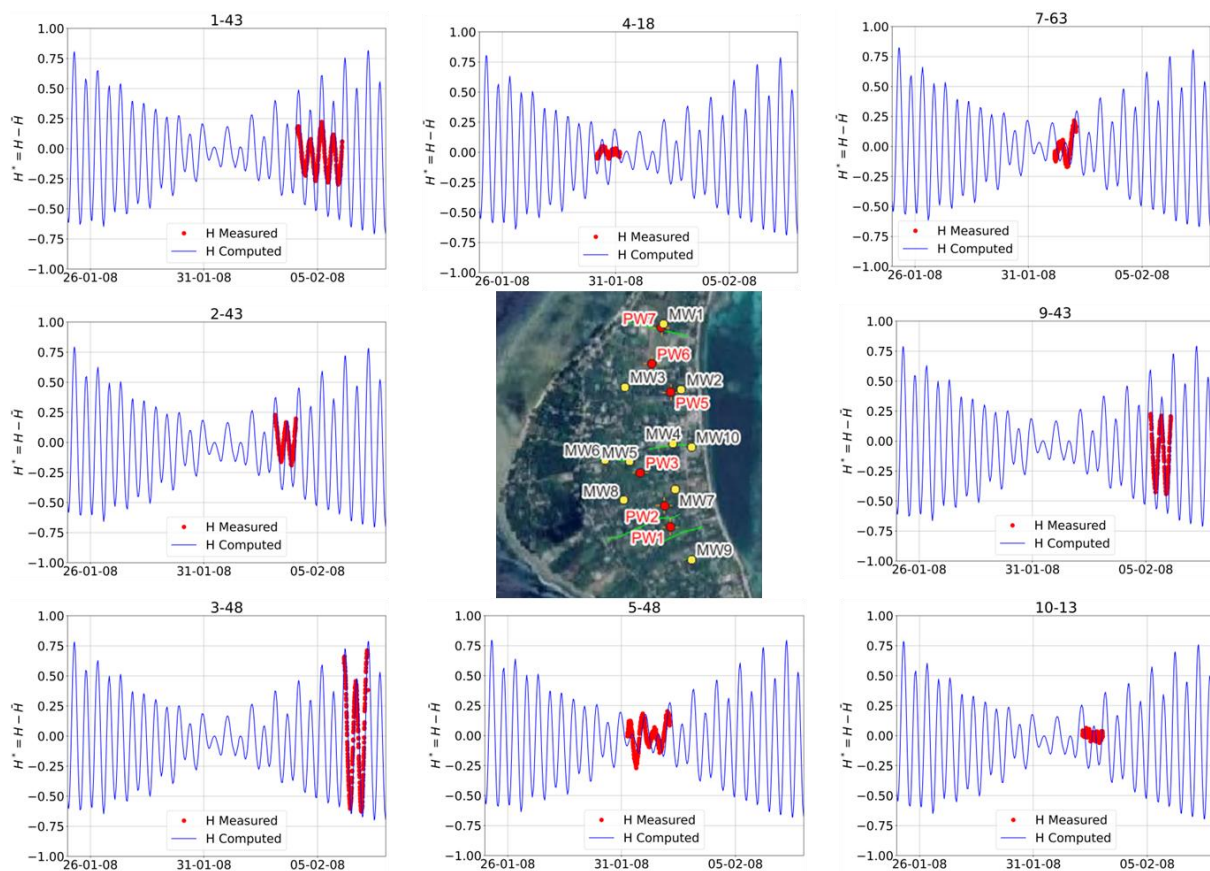


Figure 5-3: Calculated (blue line) and measured (red dots) normalized heads at eight selected shallow multi-level observation wells from the calibrated Hourly Transient Model.

However, some small but evident deviations are observed at some multi-level observation wells (see, for example wells 1-43 and 2-43). Thus, for some monitoring wells, the model captures properly the lag, it tends to predict larger amplitudes compared to the field measurements at these points. This discrepancy suggests that in this area the model overestimates the connection between the aquifer and the ocean.

Strong correlations with the tides and fluctuations in the sea level are observed in multi-level observation wells located relatively far from the coastline (for example, MW5). This is due to the high permeability of the Lower Limestones that promotes a fast horizontal and then vertical propagation of sea level fluctuations, inducing a strong impact on the head distribution. However, the large storativity of the Upper Sediments promotes a nonuniform time-dependent velocity field, resulting in a vertically delayed groundwater flow response.

This complex subsuperficial and deep connection observed between the ocean-lagoon and the system is induced by vertical heterogeneity of the hydraulic properties at small scale. However, given the regional scale of the model, it is unable to reproduce this complexity. On the other hand, the vertical heterogeneity of the Upper and Lower Sediments cannot be inferred from the available geological information. Therefore, additional field studies are required to characterize properly the vertical heterogeneity of the system and elucidate the connection between the ocean-lagoon and the aquifer.

5.2.2 Daily Transient Model

The Daily Transient Model simulates the historical response of the freshwater lens to variations in the recharge, sea level and abstraction from January 2007 to November 2022, with a maximum time step of 1 day.

The quality of the head and concentration fits has been evaluated through analysis based on visual inspection of the differences between head measurements and computed heads, from statistics that quantify the deviation between observed data and computed results, and from the distribution of the residuals (histogram).

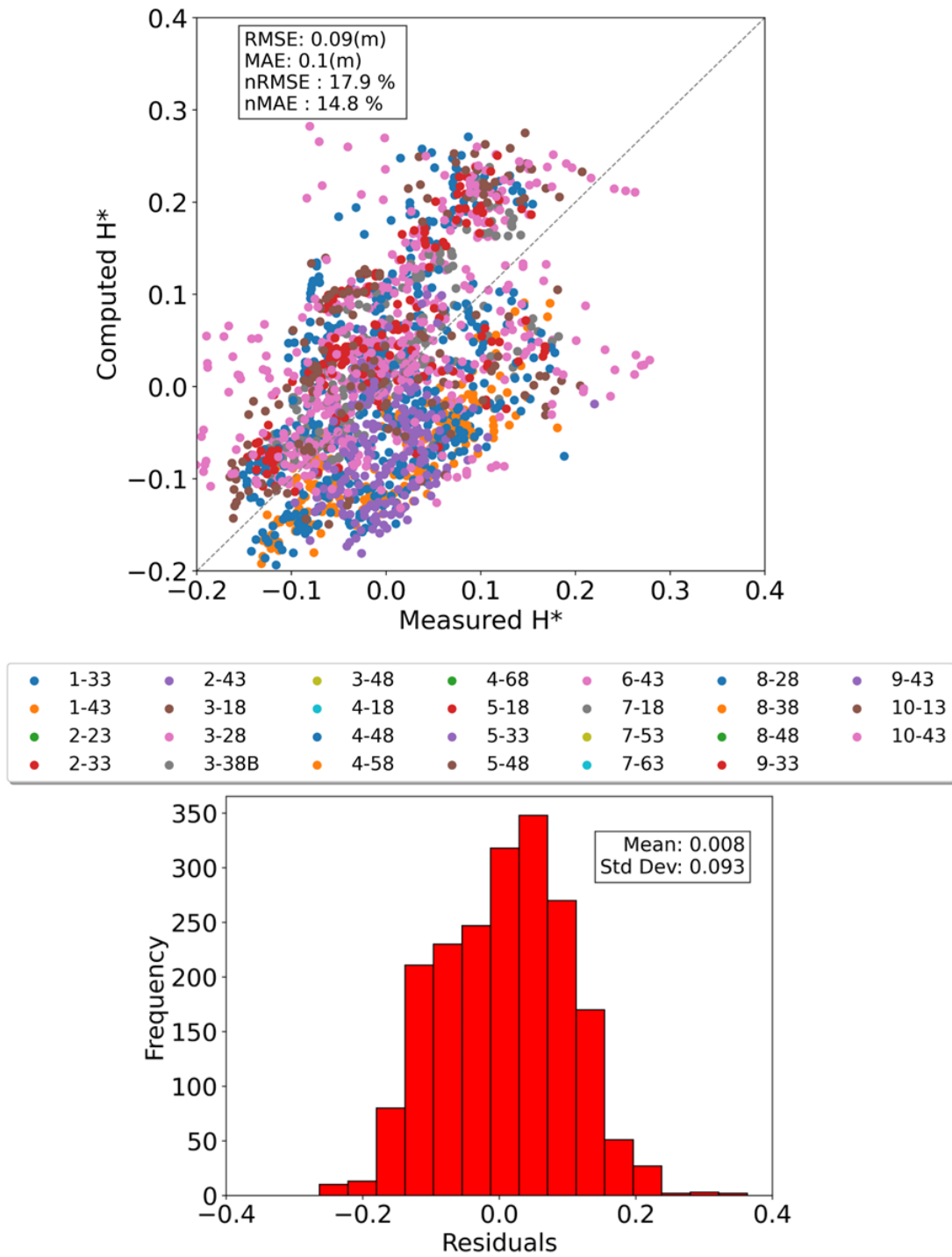


Figure 5-4: Modelled versus observed heads (top) and frequency distribution of the residuals (bottom) for the calibrated Daily Transient Model.

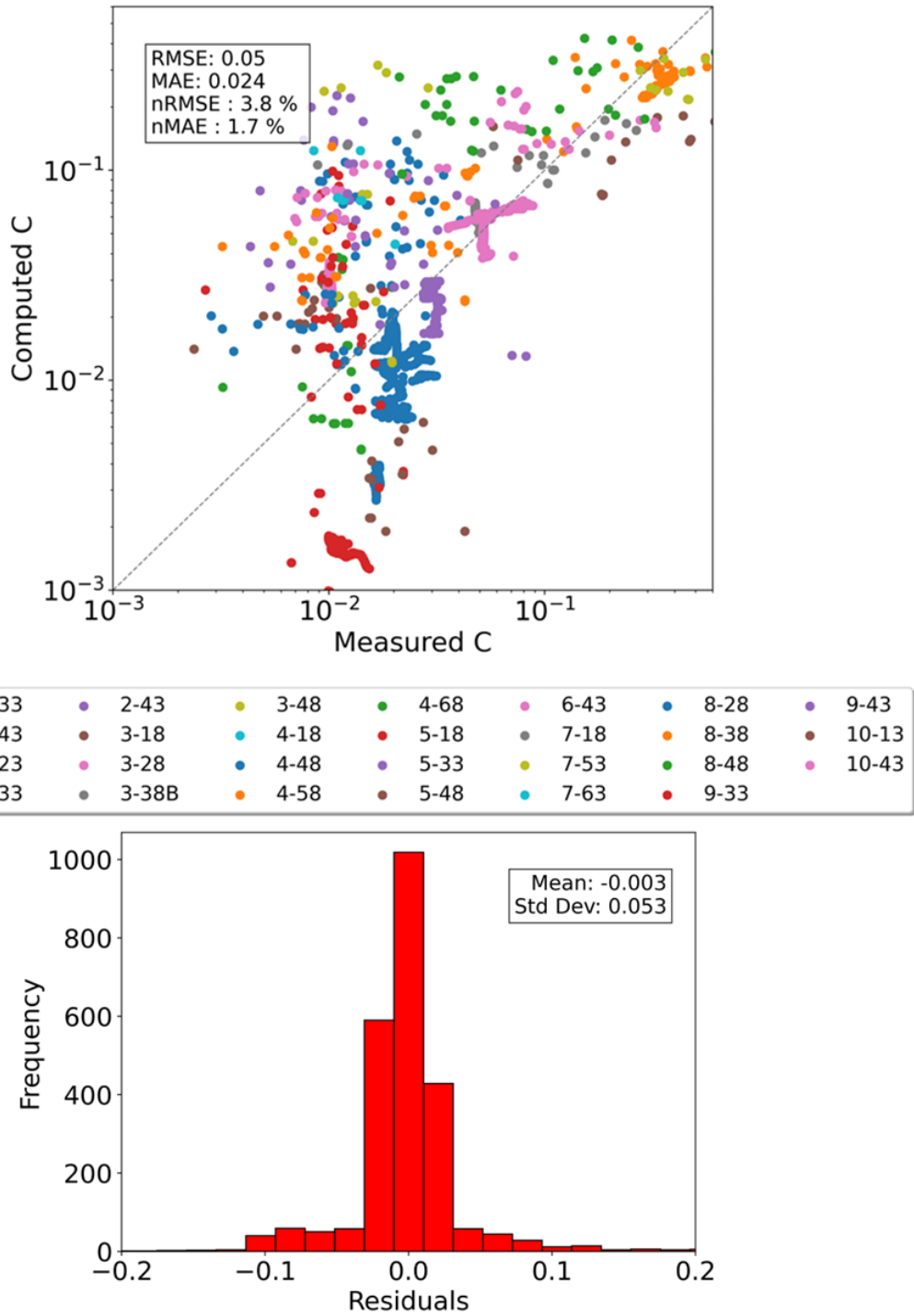


Figure 5-5: Modelled versus observed concentrations (top) and frequency distribution of the residuals (bottom) for the calibrated Daily Transient Model.

Figure 5-4 and Figure 5-5 illustrate the head and concentration fits and their residuals distributions obtained from calibration of the Daily Transient Model. Satisfactory head fits are obtained from the calibration such that calculated heads and field measurements follow the unity line. Moreover, the residual histogram shows a normal distribution with a mean value close to zero and the 90% of the residuals ranging between -0.1 and 0.1 m. A reasonable fit is also obtained for the concentrations, given the heterogeneous nature of the system and the high temporal dynamics involved.

Table 5-1 illustrates the statistics obtained from the calibration of the Daily Transient Model. The absolute mean error (MAE) values for heads and normalized concentrations are relatively small, standing at 0.1 m and 0.024, respectively. These errors are considered adequate for a regional scale model. Moreover, the normalized root mean square error (normalized RMSE) for concentrations is lower than 5 %, indicating minimal errors between computed and measured concentrations.

Comparison of these statistics with previous studies on island lens modelling suggests that the errors between the model results and measurements are within an acceptable range. For instance, Post et al., (2018) obtained a normalized RMSE of approximately 10% from the calibration of the model of the Bonriki Island (Kiribati), while Ataie-Ashtiani et al., (2013) obtained a normalized RMSE of 21% from the modelling and calibration of the Kish Island (Persian Gulf).

Table 5-1: Calibration statistics for the calibration of the Daily Transient Model.

Statistics	Heads	Concentration
RMSE	0.09 m	0.05
MAE	0.1 m	0.024
Normalized RMSE (%)	17.9 %	3.8 %
Normalized MAE (%)	14.8 %	1.7 %

The comparison between measured and computed normalized heads at different observation wells for the HYCOS and MCAP daily campaigns are shown in Appendix C.1 (Figure 10-2 and Figure 10-3). The daily data show small heads variations mainly controlled by sea level fluctuations. Note that the model reasonably matches the temporal trends in heads in all the multi-level wells, with maximum differences of around 20 cm. Therefore, although the model overestimates the amplitude of hourly tidal responses in some wells, it captures properly the daily fluctuations and long-term behaviour.

Measured and computed normalized concentrations for all the multi-level wells as well as for the pumping wells is illustrated in Appendix C.1 (from Figure 10-4 to Figure 10-8). Salinity measurements exhibit highly dynamic variations, indicating vertical movements of the lens due to seasonal and long-term rainfall variations. Thus, during extended dry periods, such as in 2016, the lens becomes thinner, leading to a generalized increase in concentrations measured at all the multi-level wells. It is important to note that pumping slightly affects the concentration at the multi-level wells. Thus, while pumping increases during dry periods, the rise in pumping causes saltwater to move upwards towards the wells, resulting in a localized decrease in lens thickness around the pumps (upconing effects). Plots with computed and measured normalized heads and concentrations for each well is included in Appendix C.1 (from Figure 10-9 to Figure 10-12).

The comparison between simulated concentration and measurements indicates that, overall, the model accurately depicts major features of the concentration distribution and its dynamics for all the wells. However, during dry periods the model appears to be overestimating (e.g., well 2-43 and well 3-28) or underestimating (e.g., well 5-48 and well 6-43) the amplitude of concentration variations at some multi-level wells. These discrepancies between modelled and observed groundwater salinities might indicate the existence of small-scale heterogeneity or local variations in the thickness of the Hydrogeological Units, not fully accounted for in the numerical model.

5.3 Calibrated parameters

The initial and calibrated parameters are shown in Table 4-2 and the spatial distribution of the calibrated permeability is illustrated in Figure 5-6. Two key observations arise from the spatial distribution of the permeability: (i) for the Upper and Lower Sediments the hydraulic conductivity varies spatially with higher values on the ocean side, and (ii) the Upper Sediments present a lower permeability compared to the Lower Sediments. Also note that during the calibration process, the permeabilities of the Lower Sediments decreased on the lagoon side compared to the values initially defined in the conceptual model. This adjustment was necessary as the initial parameters led to an overestimation of the concentrations in this area of the island and underestimation of the freshwater lens thickness.

Additionally, the calibrated permeability values for both the Upper and Lower Sediments are in accordance with the values inferred from the tidal analysis. Thus, the tidal analysis results in lower permeabilities on the lagoon side, ranging from 1 to 0.05 m/d for the multi-level wells 10 and 2, and higher permeabilities on the ocean side, ranging from 100 to 20 m/d for the multi-level wells 3, 5, 6 and 8 (see Figure 3-11 in chapter 3.6.4).

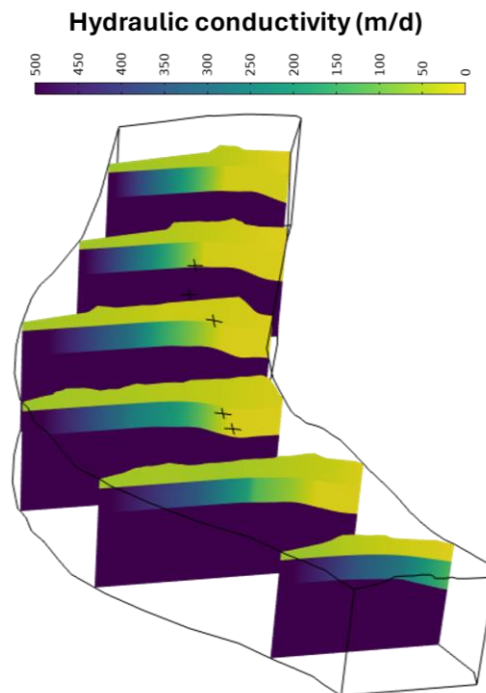


Figure 5-6: Spatial distribution of the horizontal permeability obtained from the calibration process of the Daily Transient Model.

During the calibration process, it was observed the shape of the freshwater lens is highly sensitive to the permeability of the Lower Sediments. Thus, higher permeabilities resulted in a shallower interface.

On the other hand, no significant changes to transport parameters were required to improve the simulation of the freshwater–seawater transition zone location and thickness. Only the dispersivities were decreased according to Jansen (2021).

Therefore, all the calibrated parameters are consistent with the conceptual model and previous studies of Laura, and the obtained spatial distribution in the permeability provides enough variability to achieve adequate matches to observations.

Table 5-2: Values of initial and calibrated model parameters.

Unit	Parameter	Initial value	Calibrated value
Upper Sediments	k_h (m/d)	30 - 80	10-80
	k_v (m/d)	3 - 15	5-40
	ϕ (-)	0.2	0.2
	α_L, α_T (m)	10, 5	1.37, 0.37
Lower Sediments	k_h (m/d)	40 - 500	40 - 600
	k_v (m/d)	4 - 75	0.2 - 75
	ϕ (-)	0.2	0.2
	α_L, α_T (m)	10, 5	1.37, 0.37
Lower Limestone	k_h (m/d)	500	500
	k_v (m/d)	50	50
	ϕ (-)	0.3	0.3
	α_L, α_T (m)	10, 5	1.37, 0.37

6 Sensitivity analysis

To assess the influence of various factors on the Laura Island freshwater lens, a parametric sensitivity analysis was conducted to define the key parameters controlling the system dynamics and to evaluate their impact on the results.

Parameters such as hydraulic conductivity, seepage conductance, dispersion, porosity, or abstractions were included in this analysis. Each parameter was individually varied within a relevant range while holding the others constant to emphasize their individual effect on the results. This approach allowed us to isolate the individual effects of each parameter on the model outputs. The calibrated model served as the baseline for this analysis. Therefore, the impact of changing the parameters was evaluated by comparing with the results obtained from the calibrated model.

6.1 Hydraulic conductivity

For the analysis of the hydraulic conductivity, six additional simulations were performed by multiplying or dividing the spatial distribution of the permeability for the Upper and Lower Sediments and the Lower Limestones, individually, by a factor of 2.

6.1.1 Upper Sediments

It is important to mention that in this analysis both higher and lower permeabilities compared to the ones defined in the conceptual model and previous studies have been considered to emphasize the individual effect of this parameter on the model results.

Figure 6-1 illustrates the vertical salinity profile of Laura Island freshwater lens under the different hydraulic conductivity fields and Figure 6-2 shows the isoconcentrations for each case.

A decreased hydraulic conductivity field (green lines in Figure 6-2) leads to a slight increase in the freshwater lens thickness up to 20 m and a migration of the lens towards the lagoon compared to the calibrated field. This increase in the freshwater lens thickness is reflected in the freshwater volume, which rise from 2.4 hm³ in the calibrated model to 3.0 hm³ in this simulation. However, despite these changes, the overall shape of the lens remains similar. Conversely, when the hydraulic conductivity field is increased (red lines in Figure 6-2), the freshwater lens becomes more rounded and less thick, with a thickness around 15 m. This indicates a general reduction of the freshwater lens volume compared to the calibrated model, decreasing to 1.6 hm³.

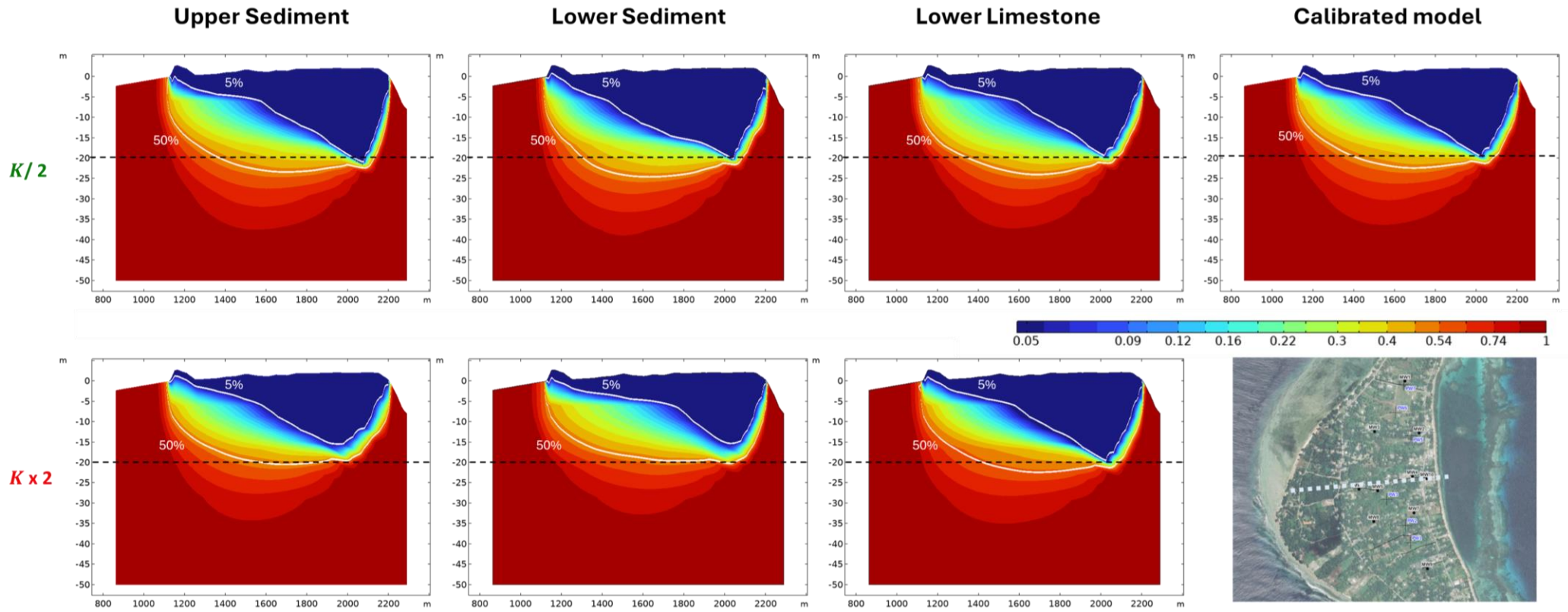


Figure 6-1: Vertical salinity profile in the central part of Laura (Hydraulic conductivity sensitivity analysis). White lines represent 5% and 50% seawater isoconcentration contours. First column corresponds to the upper sediments, the second to the lower sediments, and the third to the lower limestone layer. The calibrated model is presented in the fourth column. Results for decreased ($K/2$) and increased ($K \times 2$) hydraulic conductivity is shown in the first and second rows, respectively.

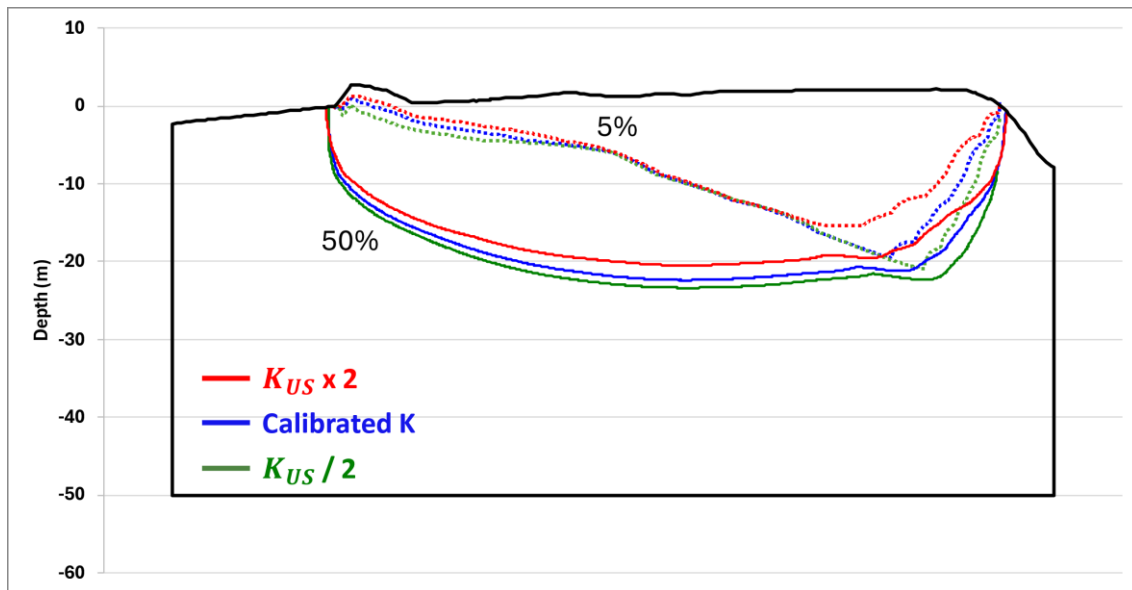


Figure 6-2: Vertical cross section showing the isoconcentration contours of 5% (dotted lines) and 50% (solid lines) of seawater in the central part of Laura Island for the calibrated model (black lines), increasing the permeability of the Upper Sediments (red lines) and decreasing the permeability (green lines).

6.1.2 Lower Sediments

The same as for the Upper Sediments, the permeability field of the Lower Sediments was increased and decreased in a factor of 2. The permeability values reported in previous studies range from 350 to 605 m/d.

Figure 6-1 and Figure 6-3 present the cross-section with the salinity distribution and isoconcentration contours at the central part of the island. Changes in the hydraulic conductivity distribution affect the freshwater lens particularly at the middle part of the island, whereas the lens at the lagoon and ocean sides show small impacts. Similarly to the analysis of the Upper Sediments, an increase in the hydraulic conductivity results in the freshwater lens becoming more rounded and thinner, whereas a decrease causes the lens to increase. Consequently, the volume of the freshwater lens increases to 3.1 hm³ with lower permeabilities and decreases to 1.8 hm³ with higher permeabilities. Note that the freshwater lens is more sensitive to permeability changes in the Lower Sediments compared to the ones in the Upper Sediments.

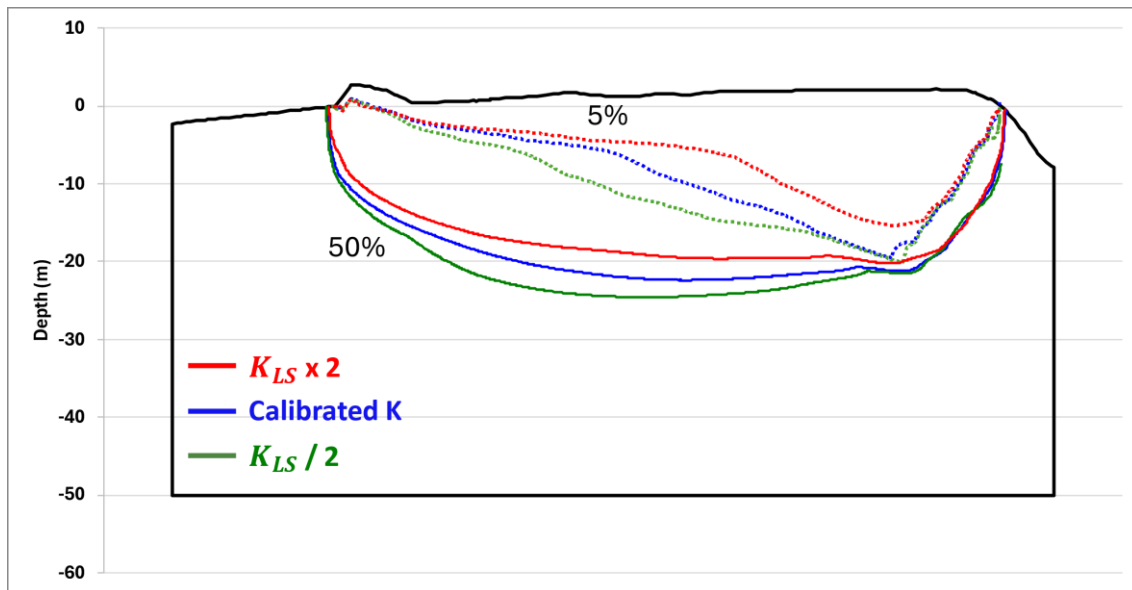


Figure 6-3: Vertical cross section showing the isoconcentration contours of 5% (dotted lines) and 50% (solid lines) of seawater in the central part of Laura Island for the calibrated model (black lines), increasing the permeability of the Lower Sediments (red lines) and decreasing the permeability (green lines).

6.1.3 Lower Limestones

Finally, the sensitivity analysis to the hydraulic conductivity was conducted for the Lower Limestones. Because a homogeneous field was considered in the calibrated model, two additional values were tested in this analysis: 250 m/d and 1000 m/d.

Figure 6-1 and Figure 6-4 display the resulting salinity distributions and isoconcentration contours, respectively. Note that changes in the permeability of the Lower Limestones lead to significant responses in the saltwater end of the interface compared to the ones observed in the freshwater end. Thus, when the hydraulic conductivity of the Lower Limestones is increased the fresher part of the lens migrates slightly downwards, whereas the saltier part migrates upwards, leading to a decrease in the width of the mixing zone. Conversely, when hydraulic conductivity is decreased the width of the mixing zone increases showing a slightly upward migration of the freshwater ends and a downward migration of the saltwater end. Because the freshwater end of the interface remains almost unaltered, small impact in the freshwater volume is observed. Thus, the freshwater volume ranges from 2.3 hm³ for the case of decrease permeability to 2.6 hm³ for the case of increase permeability.

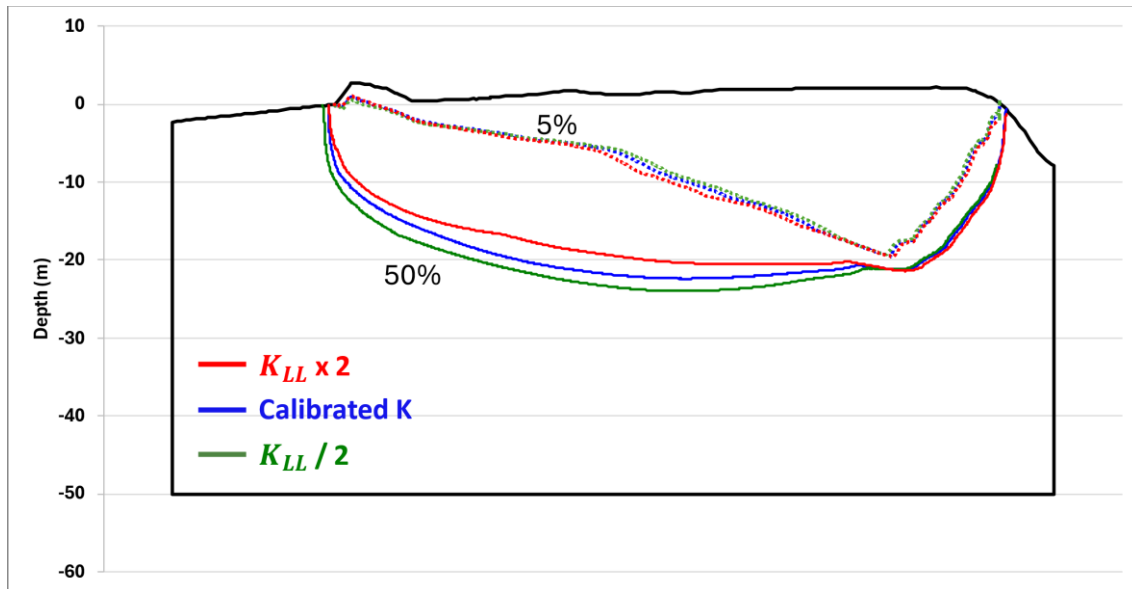


Figure 6-4: Vertical cross section showing the isoconcentration contours of 5% (dotted lines) and 50% (black lines) of seawater in the central part of Laura Island for the calibrated model (black lines), increasing the permeability of the Lower Limestones (red lines) and decreasing the permeability (green lines).

6.2 Seepage conductance

The effect of the conductance or leakage coefficient for the Cauchy boundary condition at the lateral boundaries of the model has been also evaluated. A wide range of values were test from 1×10^{-3} to $1 \times 10^{-6} \text{ m}^2/\text{s}$.

Figure 6-5 shows the freshwater discharge distribution along the coast for different seepage conductance. The figure reveals a clear correlation between conductance and discharge patterns. Thus, the value of the conductance controls the distribution and magnitude of submarine groundwater discharge. Higher conductance leads to a narrower and more concentrated discharge zone inducing a higher outflow of freshwater towards the sea. On the other hand, lower conductance results in a wider and more diffuse discharge zone with lower outflow.

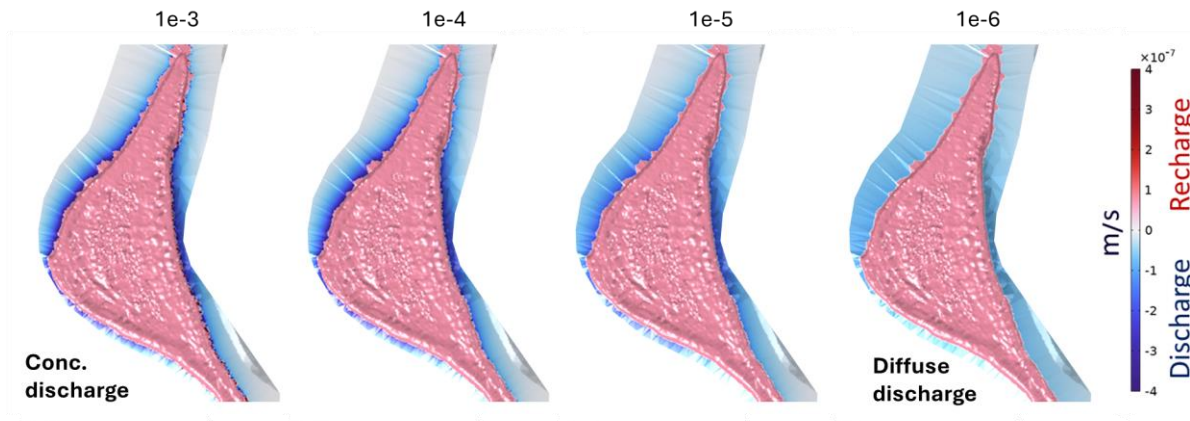


Figure 6-5: Seepage conductance impact over discharge.

6.3 Dispersion

The role of the dispersivities on the numerical results was also evaluated. The values defined for the calibrated model were divided by a factor of 3 and increased in a factor of 5.

Figure 6-6 and Figure 6-7 present the salinity distribution and the isoconcentration contours, respectively, along the central axis of the island for each simulation. As expected, when dispersion is reduced, the width mixing zone decreases, particularly near the lagoon and the freshwater lens migrates downward at the ocean side. Note that numerical instabilities are observed because in this case the Peclet restriction is violated. On the other hand, when dispersion is increased, a very important impact on the freshwater lens is observed. Thus, the mixing zone widens considerably with freshwater concentrated in the upper part of the domain (<5 m), except near the lagoon, where it reaches around 10 m.

Dispersion has a significant impact on the volume of freshwater. Thus, the freshwater volume decreases un order of magnitude from 2.4 hm³ in the calibrated model to 0.24 hm³ when dispersivities are increased and increases to 4.3 hm³ when dispersion is reduced.

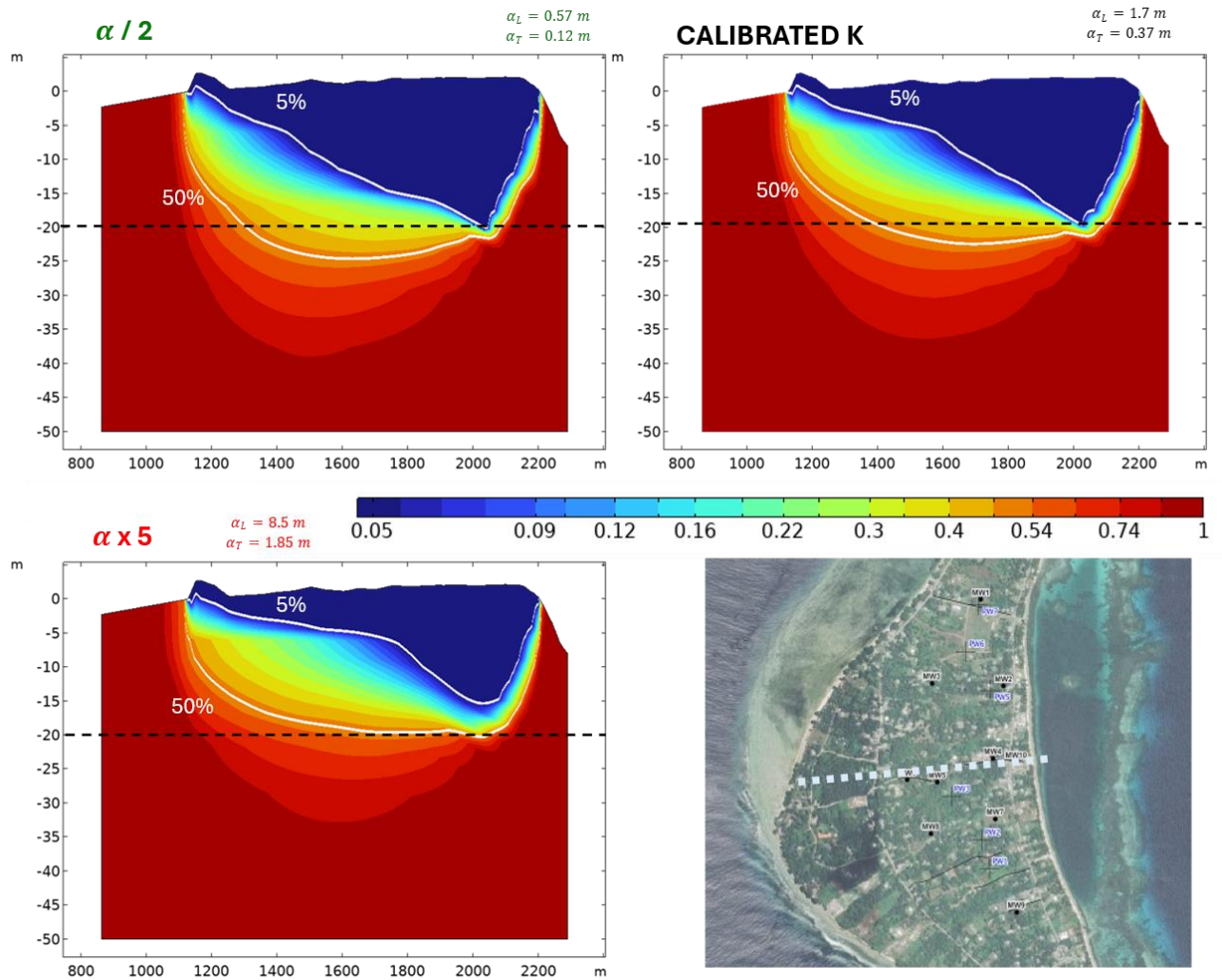


Figure 6-6: Vertical salinity profile in the central part of Laura Island (Dispersion sensitivity analysis). White lines represent 5% and 50% seawater isoconcentration contours.

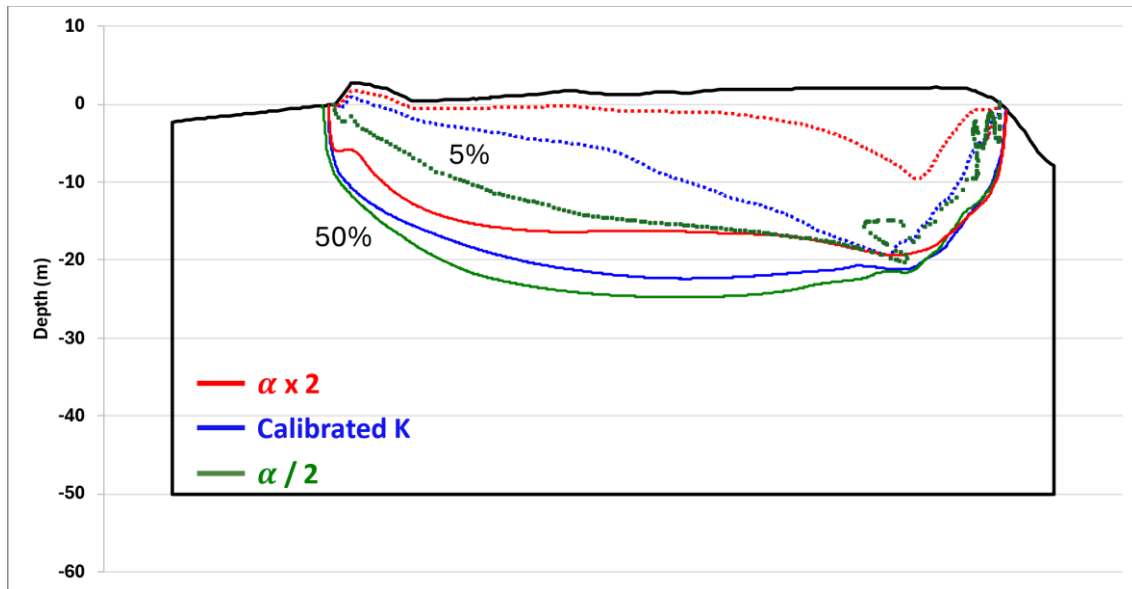


Figure 6-7: Vertical cross section showing the isoconcentration contours of 5% and 50% of seawater in the central part of Laura Island for the calibrated model (black lines), increasing the dispersion (red lines) and decreasing the dispersion (green lines).

6.4 Porosity

In addition to the analysis of the permeability, seepage conductance and dispersion, the effect of the porosity on the model results has been evaluated. Two additional simulations were performed considering a higher porosity (1.5 times the calibrated value) and a lower value (half the calibrated value) for the Upper and Lower Sediments. Figure 6-8 presents simulated salinities at various monitoring wells for each porosity.

Results show an inverse correlation between porosity and salinity. Thus, higher porosity (0.3) leads to smoother and lower salinity peaks in the monitoring wells, whereas lower porosity (0.1) results in sharper salinity peaks. This is because larger porosities induce a larger pore volume that allows a greater dilution of saltwater resulting in smoother salinity fluctuations. On the other hand, small porosities imply more rapid and sharp responses leading to more pronounced salinity peaks during intrusion events.

The volume of the freshwater lens is strongly affected by the porosity showing a linear relationship. Thus, when porosity is 0.1, the volume is halved compared to the calibrated value (0.2), whereas when it is 0.3, results in a 1.5-fold increase, see Figure 6-9.

Results show an inverse correlation between porosity and salinity. Thus, higher porosity (0.3) leads to smoother and lower salinity peaks in the monitoring wells, whereas lower porosity

(0.1) results in sharper salinity peaks. This is because larger porosities induce a larger pore volume that allows a greater dilution of saltwater resulting in smoother salinity fluctuations. On the other hand, small porosities imply more rapid and sharp responses leading to more pronounced salinity peaks during intrusion events.

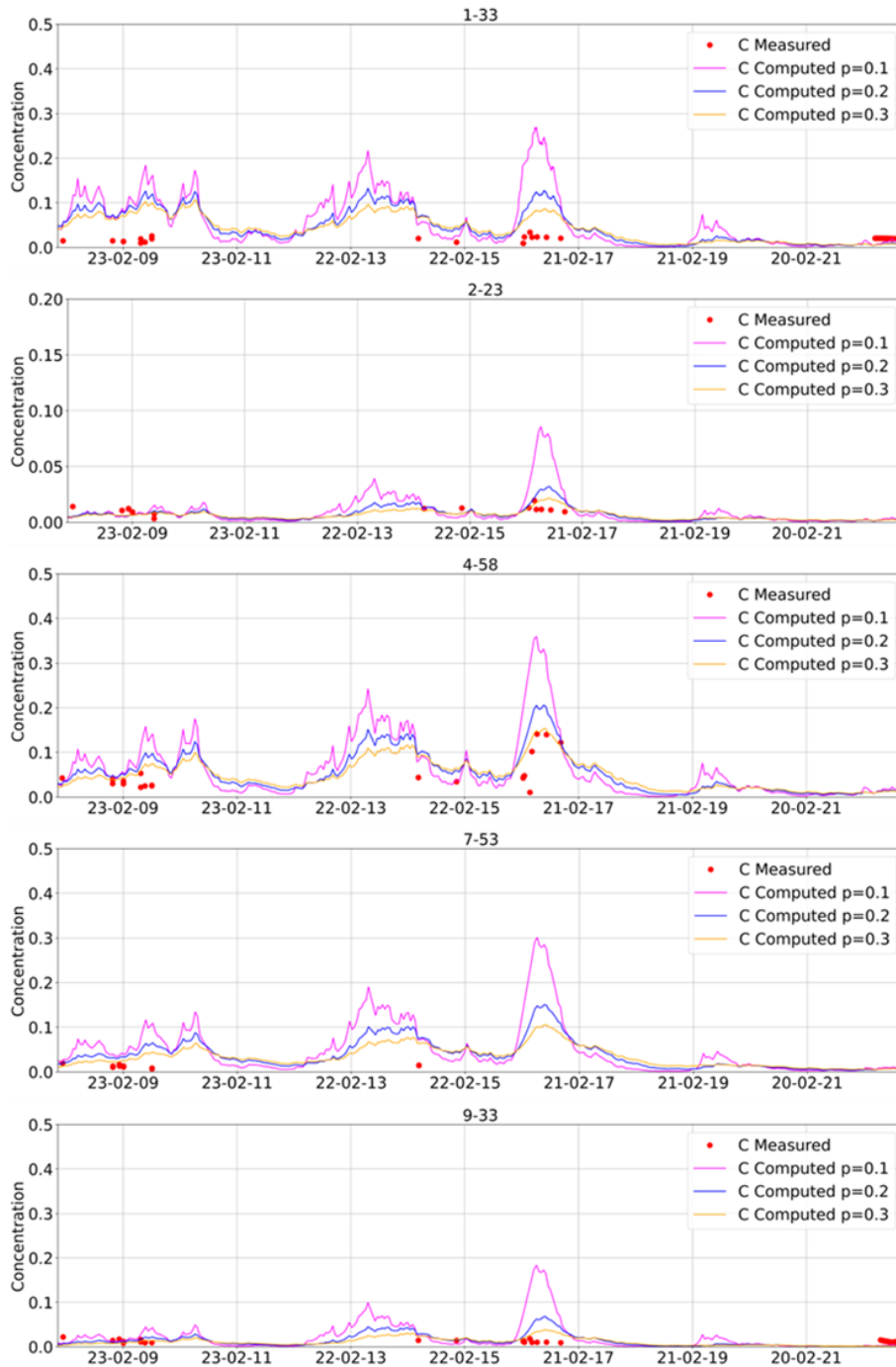


Figure 6-8: Simulated concentration for porosity sensitivity analysis.

The volume of the freshwater lens is strongly affected by the porosity showing a linear relationship. Thus, when porosity is 0.1, the volume is halved compared to the calibrated value (0.2), whereas when it is 0.3, results in a 1.5-fold increase, see Figure 6-9.

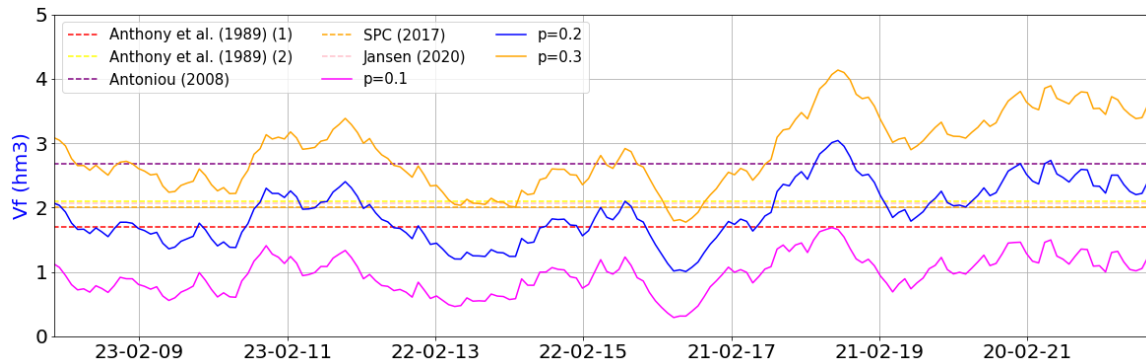


Figure 6-9: Porosity and freshwater lens volume.

6.5 Abstractions

Finally, the effect of pumping was analysed to evaluate its impact on the freshwater lens and the concentration at the pumping wells. This analysis also allows to estimate the maximum sustainable abstraction under natural conditions. Additional simulations were performed multiplying pumping rates at each well by a scaling factor (from 1.2 to 10 times) compared to the ones defined in the calibrated model.

Table 6-1 shows the impact of increased pumping on the freshwater lens volume. As expected, intense pumping leads to a reduction in the freshwater volume. When abstraction rates are multiplied by a factor of 2.5, the freshwater volume is reduced only by 5%. This reduction increases to 13% when abstractions rates are multiplied by a factor of 5, and to 20% when multiplied by a factor of 10. However, for abstraction multiplier by factors lower than 2.5, the maximum freshwater volume only changes 2%.

Table 6-1: Freshwater lens volume and relative change when increasing pumping rates.

Abstraction multiplier factor	Freshwater lens volume (hm ³)	Relative change (%)
1 (calibrated model)	2.41	0 %
1.2	2.40	-0.06 %
1.3	2.38	-0.39 %
1.5	2.36	-1 %
1.75	2.28	-2 %

Abstraction multiplier factor	Freshwater lens volume (hm ³)	Relative change (%)
2.5	2.09	-5 %
5	1.92	-13 %
10	2.40	-20 %

The resulting electrical conductivity for each well for the different abstraction rates is included in Table 6-2. Note that when pumping increases 30% (factor of 1.3), salinity at some wells exceeds drinking water limits, rendering them unsuitable for freshwater extraction. However, significant differences between wells are observed depending on their rates and location. Thus, non-drinking water is obtained when pumping is increased by a factor of 1.5 (increase of 50%) at wells PW1 and PW5, by a factor of 1.75 (increase of 75%) at wells PW2 and PW7, by a factor of 2.5 (increase of 150%) at well PW6, and by a factor of 10 (increase of 900%) at well PW3, because the well PW3 presents the lowest pumping. Therefore, results suggest that water-supply wells are capable of providing drinking water with a pumping increase of 30%. However, the extracted volume per well should not exceed 150 - 200 m³/day (in average) because above this rate (in average) salinity at the wells usually exceeds drinking water limits, see grey color in Table 6-2.

Table 6-2: Pumping rates considered and resulting electrical conductivity for each well. The grey colour indicates when salinity exceeds the drinking water limit.

PW1		PW2		PW3		PW5		PW6		PW7	
Q (m ³ /d)	EC (μS/cm)										
138	1361	95	747	23	72	82	1379	48	589	75	684
165	1939	113	1150	17	102	99	1992	58	840	90	1111
180	2256	123	1375	29	118	107	2311	62	978	98	1350
207	2940	142	1869	34	151	124	2981	72	1281	113	1874
242	3884	165	2561	39	195	144	3881	84	1707	131	2599
345	1091	236	4951	56	344	206	6803	120	3192	188	5071
690	18460	473	14050	113	1025	412	17845	240	9497	375	15556
1381	32734	945	29318	226	2782	823	31499	479	21732	751	29105

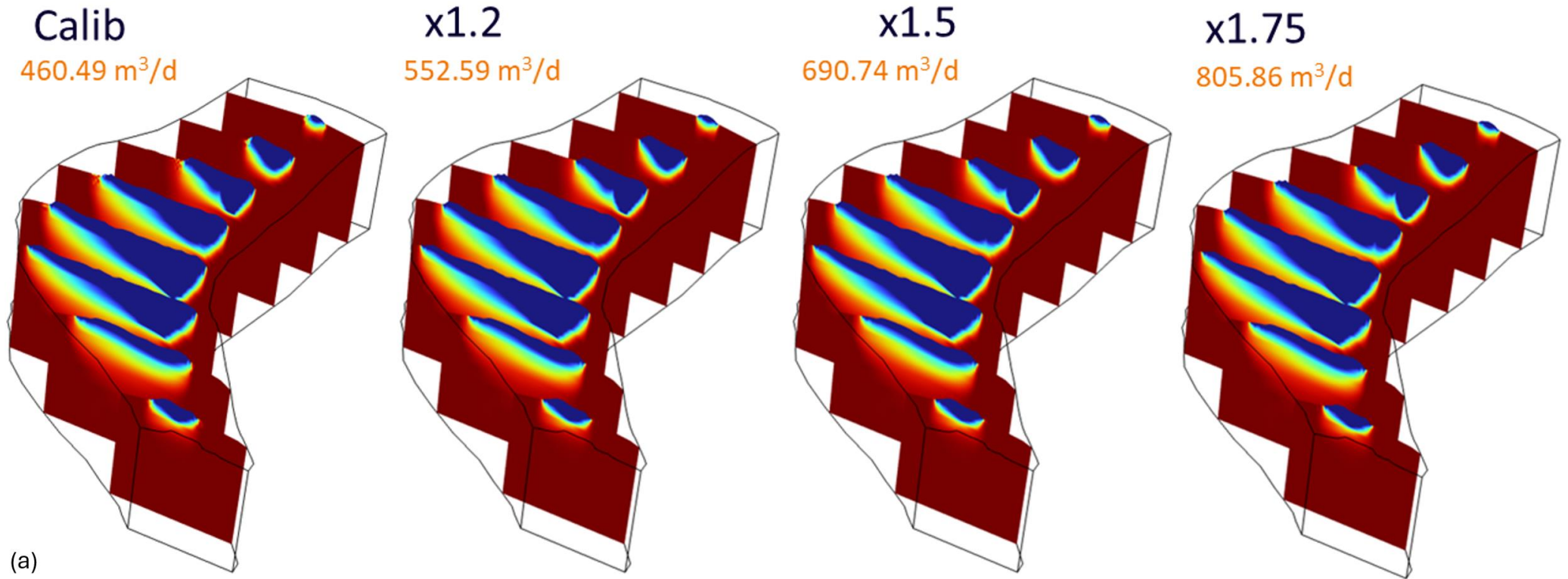


Figure 6-10: Concentration distribution obtained for the Sensitivity analysis of the abstractions considering a multiplier factor of 1.2, 1.5 and 1.75.

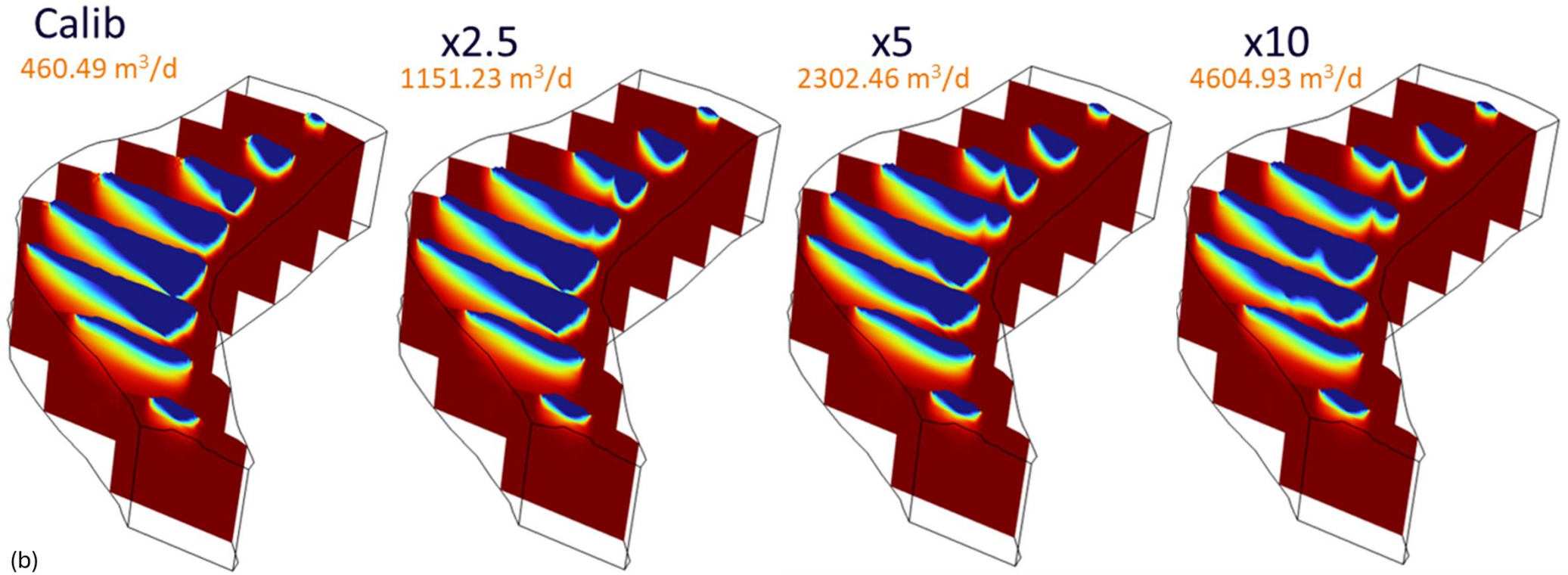


Figure 6-11: Concentration distribution obtained for the Sensitivity analysis of the abstractions considering a multiplier factor of 2.5, 5 and 10.

Figure 6-10 and Figure 6-11 show the concentration distribution when pumping is increased. Note that the impact of pumping is only local, and the freshwater lens thickness only decreases around the pumps. Note also that upconing processes are evident with the upward movement of saltwater to the wells. Thus, when pumping increases, the size and the extent of the upconing cones expand, in particular at the south of the island.

6.6 Summary

The sensitivity analysis has investigated the impact of various parameters on the behaviour of the freshwater lens on Laura Island. The following observations can be made after analysing the results:

- **Hydraulic Conductivity:**
 - **Upper sediment:** The permeability of the Upper Sediments affects the overall thickness and shape of the freshwater lens. Thus, lower conductivities lead to a thicker lens, whereas higher values result in a thinner and more rounded lens.
 - **Lower sediment:** The permeability of the Lower Sediments mainly influences the central part of the lens, causing it to shift slightly upwards or downwards depending on the specific scenario. Thus, an increase in the hydraulic conductivity results in the freshwater lens becoming more rounded and thinner, whereas a decrease causes the lens to increase.
 - **Lower limestone:** The permeability of the Lower Limestones causes minimal overall impact and only affects the saltwater end of the interface. Thus, when the hydraulic conductivity is increased the fresher part of the lens migrates slightly downwards, whereas the saltier part migrates upwards.
- **Seepage Conductance:** The seepage conductance controls the ratio and distribution of freshwater discharge towards the sea. Thus, higher conductance leads to a narrower and more concentrated discharge zone, while lower conductance results in a wider and more diffuse outflow.
- **Dispersion:** The longitudinal and transverse dispersivities control the mixing between freshwater and saltwater. Reduced dispersion narrows the mixing zone, whereas increased dispersion widens the mixing zone and causes the freshwater lens to migrate upward.
- **Porosity:** Porosity directly affects the volume and salinity response of the lens. Higher porosities result in smoother salinity variations in monitoring wells, whereas lower porosities lead to sharper salinity peaks during intrusion events.

- **Abstractions:** Pumping has a local impact on the freshwater lens, causing upconing below the pumping wells while leaving the overall lens volume relatively unaffected. However, as expected, increased pumping rates can lead to salinity increase exceeding drinking water limits in some wells, rendering them unsuitable for freshwater extraction. The level of impact varies significantly between individual wells.

The findings from the sensitivity analysis are summarized in Table 6-3, which the parameters considered and their impact on the freshwater lens dynamics. Overall, the sensitivity analysis provides valuable insights into the key factors governing the dynamics and sustainability of the Laura Island freshwater lens. This information will be integrated, alongside futures scenarios, to develop effective management strategies.

Table 6-3: Summary of sensitivity analysis effect.

Parameter		Effect over the freshwater lens	Freshwater lens Volume		Observation
			Increasing parameter	Decreasing parameter	
Hydraulic conductivity	Upper Sediment	Important	↘	↗	Mainly controlled by Upper and Lower Sediment
	Lower Sediment	Important	↘	↗	
	Lower Limestones	Minimal	≈	≈	
Seepage conductance		Minimal	≈	≈	Effect on the discharge
Dispersion		Important	↘	↗	-
Porosity		Important	↘	↗	Effect over the transient response
Abstractions		Local upconing	≈	≈	Maximum increase 30% to avoid PW salinization

↘ Decrease, ≈ Unchanged, ↗ Increase

7 Limitations of the model

Numerical models of actual systems are usually based on a limited amount of data and, therefore, it is necessary to assume simplifications in the model design and parameterization. While the groundwater model developed for Laura Island provides valuable insights into the behaviour of the freshwater lens system, several limitations exist that must be discussed to understand what type of questions the model can provide accurately and reliably.

The main limitation of the model is the very limited temporal resolution of the abstraction data that made necessary to make assumptions to complete the data series. Salinities at the pumping wells are heavily dependent on the pumping rates. But those are only available for

the years 2007 and 2016. Averaged and interpolated data were used to complete the abstraction functions. As a result, model predictions on salinities at the pumping wells might have a high degree of uncertainty, limiting the model to design optimized groundwater management strategies.

Other limitations include the relatively large scale of the model as well as the uncertainty related to the geometry and parametrization of the Hydrogeological Units. In particular, the geometry of the hydrogeological units largely controls the shape of the freshwater lens. In this model a unique geometry was considered.

Key recommendations to improve model predictions include:

- Data Availability and Quality: The model's accuracy heavily relies on the availability and quality of input data, including groundwater flow dynamics and aquifer characteristics. Conduct comprehensive field surveys and monitoring programs to collect high-quality data on groundwater levels, salinities and pumping rates is essential for the optimization of abstraction schemes during droughts or inundation events.
- Hydrological Processes: The model might oversimplify hydrological processes, such as recharge mechanisms or the connection observed between the ocean-lagoon and the system. Considering the influence of land use and land cover on recharge estimations.
- Geometry of the hydrogeological units. The definition of the geological layers is based on a unique geological cross-section and based on it; the depth of the layers is extrapolated to the whole island extent. Moreover, the connectivity of the units with the sea in the inner part of the lagoon is not well characterized. The geometry largely controls the shape of the freshwater lens. Therefore, further field investigations such as geophysics, construction and description of new boreholes and long-term pumping tests are required to characterize in detail (i) the unconfined behaviour of system and (ii) vertical variations of the hydraulic properties of the system. Studies to characterize the geometry and parametrization of the Hydrogeological Units would be required to increase the precision of the model and decrease prediction uncertainty
- Model Calibration and Validation: Numerical results indicate that the freshwater lens is mainly controlled by the recharge and the geometry and parametrization of the Hydrogeological Units, whereas heads variations are mainly controlled by sea level fluctuations. Moreover, salinities at the pumping wells are strongly controlled by the abstractions that are only available for the years 2007 and 2016. The uncertainties associated with parameter estimation and simplifications adopted with pumping rates may affect the model performance. Therefore, detailed records of abstractions, together with continuous monitoring of groundwater levels and salinity.

8 Simulation of predictive scenarios

Once the model is calibrated and the sensitivity analysis is performed, various simulations have been conducted to predict the freshwater lens behaviour under different future scenarios. These scenarios focus on three key aspects: First, the impact of extended drought periods is analysed, exploring not only the reduction of the freshwater lens volume but also the time required for restoring the freshwater lens. Second, simulations of sea level rise are carried out to anticipate and plan for the consequences of this phenomenon. Finally, simulations of rapid inundation due to storm surge events provide crucial information about the vulnerability of the freshwater lens to this type of event and its subsequent recovery.

A series of 16 simulations, summarised in Table 8-1, have been conducted. They are a combination of future recharge variations and drought events (scenarios A, B and C), changes in sea level elevation (scenario D), and a possible inundation event (scenario E). For the climatic scenarios (A to C) two different simulations have been performed by considering (i) the same abstraction as the one defined in the daily transient model (A1, B1 and C1) and (ii) and increase in the abstractions of 30% (A2, B2, C2). In Table 8-1 the scenarios are described in base to the modifications performed with respect to the calibrated model. The rest of aspects that are not modified (boundary conditions, parameters, abstractions) remain unchanged and are those described for the daily transient model, Chapter 4.5.

The initial time for the future scenarios is November 2022, which corresponds to the last model results of the calibrated daily model, and the simulation time covers the period of almost 16 years until September 2038. A reference future scenario has been carried out as base case without any modification with respect to the calibrated daily transient model. That case serves as control for results comparison.

Table 8-1: Summary of future scenarios with the main variations included in each simulation.

Scenario	Change with respect to the reference	Name	Variant
A: Drought with Dry Recovery	Recharge function with Dec. 2008 – Nov. 2010 data replaced by data from the reference drought	A1	Abstractions of the calibrated model
		A2	Increase in Abstractions of 30%
B: Drought with Average Recovery	Recharge function with Dec. 2014 – Nov. 2016 data replaced by data from the reference drought	B1	Abstractions of the calibrated model
		B2	Increase in Abstractions of 30%
C: Extreme Double Drought	Recharge function with Dec. 2016 – Nov. 2020 data replaced by data from the reference drought (repeated)	C1	Abstractions of the calibrated model
		C2	Increase in Abstractions of 30%
D: Sea level rise (SLR)	Increase sea-level	D1	A2
		D2	A2 + 25 cm
		D3	A2 + 50 cm

Scenario	Change with respect to the reference	Name	Variant
		D4	A2 + 100 cm
E: Inundation	Inundation event with a return period of 25 years combined with SLR	E1	E1.1 - SLR +0.25 m - Wet condition
			E1.2 - SLR +0.25 m - Dry condition
		E2	E2.1 - SLR +0.5 m - Wet condition
			E2.2- SLR +0.5 m - Dry condition
		E3	E3.1- SLR +1.0 m - Wet condition
			E3.2 - SLR +1.0 m - Dry condition

The temporal evolution of the freshwater lens and the salinities computed at the pumping wells have been evaluated and compared to the reference future scenario. In addition to that, and in order to gain a quantitative understanding of the impact of the freshwater lens to climate, storm surge and sea level rise events, different measurable diagnostics have been evaluated for each scenario:

- Minimum freshwater lens volume reached during or post-event.
- Time required for freshwater lens volume to reach 1.5 hm³ once the extreme event simulated (drought and inundation) finishes.
- Time required for the freshwater volume to recover 80% from the end of the event to the one obtained for the reference simulation.
- Pumping wells above the drinking water threshold by the end of the event.
- Time required for pumping wells to drop below the drinking water threshold.

8.1 Drought recovery

8.1.1 Scenarios description

8.1.1.1 Drought event

Droughts pose significant challenges for managing freshwater lens, especially in the context of climate change where they may become more frequent and severe. Atolls, with limited freshwater alternatives, rely heavily on groundwater especially during droughts that place greater pressure and threatens the freshwater lens (Werner et al., 2017). Moreover, the shape and thickness of the freshwater lens is mainly controlled by rainfall.

The response of the Laura Island freshwater lens to droughts conditions is analysed using three simulated recharge scenarios. After reviewing the historical monthly rainfall data from Laura dating back to 1955, the period from December 1982 to November 1984 is selected as the reference drought period. This period encompasses the driest 12-month period (Dec. 1982 – Nov. 1983) along with the only drought occurring during the wet-season (Mar. – Jun. 1984). Thus, the following three drought scenarios are defined by creating three recharge series in which the data from the reference drought period replaces a portion of the 2007-2022 recharge series used for the model calibration.

- **Dry recovery (scenario A):** Simulates a drought followed by low rainfall years by integrating the reference drought between December 2008 and November 2010.
- **Average recovery (scenario B):** Simulates a drought followed by average rainfall years. The reference drought is placed between December 2014 and November 2016.
- **Double drought (scenario C):** Simulates an extended drought by doubling the extent of the reference drought and replacing the data of the 2016-2020 period.

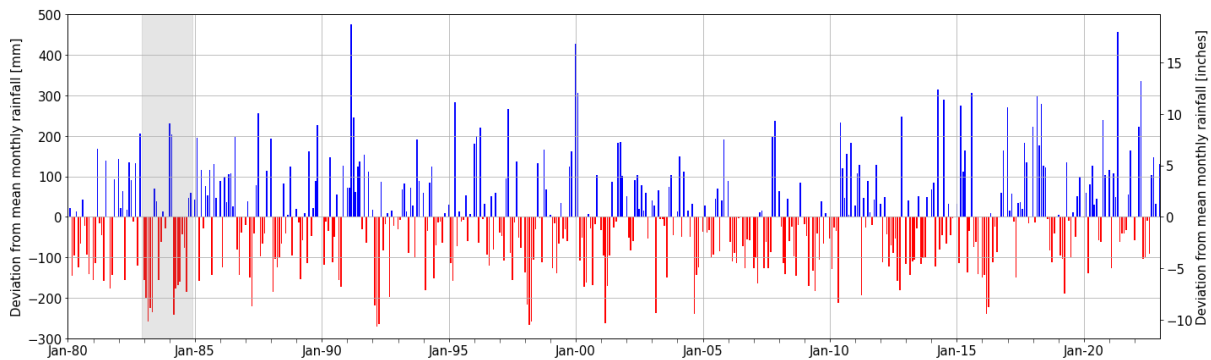


Figure 8-1: Deviation from monthly rainfall historic data from 1980 to 2022. Months above the monthly average rainfall are indicated in blue, while those below average are in red. Grey shaded part indicates the reference drought from Dec-1982 to Nov 1984.

Figure 8-2 presents the modified recharge series for each drought scenarios. All other boundary conditions remain unchanged. Each scenario starts with the calibrated model's state in November 2022 and projects the response of the lens for a total of almost 16 years until September 2038. From these scenarios, the idea is to assess the impact quantitatively and qualitatively on water availability, simulate the progress of seawater intrusion in response to reduced recharge, analyse the resilience of the system after the event, and to evaluate potential water management strategies to mitigate the future drought's impacts. Results are presented regarding scenarios effect on both the total volume of the freshwater lens and on pumping wells. Additionally, a reference case is simulated without any modifications to the recharge, serving as our control for results comparison.

Figure 8-2 presents the modified recharge series for the three drought scenarios. Thus, in scenario A the average annual recharge decreased 45% with respect to the one in the base case (from an average recharge of 2480 mm/y to 1324 mm/y for the two-years period), in scenario B the average annual recharge decreased 35% (from an average recharge of 2041 to 1330 mm/y for the two-years period), and in scenario C the average annual recharge decreased 58% (from an average recharge of 2944 to 1245 mm/y for the four-years period).

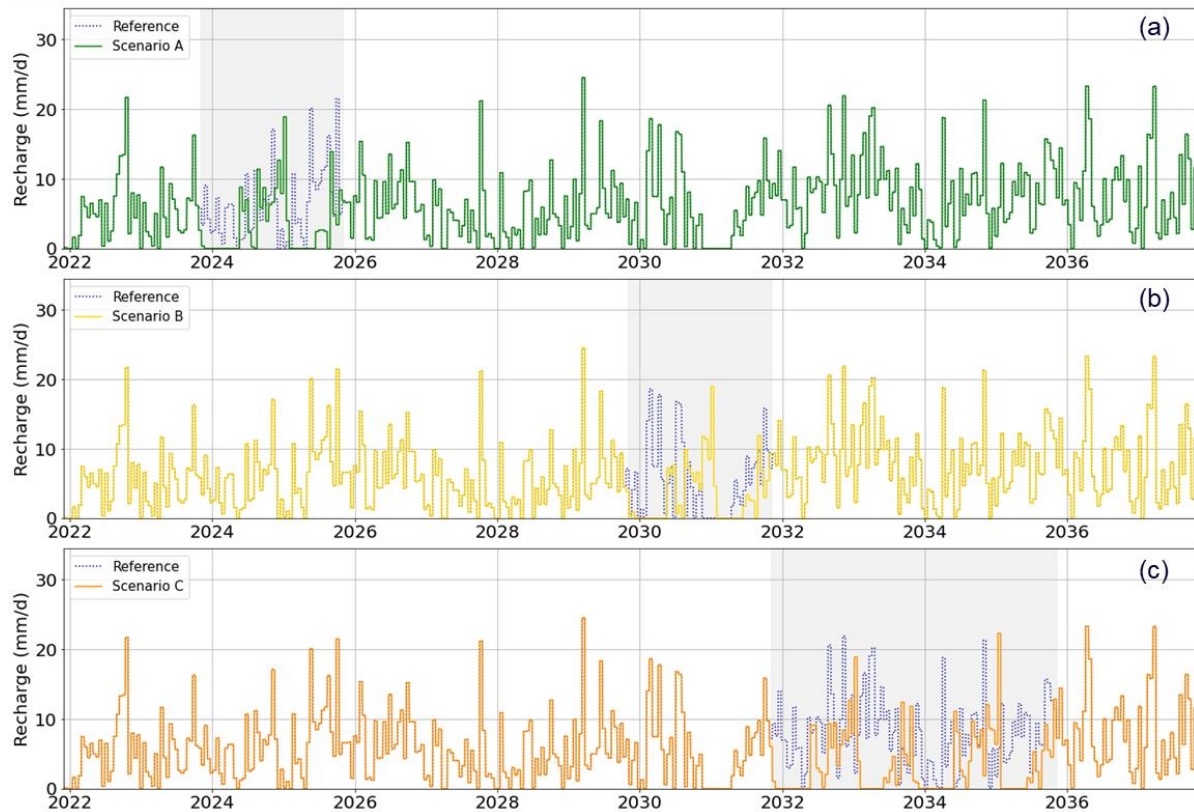


Figure 8-2: Drought scenarios recharge series. (a) Scenario A: Dry recovery; (b) Scenario B: Average recovery; (c) Scenario C: Double drought. Dotted blue represents the reference case, with no modification in the recharge.

The objective of these scenarios is to quantitatively and qualitatively assess the impact on water availability, simulate the progress of seawater intrusion in response to reduced recharge, analyse the resilience of the system after the event, and evaluate potential water management strategies to mitigate the future drought’s impacts. Results are presented regarding the effect on both the total volume of the freshwater lens and on the water salinity evolution in the pumping wells. The results are compared against the reference scenario without any modifications in the recharge.

8.1.1.2 Drought event with abstraction increase

A second set of scenarios investigates the combined impact of drought and increased pumping on the Laura Island freshwater lens. Specifically, the pumping rate defined in the calibrated daily model is raised by 30% in all wells simulating a future higher demand for groundwater. This set of scenarios share the same recharge scenarios as the ones defined previously: dry recovery, average recovery, and double drought. This set of scenarios aims to understand how the lens responds to intensified stress due to increased pumping to satisfy the demand of freshwater during drought periods.

8.1.2 Effect on the freshwater lens volume and recovery

8.1.2.1 Drought event

Figure 8-3 illustrates the simulated droughts' impact on the freshwater lens volume. For each scenario the top graph shows the evolution of the recharge defined and the bottom graph the computed freshwater lens volume from 2022 to 2038. For all scenarios, a reduction in freshwater lens volume is observed with respect to the reference simulation (dashed blue line in the graphs). This reduction is 58% for A1, reaching a minimum of 0.84 hm³ and 46% for B1, with a minimum volume of 0.85 hm³. This reduction is more pronounced in the scenario C1 (76 %), with a minimum volume of 0.48 hm³ in the third year of drought.

The recovery rate differs depending on the scenario. Thus, in scenario B1, higher post-drought rainfall, 2913 mm net recharge in the year following the drought, facilitates a faster recovery, reaching 80% of the reference simulation volume (approximately 1.8 hm³) in just 6 months after the end of the drought. Over this 6-month period, the freshwater lens volume increases from 1.05 to 1.92 hm³, indicating a recovery rate of 0.15 hm³/month. Scenario A1 requires 12 months to recover 80% of the reference simulation (around 2.4 hm³), increasing from 1.02 to 1.92 hm³ at a recovery rate of 0.04 hm³/month, with an annual recharge of 2678 mm during the year following the drought. Conversely, the C1 scenario, takes 15 months for 80% recovery (around 2.2 hm³), with the volume passing from 1.0 to 1.76 hm³, corresponding to a recovery rate of 0.05 hm³/month, with 3023 mm of net recharge in the year following the C1 drought. The recovery rates of A1 and C1 scenarios are very similar. However, while the C1 scenario, demonstrates a rapid initial response, it achieves only a partial recovery, with 90% of the volume in the reference simulation restored by the end of the simulation.

Figure 8-4 illustrates the monthly freshwater lens volume recovery for each scenario with the corresponding monthly recharge for each scenario. The recharge for each scenario varies after each dry event, as droughts occur at different times. In Scenario A1, the freshwater lens volume increases for the first four months about 0.2 hm³. Then, there is period of low recharge

with only 43 mm in the fifth month, leading to a reduction in the freshwater lens volume. Finally, recharge and, consequently, the freshwater lens volume increase linearly the rest of the year. In scenario B1, recharge increases until the fifth month, resulting in a continuous freshwater lens volume growth of 0.2 hm³. However, a decrease in recharge in the sixth month, with only 63 mm, causes a slight reduction. From the seventh month onward, the freshwater lens volume increases along with recharge for the rest of the year after the event. In Scenario C1, the initial freshwater lens volume is quasi stable, until the fourth and sixth months, where it experiences a significantly increase, rising from 1.2 hm³ in the fourth month to 1.7 hm³ in the sixth month. Between the seventh and ninth month, recharge diminishes, causing the volume to plateau, before rising again in the tenth, eleventh, and twelfth months. Although the precipitation is more significant during the year after the event in scenario C1, its variability throughout the year hinders its recovery. By the end of the year, B1 simulation exhibits the most significant volume and A1 the lowest.

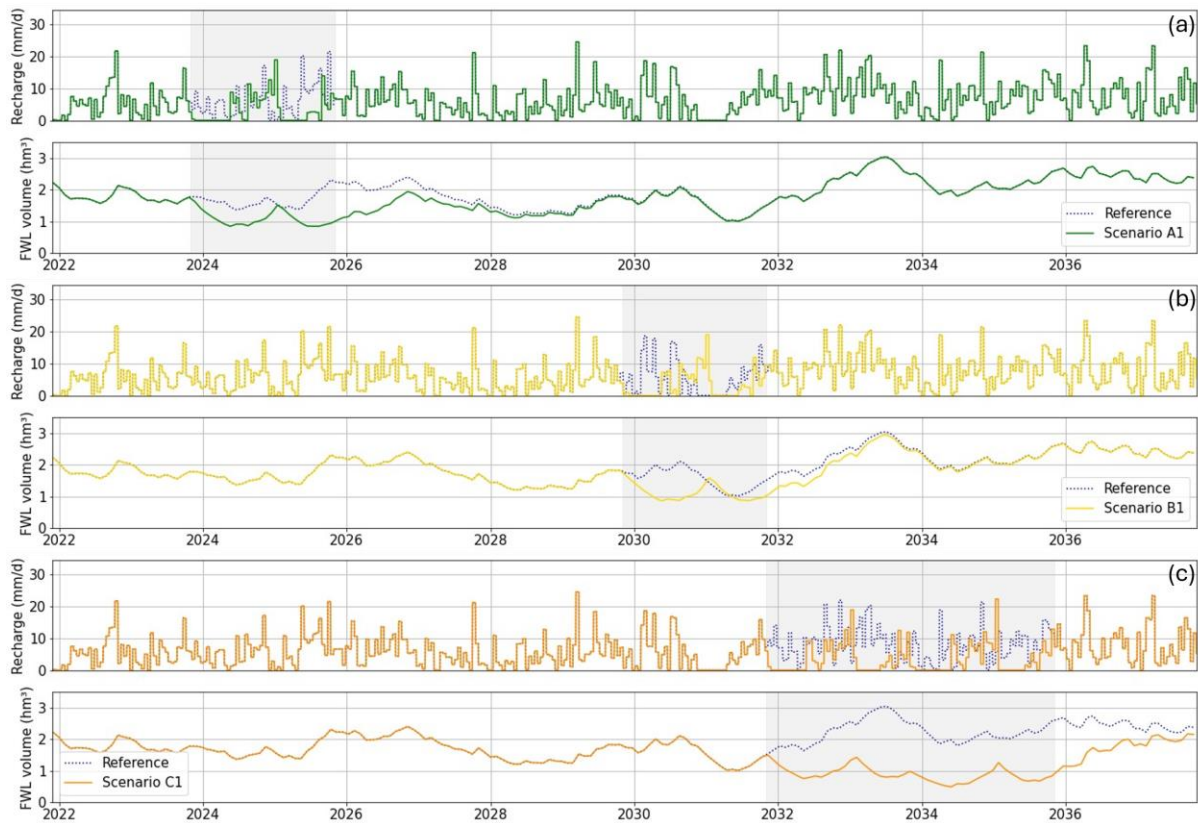


Figure 8-3: Freshwater lens volume in response to drought scenarios. (a) Scenario A1: Dry recovery; (b) B1: Average recovery; (c) C1: Double drought.

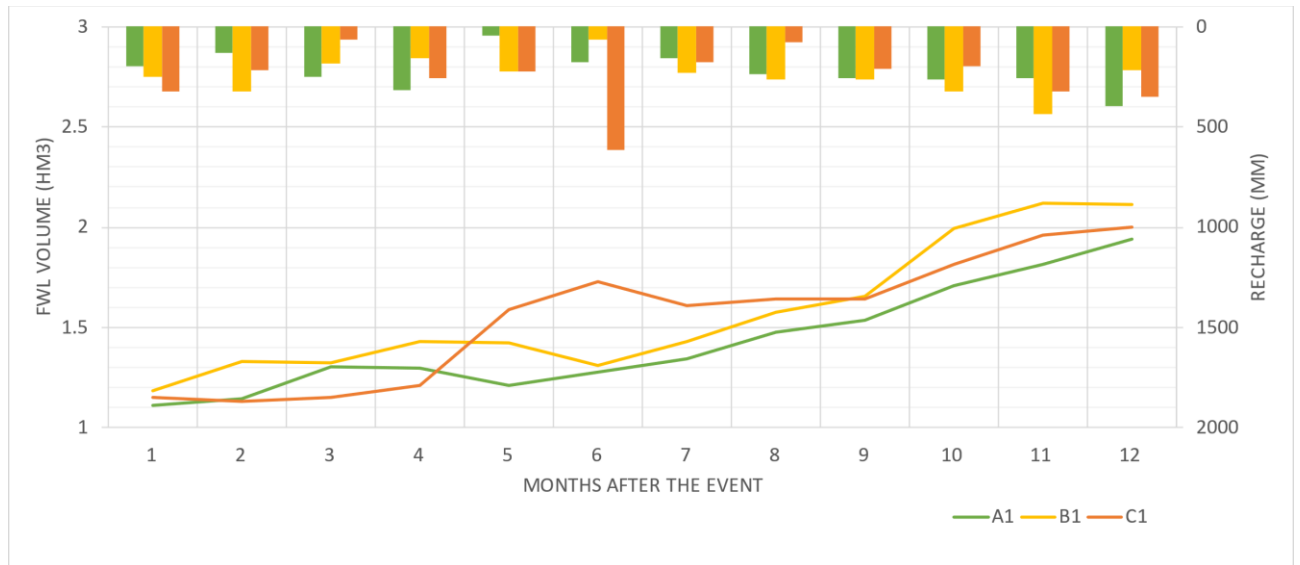


Figure 8-4: Freshwater lens volume recovery and recharge.

8.1.2.2 Drought event with abstraction increase

In scenarios A2, B2 and C3, which consider the same recharge as the ones for scenarios A1, B1 and C1 but including an increase of 30% in abstractions, the reduction in the freshwater lens volume is negligible (less than 3%). Therefore, the results of the temporal variation of the freshwater lens from the scenarios considering the initial and increased pumping nearly overlap, Figure 8-5. This is because the increase in pumping only impacts locally the concentration distribution around the wells, as observed in the sensitivity analysis (Section 6.5), and then the freshwater lens volume remains practically unaltered. Consequently, post-drought lens recovery follows exactly the evolution computed for the scenarios with no increase in pumping rates.

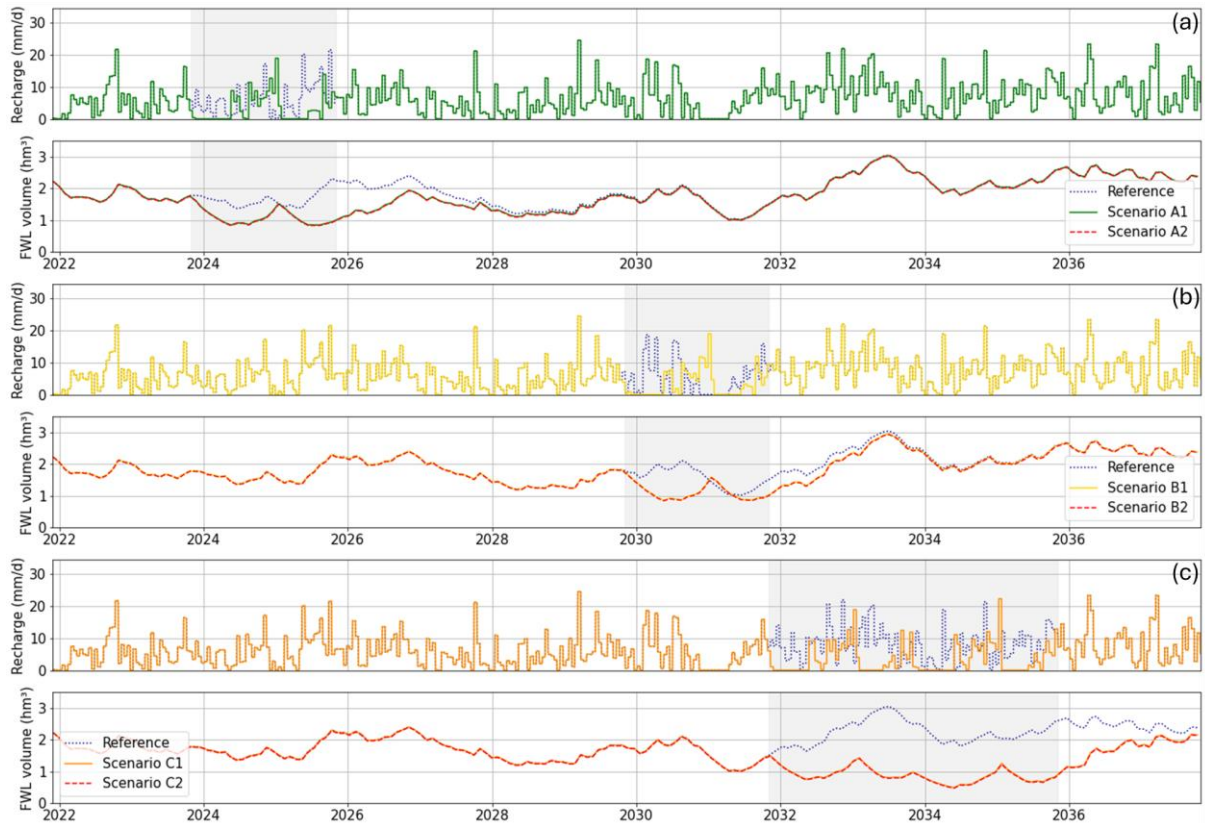


Figure 8-5: Freshwater lens volume in response to drought scenarios with abstraction increased. (a) Scenario A: Dry recovery; (b) Scenario B: Average recovery; (c) Scenario C: Double drought. Increased abstraction scenarios are represented by red dashed lines.

Therefore, numerical results suggest that the freshwater lens recovers to nearly pre-drought events within approximately one year, even after a double drought event.

8.1.3 Effect and recovery on pumping wells

In this section, the evolution of the concentration of the water in the pumping wells is analysed for the climate scenarios.

8.1.3.1 Drought event

Figure 8-6 illustrates the salinities at the pumping wells for scenario A1. Note that two pumping wells (PW1 and PW7) already exceeding the freshwater limit (salinity higher than 2500 $\mu\text{S}/\text{cm}$) before the drought occurs. During the drought, their salinity further increases reaching peak values of 6809 and 8284 $\mu\text{S}/\text{cm}$, respectively. Approximately 8 months after the drought, their salinity drops again below the potability threshold. The salinity in PW2 fluctuates around the 2500 $\mu\text{S}/\text{cm}$ threshold, exceeding it three times during the drought. The maximum salinity

increase reached is 3736 $\mu\text{S}/\text{cm}$ and occurs approximately 5 months before the end of the drought. Finally, the wells PW3, PW5, and PW6 with low pumping rates during the drought (PW3 around 50 m^3/d , and PW5 and PW6 below 10 m^3/d) show small impact on their salinity during the drought remaining within the safe limits.

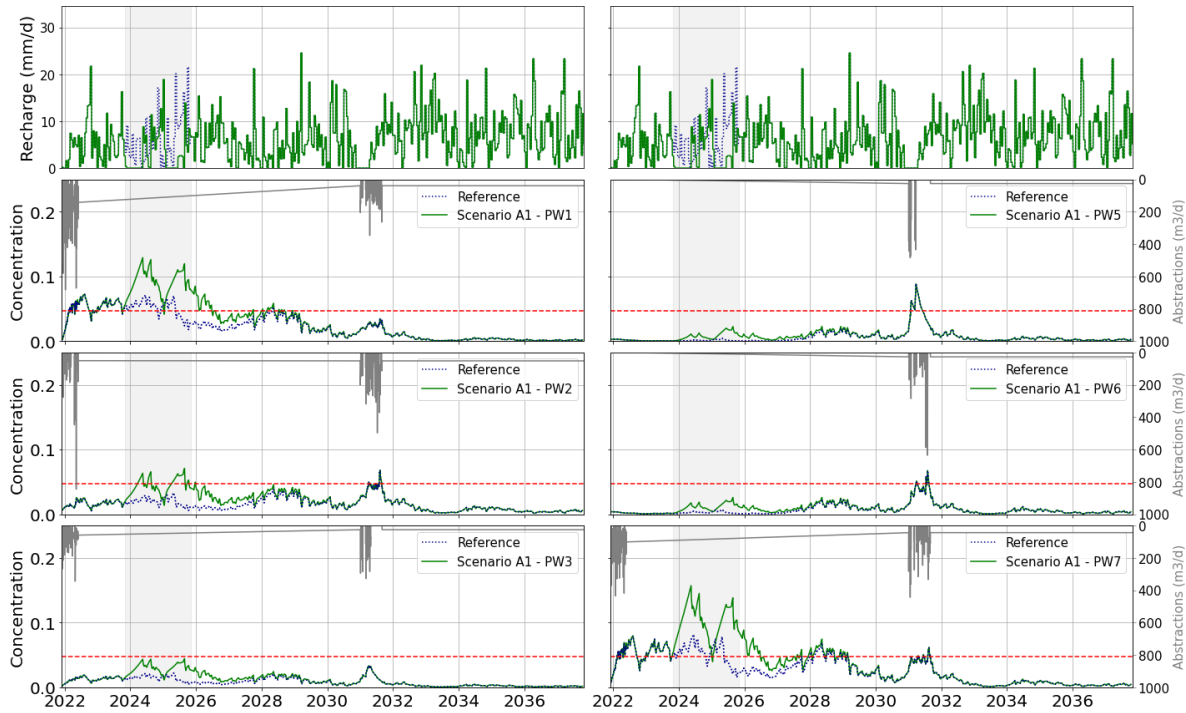


Figure 8-6: Pumping wells response to Scenario A1: Dry recovery. The grey lines on the secondary y-axis represent abstraction and the red dashed line the 2500 $\mu\text{S}/\text{cm}$ limit.

It is important to note that although some water-supply wells are capable of providing drinking water during the drought, when abstraction is intense (year 2031) most of the pumping wells except PW1 and PW3 show salinities above the drinking water limit. Therefore, the salinity at the pumping wells is significantly controlled by the abstraction strategy.

In the drought scenario with average recovery (scenario B1), all pumping wells exceeded the 2500 $\mu\text{S}/\text{cm}$ limit temporarily during the drought period, see Figure 8-7. However, note that the temporal distribution of pumping differs along the drought period. Thus, during the first half of the drought period, pumping rates are continuous with values resulting from data interpolation (interpolation considered in the calibrated daily model between 2007 and 2016), and pumping wells do not or only slightly exceed the drinking water limit. However, the second half of the drought period is simulated using the daily abstraction data (corresponding to the year 2017 in the daily transient model) in which alternating periods of several days with intense pumping are followed by days with no pumping. During the intense pumping periods, salinity in the

pumping wells increase more rapidly. However, during the no-pumping periods a rapid recovery in salinity levels is observed, even in the reference simulation without drought (dashed lines in Figure 7-6). At the end of the drought, there is a prolonged period with no pumping activity that promotes the recovery of the pumping wells. Recovery times ranging from 18 days at PW1, 32 days at PW2, 35 days at PW6, 77 days at PW7 and 86 at PW5 are obtained. However, all pumping wells are all fully recovered by the end of the drought event. The results of this scenario suggest that a continuous extraction of water might help to maintain the water salinity at the pumping wells below the 2500 $\mu\text{S}/\text{cm}$ threshold, whereas intense and intermittent pumping strategies lead to a fast salinization of the wells that will decay after a pumping pause. The first option is, therefore, a better strategy to deal with pumping during drought periods.

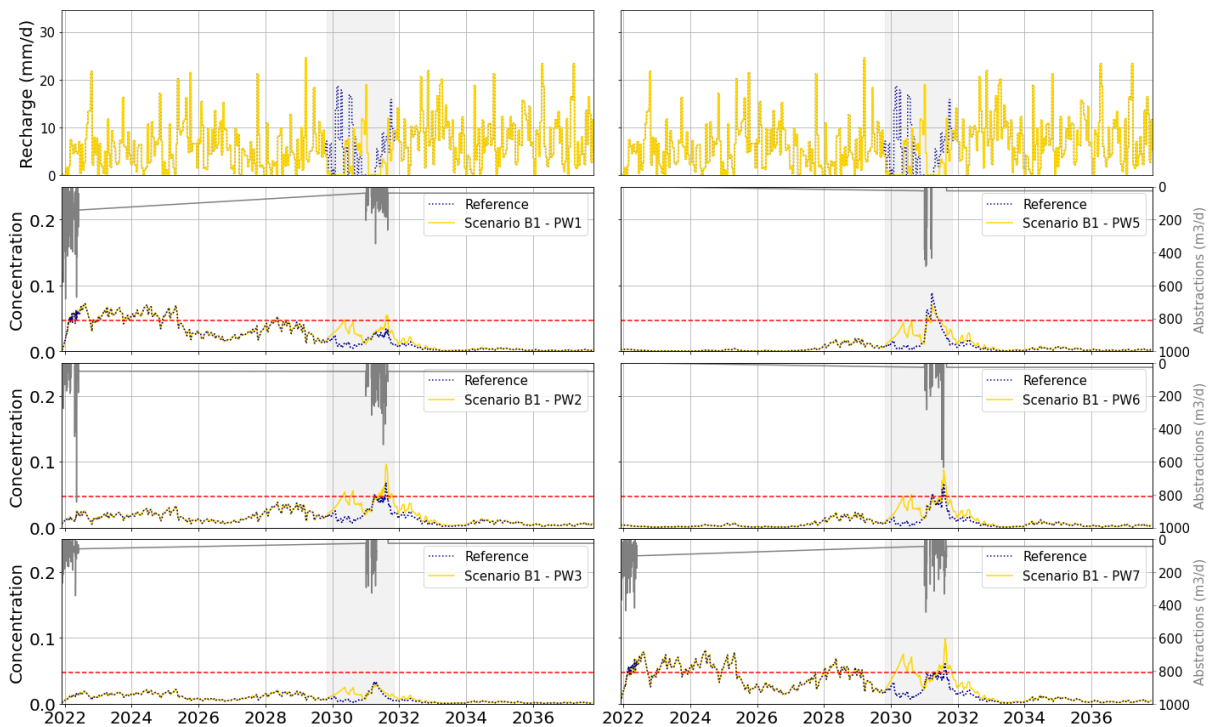


Figure 8-7: Pumping wells response to Scenario B1: Average recovery. The grey lines on the secondary y-axis represent abstraction and the red dashed line the 2500 $\mu\text{S}/\text{cm}$ limit.

The double drought scenario (C1) extends over a 4-year period. During this prolonged drought, all pumping wells except PW3 exceed the drinking water limit, see Figure 8-8. Four significant peaks in salinity levels are observed for all the wells, with the third peak being the most pronounced, in response to zero recharge periods during the drought. Initially, each well starts with salinity below the potability limit. At the onset of the drought, PW2 exhibits a salinity level 50% below the potability limit, while PW6 and PW1 are at 35% and PW5 at 26%. PW2 and PW7 experience the most rapid salinization, exceeding the limit within 3 months, followed by

PW5 and PW6 within 4 months, and PW1 taking the longest (6 months) to exceed the limit. By the end of the event, all wells are fully recovered, returning to acceptable salinity levels.

The result of this scenario illustrates how resilient the system is to pumping, since salinity recovers as soon as the drought period is over. Therefore, a sound strategy is to pump as much as possible during the drought because the system will quickly recover. The only constraint is to maintain the salinity below the 2500 $\mu\text{S}/\text{cm}$ limit, which can be accomplished by maintaining a constant pumping rate.

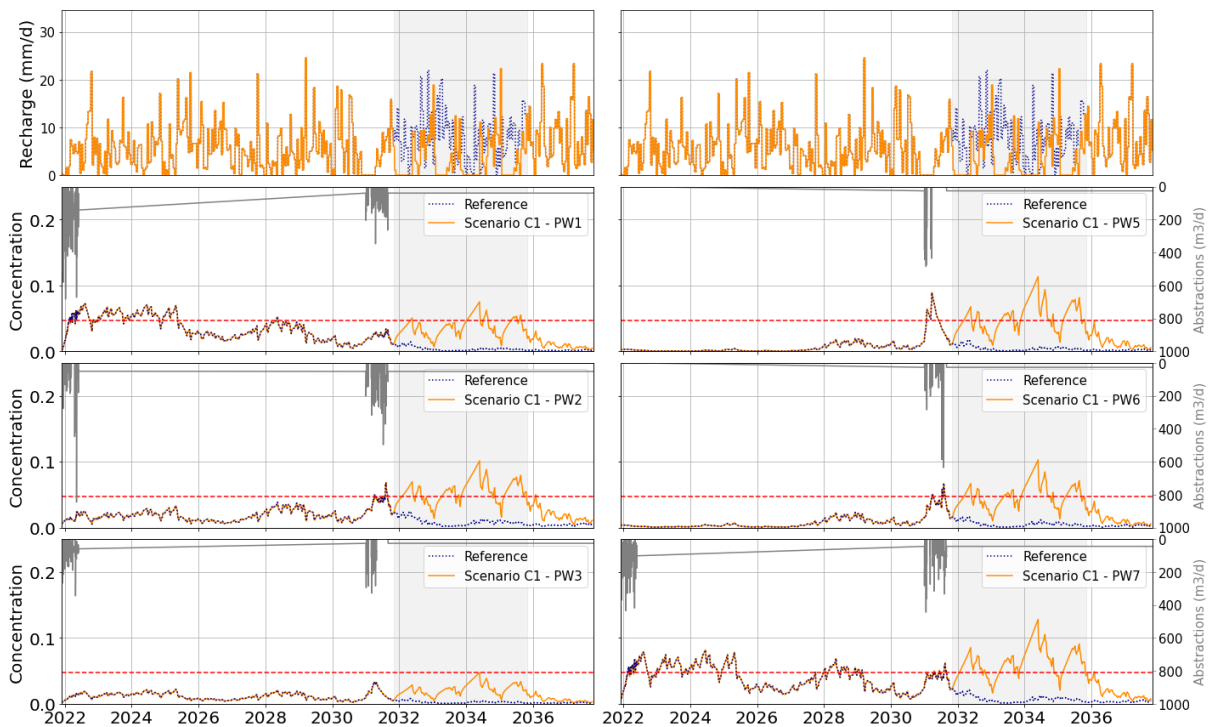


Figure 8-8: Pumping wells response to Scenario C1: Double drought. The grey lines on the secondary y-axis represent abstraction and the red dashed line the 2500 $\mu\text{S}/\text{cm}$ limit.

8.1.3.2 Drought event with abstraction increase

When pumping is increased by 30%, an average salinity increase of 50% is observed at all the pumping wells but following similar trends to the ones for the scenarios without increased pumping. Among the three scenarios (A2, B2 and C2), the main difference is the magnitude of the salinity increase.

For the dry recovery scenario (scenario A2), the wells PW1, PW2, PW7 and PW3 exceed the drinking water limit during the drought, and only the well PW3 is below the limit at the end of the event, see Figure 8-9. After the drought, the well PW2 recovers in around 3 months

whereas the well PW3 is fully recovered and the wells PW1 and PW7 take took 11 months to return to acceptable salinity levels.

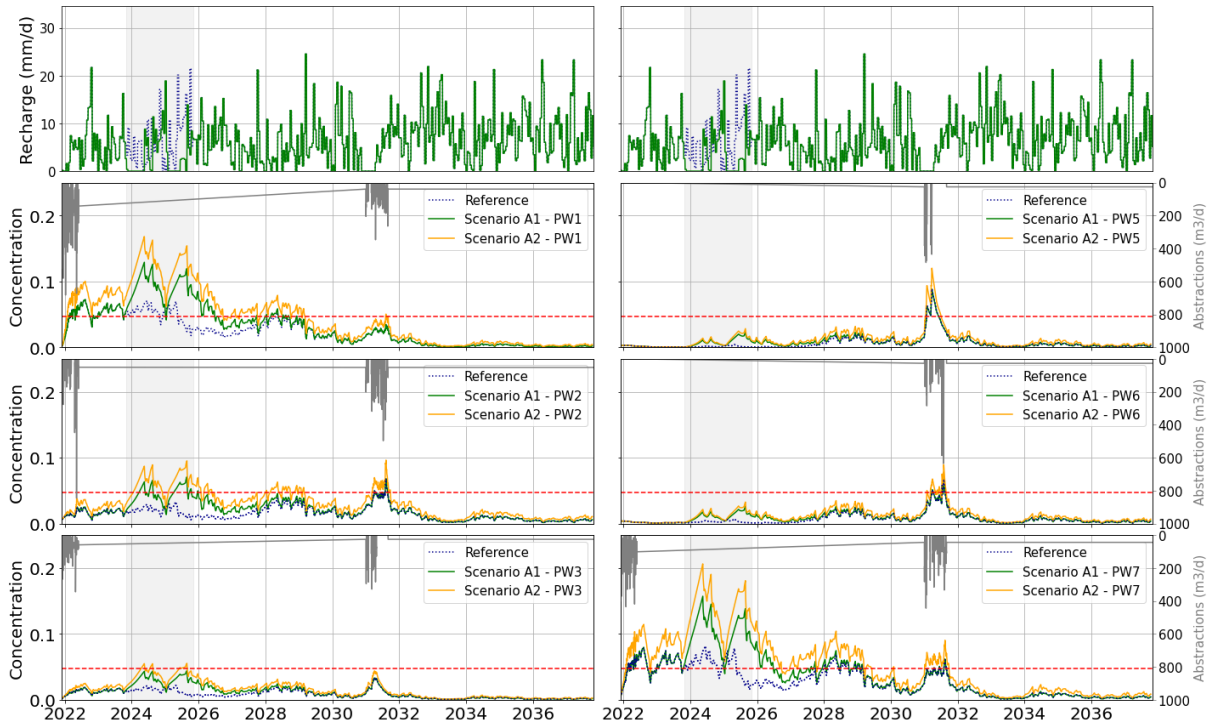


Figure 8-9: Pumping wells response to Scenario A2: Dry recovery. The grey lines on the secondary y-axis represent abstraction and the red dashed line the 2500 µS/cm limit.

In scenario B2, the effect on pumping wells is less pronounced during the drought, with a salinity increase of 30% across all wells, see Figure 7-9. A rapid recovery is observed before the end of the event induced by a decrease in pumping. Thus, at the end of the drought only the wells PW2 and PW7, exceed the drinking water limit but recover within one month.

In the double drought scenario (C2), the salinities show a similar trend to the one for scenario C1, with a salinity increase of approximately 40% for all the wells, see Figure 8-11. At the end of the event the wells PW2 and PW7 are still salinized, but they recover in 5 months to pre-drought values within about five months.

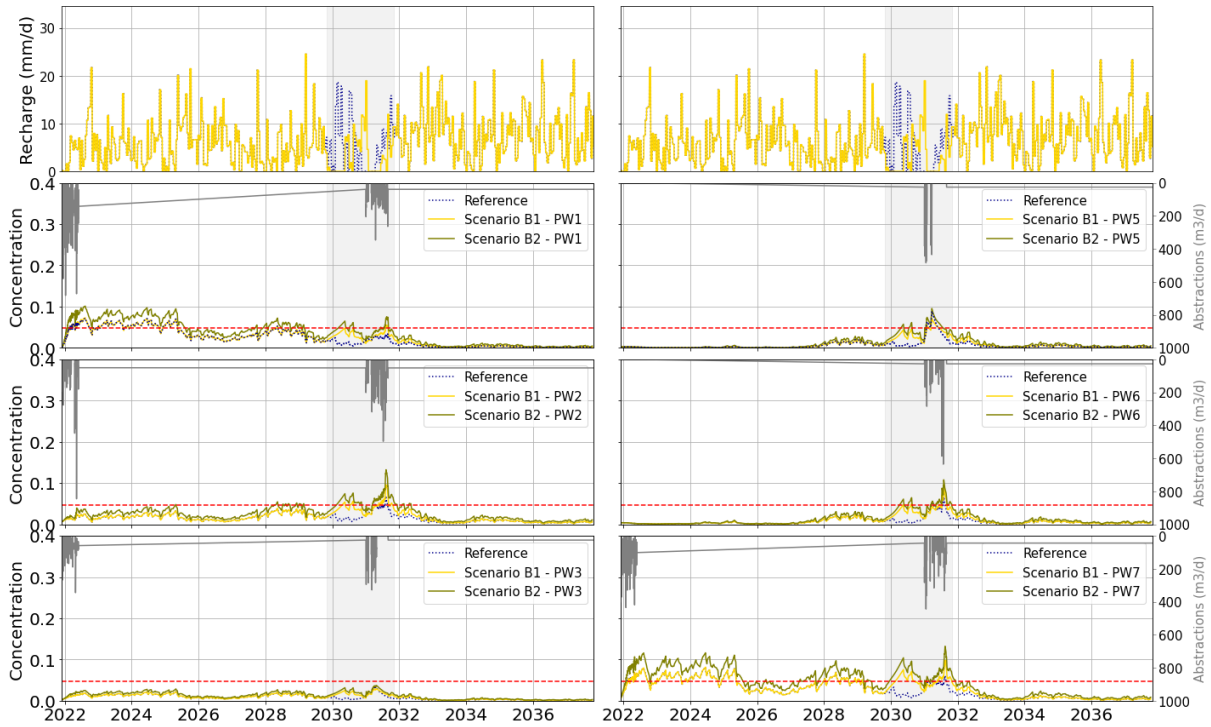


Figure 8-10: Pumping wells response to Scenario B2: Average recovery. The grey lines on the secondary y-axis represent abstraction and the red dashed line the 2500 µS/cm limit.

In summary, various recharge scenarios and abstraction rates have been simulated and the responses of the freshwater lens and pumping wells were described.

In the face of drought events, the freshwater lens is highly sensitive, experiencing notable reductions in volume (up to 50% of decrease), particularly in scenarios with prolonged or intensified droughts. Although the lens shows a relatively rapid recovery following droughts, the extent and duration of recovery vary significantly depending on the severity of the drought and subsequent recharge conditions.

Moreover, the combined effects of drought and increased pumping highlight the importance of understanding groundwater abstraction impacts on the lens. Despite a localized increase in salinity around pumping wells, the overall impact on freshwater lens volume is insignificant, indicating the resilience of the lens in mitigating stresses induced by increased pumping.

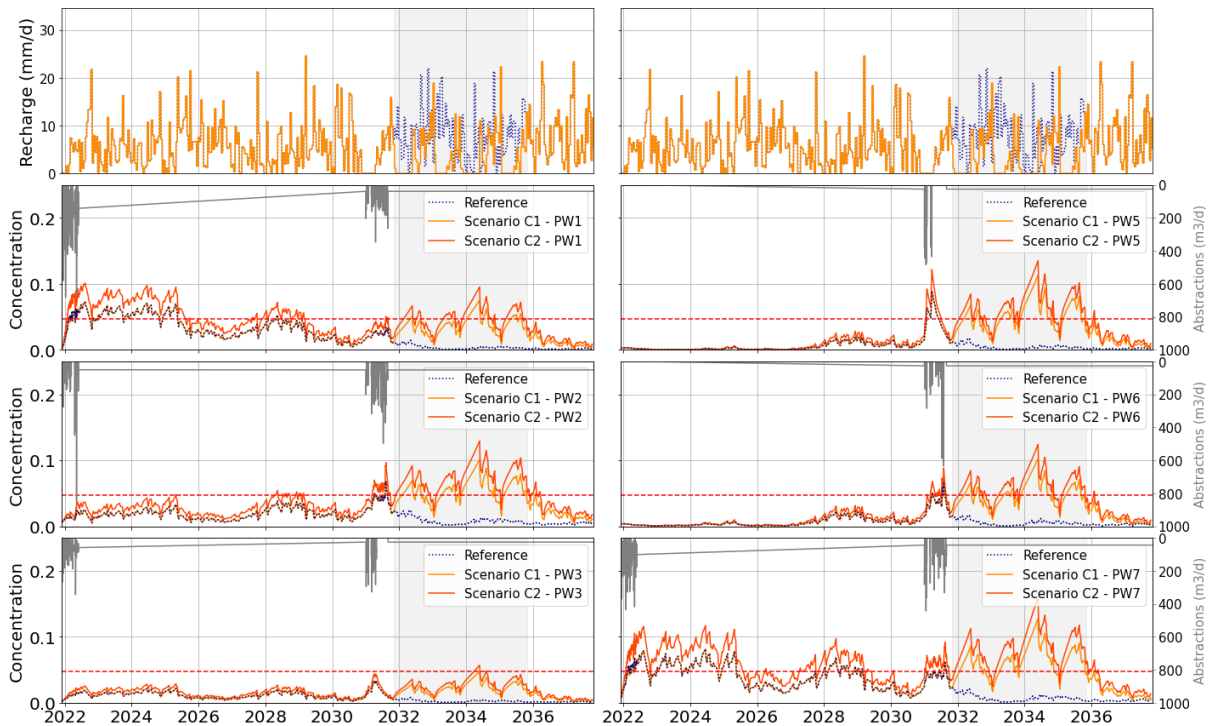


Figure 8-11: Pumping wells response to Scenario C2: Double drought. The grey lines on the secondary y-axis represent abstraction and the red dashed line the 2500 µS/cm limit.

8.2 Sea-level rise (SLR)

8.2.1 Scenario description

The second set of scenarios explores the potential effects of sea level rise combined with increased pumping of 30% and a drought and a dry recovery on the groundwater resources (scenario A2 with sea level rise, see details on the recharge function in Section 8.1.1.1 and in Figure 8-2a).

Each scenario simulates a linear increase in sea level between November 2022 and September 2038. These scenarios are based on projected sea level increases up to 2050, but for the purpose of this simulation, only projections up to 2039 (are considered, see Figure 8-12a). The details for each scenario are explained in the following:

- Baseline (D1): No change in sea level is considered.
- Low rise (D2): a 0.25 m of increase is considered, corresponding to an annual rise of 0.93 cm/year.

- Medium rise (D3): a 0.50 m of increase is considered, corresponding to an annual rise of 1.85 cm/year.
- High rise (D4): a 1.00 m of increase is considered, corresponding to an annual rise of 3.70 cm/year.

8.2.2 Impact of SLR

Figure 8-12(bottom) shows the volume of the freshwater lens over the 16-years projection period for the four SLR scenarios. Note that most of the lines overlap. Thus, the volume remains unaffected in all cases except for scenario D4 (High rise) in which a decrease of less than 5% in the freshwater volume is observed in the last 2 years of simulation.

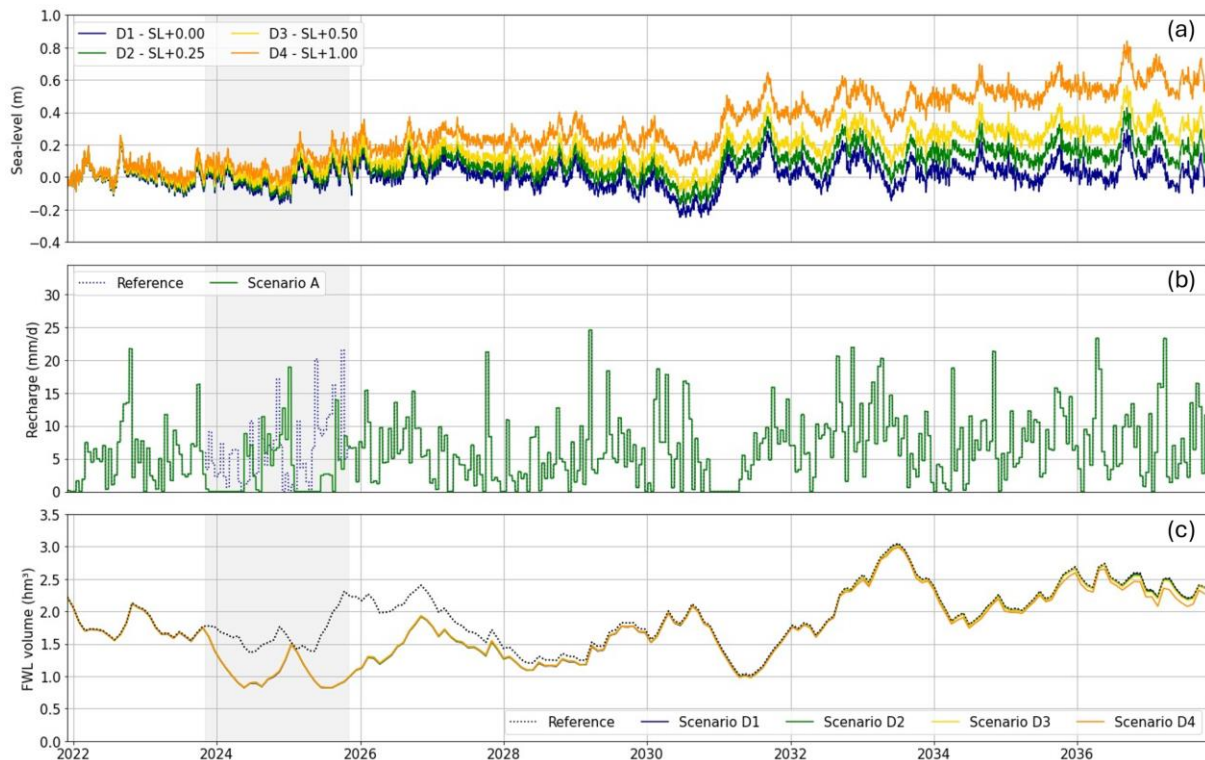


Figure 8-12: Freshwater lens volume in response to drought scenarios. (a) Sea-level used for SLR scenarios. (b) Recharge used for SLR scenarios (c) Freshwater lens volume for the four SLR scenarios and the referenced case (dashed blue line) for comparison.

The rise in the sea level primarily induces an increase in the piezometric level that is observed in all the scenarios. Thus, the piezometric level exceeds the topography in internal areas of Laura Island, particularly in the topographic depression (Figure 8-13). Even the scenario D1 (with no sea level increase) exhibits areas where the water table exceeds the topography.

These areas are prone to water ponding during high tides because the sea level data from 2007 to 2022 already show a slight increase in sea level on the order of 0.31 cm/yr.

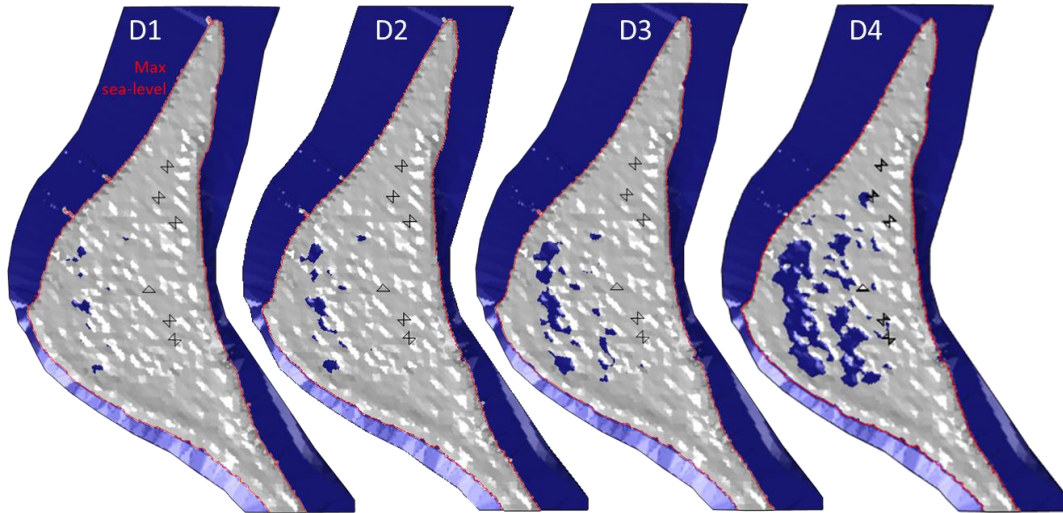


Figure 8-13: Water ponding areas with the water table above topography.

Figure 8-14 shows a vertical cross section with the thickness of the freshwater lens and the piezometric level. Note that the increase in sea level mainly impacts on the laterals of the lens and negligible effects are observed in the middle of the island. As expected, the highest impact on the freshwater lens is obtained in scenario D4 (High rise), in particular on the ocean side with a migration of the freshwater lens of about 200 m at the middle of the island. This result is positive, as all pumping wells are situated further from the coastline and nearer to the lagoon side.

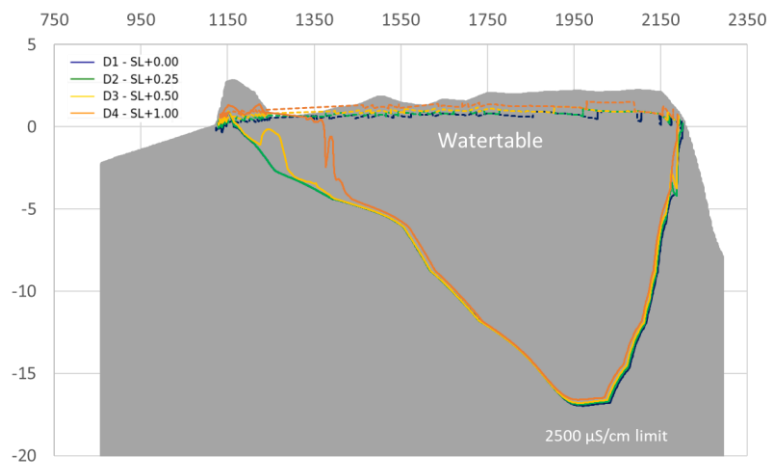


Figure 8-14: Vertical profile in the central part of Laura Island.

Figure 8-15 illustrates the salinities at the wells for the sea level rise scenarios. A negligible impact of the sea level rise is observed on the salinities, with results overlapping for all the wells. Therefore, the pumping wells remain unaffected regardless of the magnitude of the sea level rise. These results are due to two different factors: (i) large distance of the wells from the coastline and (ii) minimal impact observed on the lagoon side.

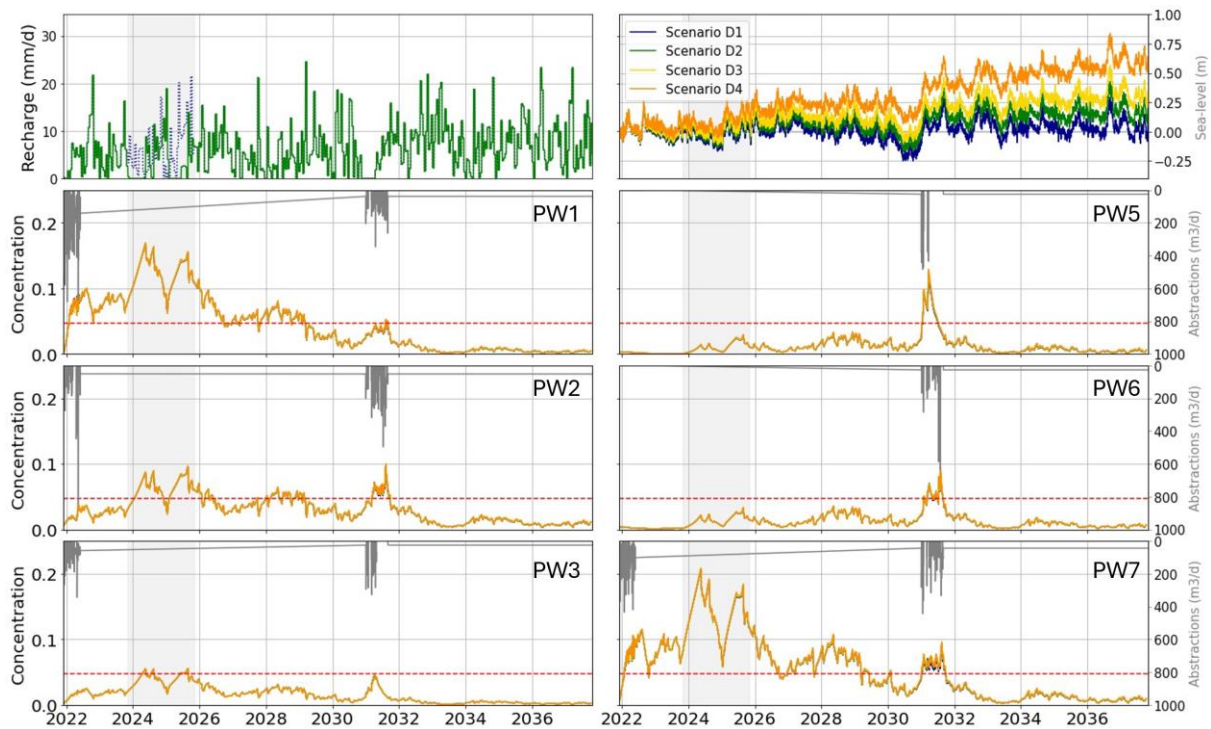


Figure 8-15: Pumping wells response to SLR scenarios. The grey lines on the secondary y-axis represent abstraction and the red dashed line the 2500 $\mu\text{S}/\text{cm}$ limit.

In summary, the analysis of the sea-level rise scenarios over a 16-years projection results in no significant change or relatively minor changes on the freshwater lens. Thus, the volume of the freshwater lens remains largely unaffected, with only a small decrease observed in the most extreme scenario (D4) during the last 2 years of prediction.

The rise in sea level primarily results in an increase in the piezometric level, exceeding the topography in internal areas of Laura Island. Additionally, while sea level rise only impacts the laterals of the freshwater lens particularly on the ocean side. Therefore, a negligible impact is observed on the pumping wells salinities.

In essence, sea level rise within the projected range and without important inland flooding, poses minimal risk to the overall volume and accessibility of the Laura Island freshwater lens.

8.3 Inundation events

8.3.1 Scenario description

This last set of scenarios explores potential inundation by seawater caused by a storm surge. Three scenarios are simulated (E1, E2, E3), each one corresponding to a specific inundation event with a return period of 25 years combined with three potential sea levels, 0.25, 0.5, and 1 m, respectively. Figure 8-16 illustrates the flood extent for the three scenarios with their associated water column height, ranging from 0.01 to 3.81 m.

Table 8-2 summarizes the inundated area, percentage of inundated island, and estimated ponded water volume for each scenario. The latter represents the maximum amount of water that could potentially infiltrate, and it is calculated as the integral of the water column (inundation height minus topographic elevation).

A 2-day inundation event is considered after which the recovery is simulated for a total duration of 5 years. During inundation, rainfall recharge is applied only to non-inundated areas. A Cauchy boundary condition simulates the inundation process at the inundated areas, so that the flow is $Q = \alpha ((z + I_h) - h)$, where z denotes elevation, I_h represents the inundation height, h the computed hydraulic head, and α represents a conductance term. The term α was calibrated using scenario E1 so that after a 2-day inundation event, all the floodwater volume is infiltrated, resulting in $\alpha = 1.68\text{e-}6 \text{ m}^2/\text{s}$. The concentration of infiltrated water during the inundation is assumed to be equal to the one for seawater (c_s).

After the inundation event, the recharge with freshwater promotes the freshwater lens recovery. Two post-event recharge scenarios are considered: a wet variant, in which above-average rainfall conditions follow the inundation event (scenarios E1.1, 2.1 and E3.1), and a dry variant, in which below-average rainfall conditions come after inundation (scenarios E1.2, 2.2 and E3.2), see Figure 8-17.

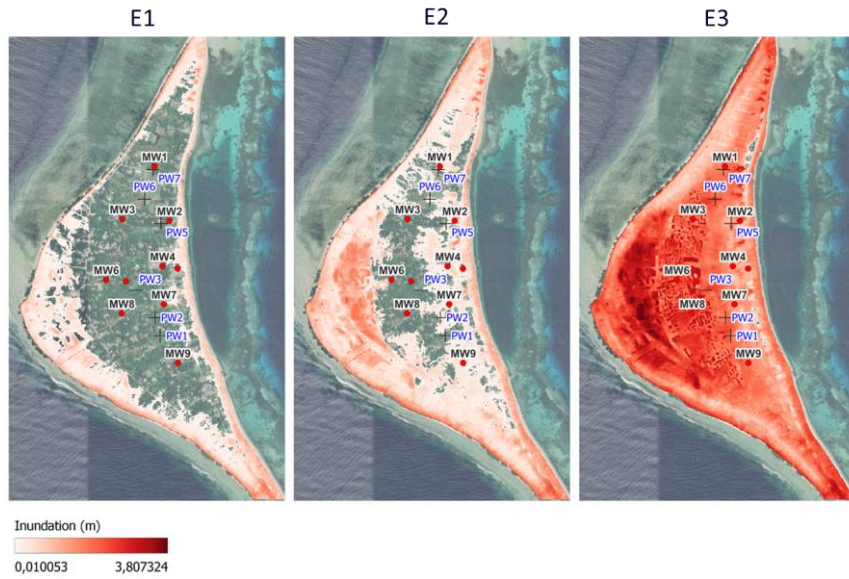


Figure 8-16: Map of inundation height.

Table 8-2: Inundation scenarios.

		E1	E2	E3
Inundated area (m ²)		990220	1894717	2337593
Percentage inundated island (%)		40	77	95
Floodwater volume (hm ³)		0.36	1.03	4.36
Infiltrated volume (hm ³)	Wet condition	0.34	0.59	1.17
	Dry condition	0.31	0.53	0.97

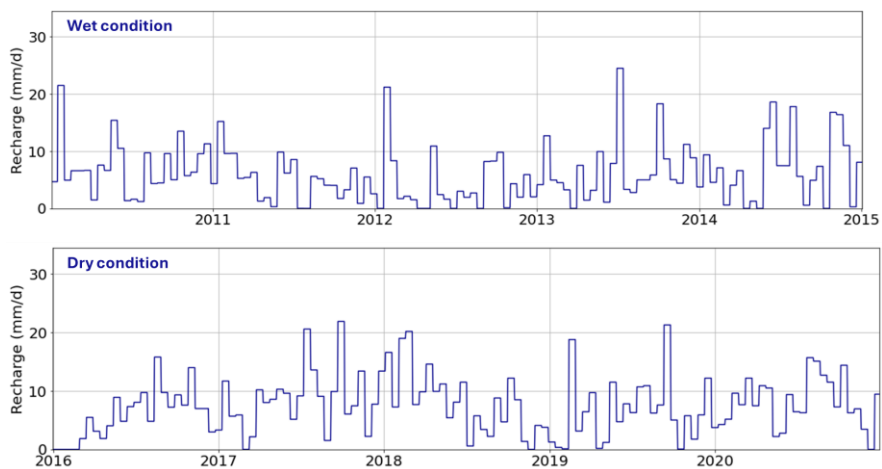


Figure 8-17: Recharge during inundations scenarios.

8.3.2 Effect on the freshwater lens volume and recovery

Figure 8-18 presents the freshwater lens volume in response to the inundation scenarios occurring during wet conditions. It is evident that the volume of the lens is impacted in all three scenarios (E1.1, E2.1, E3.1). Specifically, immediately after the 2-day inundation period, the volume decreases from 2.1 hm³ to 1.5 hm³, 0.3 hm³ and 5.10⁻³ hm³, for the scenarios E1.1, E2.1 and E3.1, respectively.

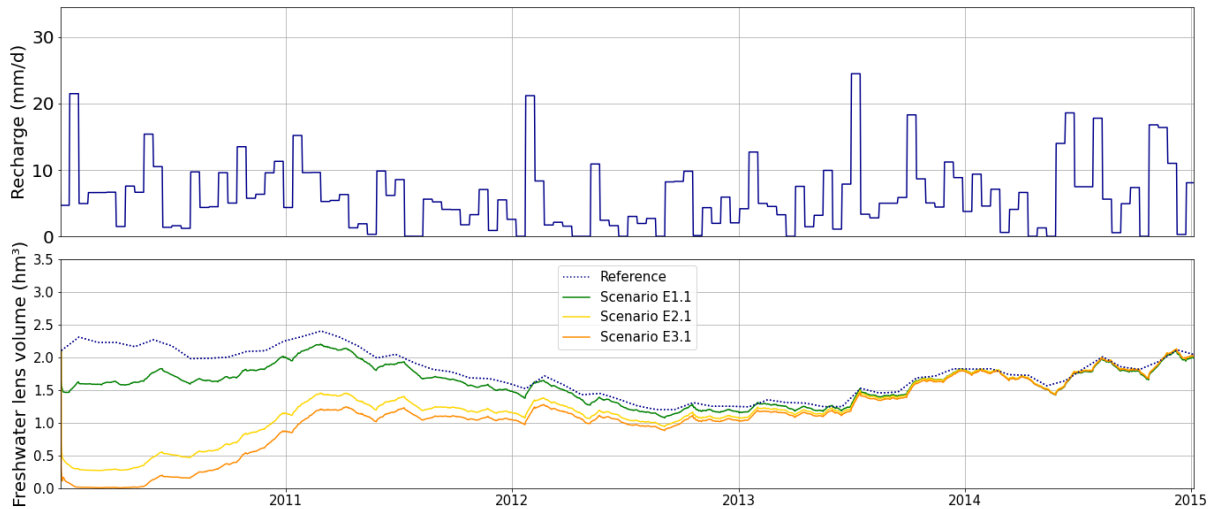


Figure 8-18: Freshwater lens volume in response to inundation scenarios in wet conditions. (a) Recharge used for scenarios (b) Freshwater lens volume.

Scenario E1.1, with a very limited inundation extent, presents the lowest impact on the freshwater lens volume compared to scenarios E2.1 and E3.1. The volume decreases around 30% in scenario E1.1 but always remains above levels observed during low rainfall periods. In contrast, the inundation in scenarios E2.1 and E3.1 covers a large portion of the island (Figure 7-15) and significantly impacts the freshwater volume. Thus, after inundation in the scenario E3.1 less than 0.015 hm³ of freshwater remains within the lens for over a 3-month period. The reduction in the freshwater lens volume is greater than the volume of infiltrated water (Table 8-2). For every cubic meter of water that infiltrates, the resulting freshwater lens volume loss is twice that amount. This substantial loss of freshwater can be attributed to mixing processes occurring within the lens. During inundation events, seawater infiltrates into the freshwater lens. The seawater then mixes with the existing freshwater, increasing its salinity. As a result, not only does the volume decrease due to the infiltrated seawater, but also because of the spreading of the mixed solution. This spreading effectively doubles the volume loss compared to the seawater infiltrated alone. However, the recovery of the freshwater lens volume is rapid for all scenarios. Within 7 months, inundation E1.1 has recovered 80% of the reference simulation volume, while E2.1 and E3.1 take 28 and 32 months, respectively. The time to

recover a volume of 1 hm³, corresponding to the lowest volume reached by the lens during periods of low rainfall is 9 months for E2.1 and 13 months for E3.1.

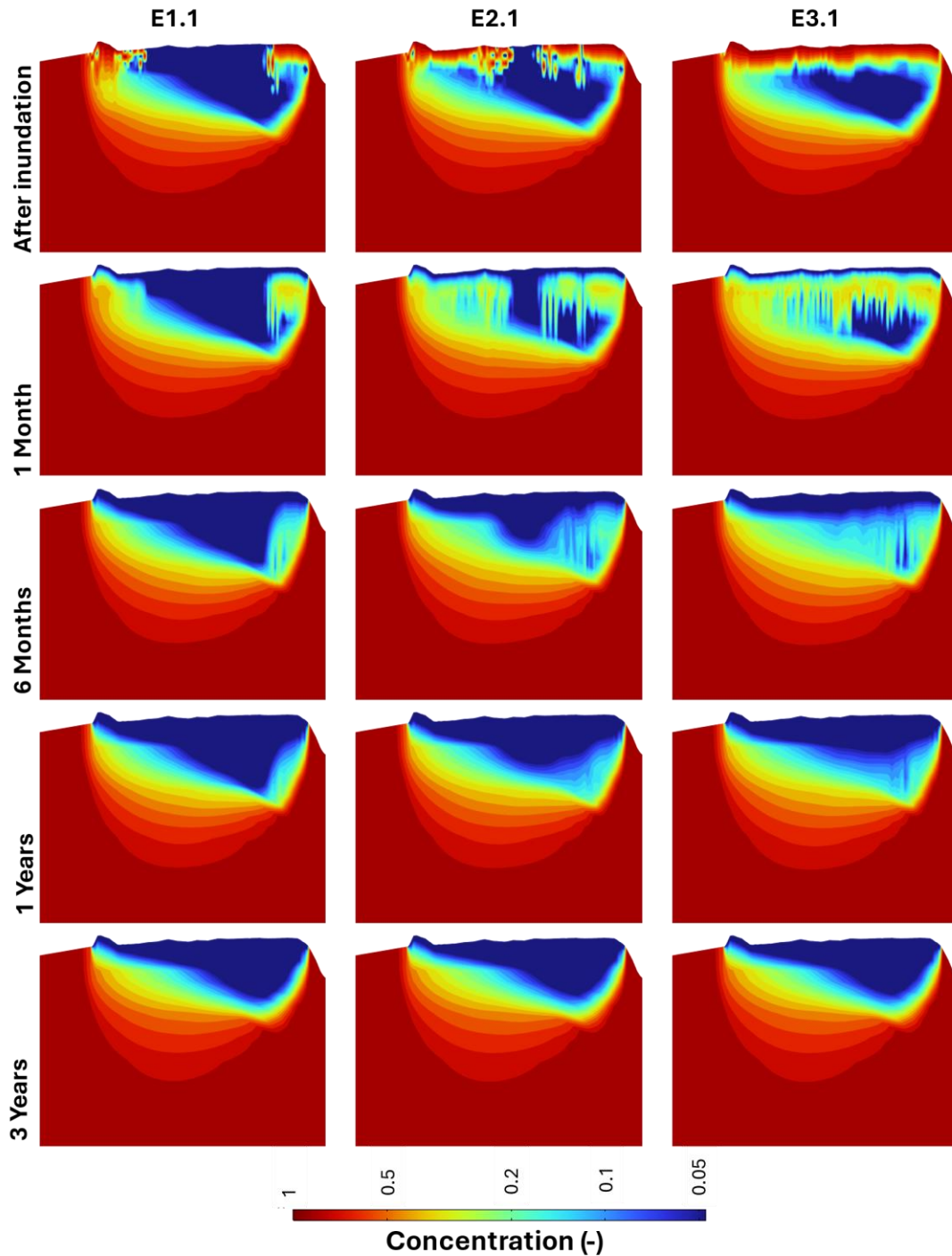


Figure 8-19: Vertical salinity profile in the central part of Laura Island at different times after the storm surge in wet conditions.

Figure 8-19 illustrates the temporal evolution of salinity distribution along a vertical cross section from the West side to the East side at the centre of Laura Island immediately after the 2 days inundation, and 1 month, 6 months, 1 year, and 3 years after. In all scenarios, a downwards migration of the salt plume pushed down by freshwater recharge is observed. Afterwards, progressive dilution and washing finally lead to the full recovery of the initial freshwater lens. While the inundation in scenarios E1.1 and E2.1 primarily affects the lateral boundaries of the lens, with the inner part relatively unaffected, the inundation in scenario E3.1 impacts the entire freshwater lens. However, a superficial freshwater lens is already formed after 6 months. Note that in the three scenarios several sinking denser fingers are formed specially in the first month after the inundation.

Figure 8-20 presents the freshwater lens volume in response to the inundation scenarios occurring during dry conditions (scenarios E1.2, E2.2 and E3.2). The freshwater lens volume significantly responds to inundations scenarios. Thus, the lens volume decreases from an initial value of 1.28 hm³ to 0.81 hm³, 0.086 hm³ and 2.10⁻⁴ for scenarios E1.2, E2.2 and E3.2, respectively. In scenario E1.2, the freshwater lens is less reduced than under wet conditions (from a maximum reduction of 30% to 21%). This is because the initial freshwater lens volume is much lower under dry conditions (from 2.1 hm³ to 1.28 hm³ for wet and dry conditions, respectively). Scenario E1.2 exhibits lower impact compared to scenarios E2.2 and E3.2., in which under dry conditions the freshwater lens almost disappears. The recovery is particularly slow since the recharge is zero for some time after the inundation. However, once the drought period is over, recovery accelerates, and a full recovery is reached after 1 month, 21 months and 22 months for E1.2, E2.2, and E3.2, respectively.

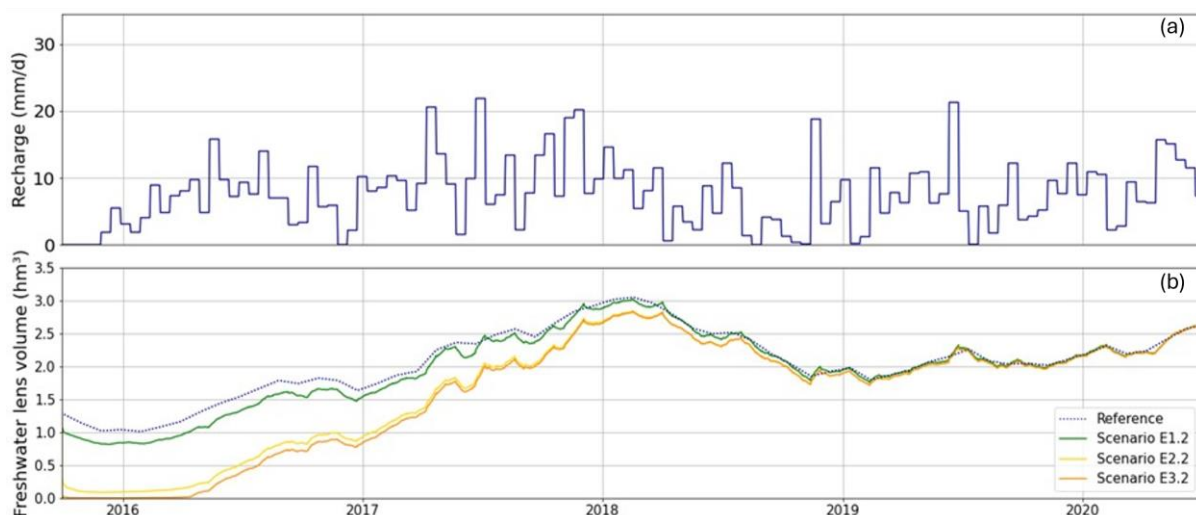


Figure 8-20: Freshwater lens volume in response to inundation scenarios in dry conditions. (a) Recharge used for scenarios (b) Freshwater lens volume.

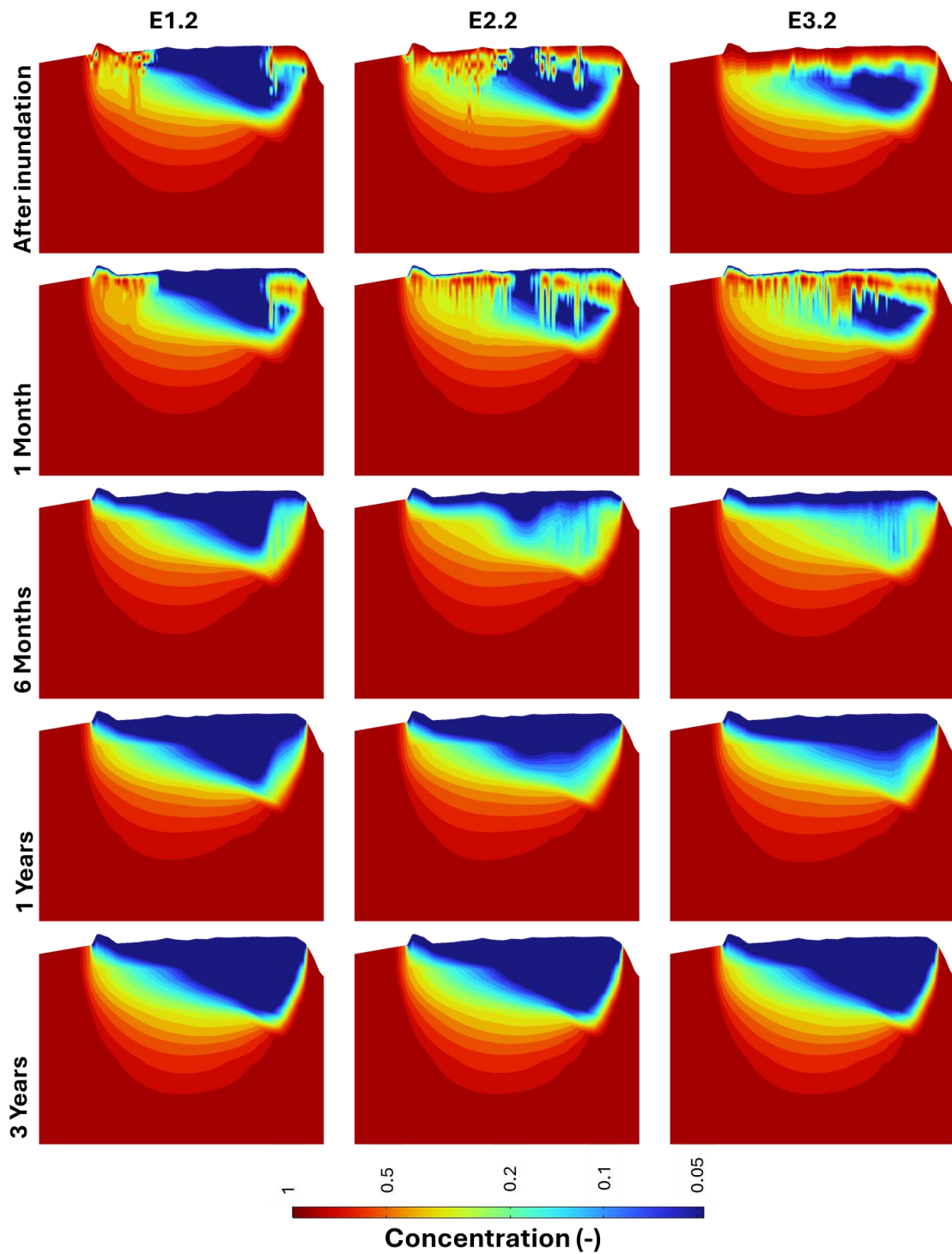


Figure 8-21: Vertical salinity profile in the central part of Laura Island at different times after the storm surge in wet conditions.

Recovery times under dry conditions are longer than the ones under wet conditions due mainly to the slower downwards movement of the plume in the absence of recharge. Moreover, higher salinities are observed in the upper part of the lens after 6 months, see Figure 8-21. However, in general the saltwater plume behaves in a similar way under wet and dry conditions, with a salty front and denser fingers migrating downward, followed by dilution and washing processes, and a recovery within 2 or 3 years to the pre-inundation volume. As for the wet scenarios, the lateral boundaries of the lens are mainly affected for the inundation in scenarios E1.2 and E2.2, whereas in scenario E3.2 the entire freshwater lens is damaged.

8.3.3 Effect and recovery in pumping wells

Figure 8-22 illustrates the salinity at the wells for the inundation scenarios under wet conditions.

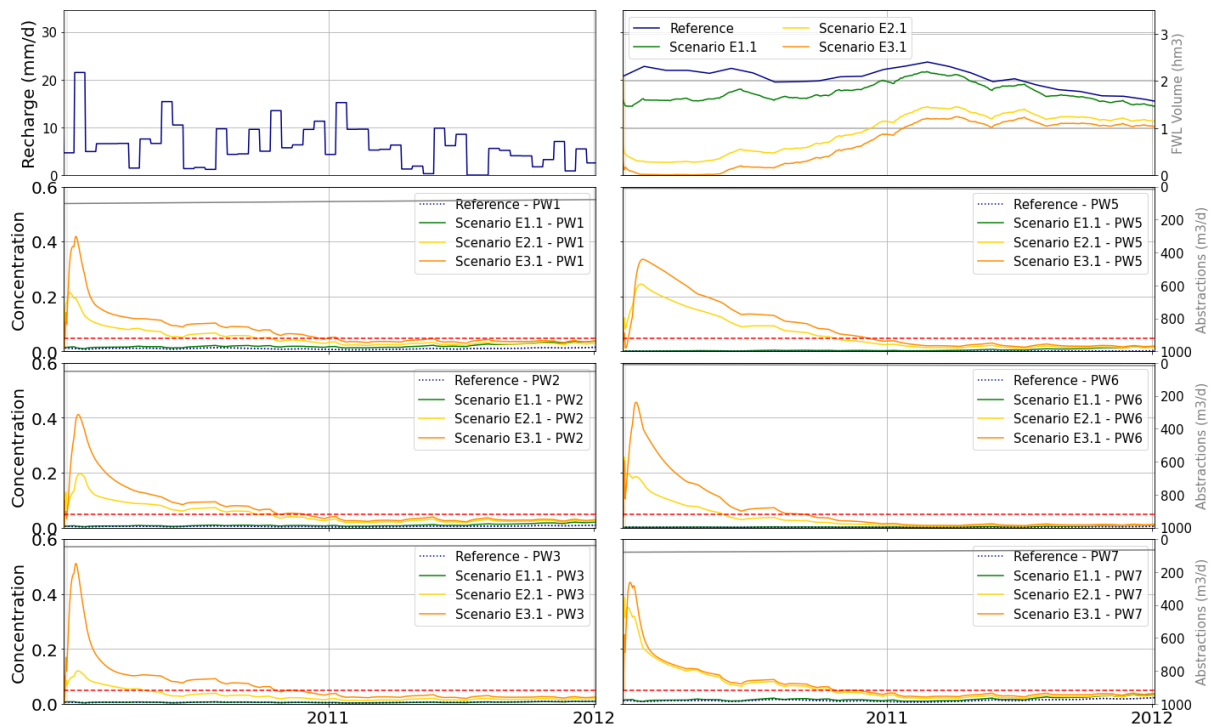


Figure 8-22: Pumping wells response to inundation scenarios in wet conditions: recharge function, freshwater lens volume and concentration at PW1, PW2, PW3, PW5, PW6 and PW7. The grey lines on the secondary y-axis represent abstraction and the red dashed line the 2500 µS/cm limit.

In scenario E1.1, pumping wells are not affected by the inundation because the loss of freshwater, mixing and increased salinities occur mainly at the lateral boundaries of the island. Salinities at the pumping wells in scenarios E2.1 and E3.1 increase significantly from the inundation exceeding for all the cases the drinking water limit of 2500 µS/cm. The salinization

of pumping wells occurs rapidly, taking less than 2 hours in scenario E2.1 and 1 hour in scenario E3.1. As expected, the increase in the salinity is more significant in scenario E3.1, resulting also in a longer recovery time (8 to 12 months) compared to scenario E2.1 (4 to 10 months). Note that the wells present two distinct types of breakthrough curves. Thus, in scenario E3.1, the wells PW5 and PW6 exhibit a peak characterized by a rapid ascent followed by a gradual decline over time. In contrast, the other wells display peaks with a smooth rise and fall.

Figure 8-23 shows the salinity at the wells for the inundation scenarios under dry conditions. Concentration at the pumping wells in scenario E1.2 shows negligible effect to the inundation event. Note that the well PW5 exceeds the drinking water limit for E1.2, however the increase in salinity at this well is induced by the pumping. Scenarios E2.2 and E3.2 present a more significant impact. The wells take longer to become salinized compared to wet conditions because there is no recharge to push the salt downwards. The reduced recharge also induces a lower maximum salinity reached at the pumping wells which remain salinized on a pseudo-plateau before gradually recovering once the recharge begins again. Thus, the recovery times takes between 7 to 10 months in E2.2 and from 10 to 12 months in E3.

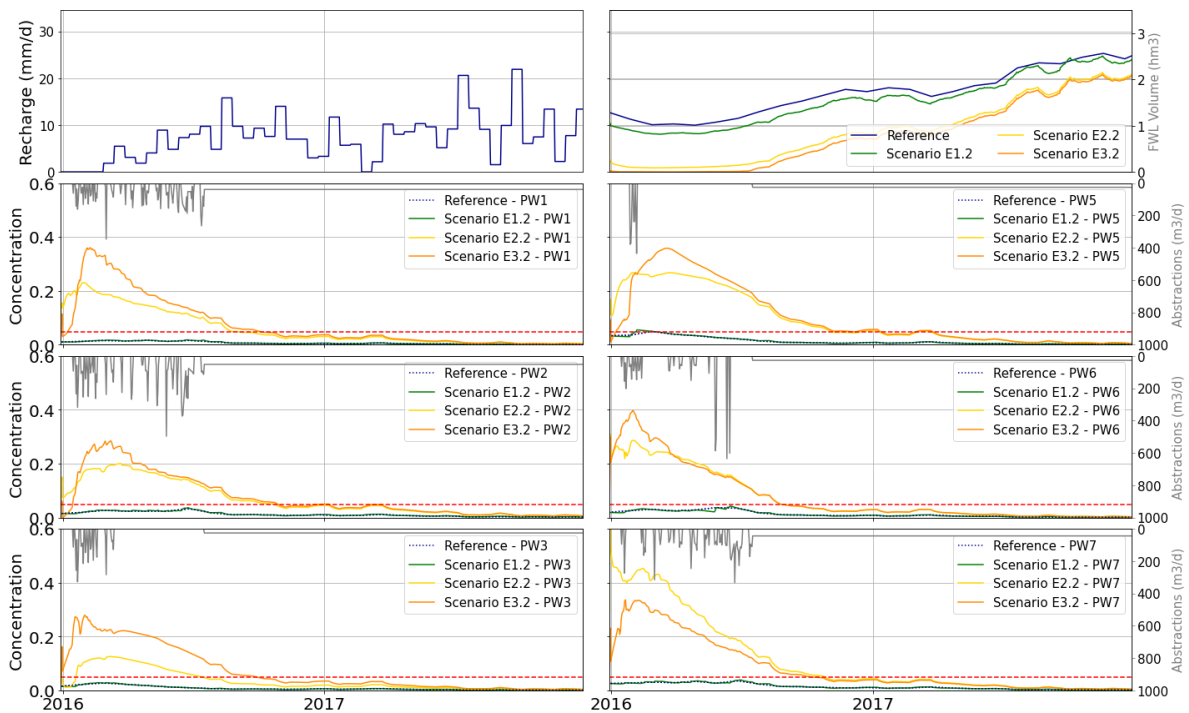


Figure 8-23: Pumping wells response to inundation scenarios in dry conditions: recharge function, freshwater lens volume and concentration at PW1, PW2, PW3, PW5, PW6 and PW7. The grey lines on the secondary y-axis represent abstraction and the red dashed line the 2500 µS/cm limit.

Note that, however, after and during the inundation event salinities at some wells are higher for scenario E2.2 than the ones for scenario E3.2 (see, for example, wells PW1, PW2, and PW7). This is because in scenario E3.2 the inundation on the entire island induces a spatially continuous salty front at the top of the freshwater lens whereas in scenario E2.2 several deep fingers irregularly distributed appear and sink being rapidly captured by the pumping wells, see Figure 8-21.

8.4 Scenarios main conclusions

In summary, the main conclusions of the scenarios are as follows:

- **Drought Events** Impact on the freshwater lens volume: Drought events have a significant impact on the volume of the freshwater lens, with reductions of ranging from 76% to 55% for extreme and average recovery scenarios. On the other hand, the freshwater lens demonstrates resilience by recovering relatively rapidly after drought events within 6 to 15 months.
- **Increased Pumping during Droughts:** An increase of 30% in pumping rates during drought events slightly impact on the freshwater lens volume. However, increased pumping leads to increased upconing with higher salinities near the wells. As a result, the wells PW1, PW2 and PW7, which present higher pumping rates, exceed the drinking water limit after the drought. The less vulnerable well is PW3, which presents lower pumping rates and is located in the middle of the island and far from the coastline. However, once pumping is reduced, the salinity at the wells decreases rapidly to pre-drought values.
- **Sea-Level Rise (SLR):** Sea level rise causes negligible impact on both the freshwater lens volume, which a maximum decrease lower than 5% for 1 meter rise, and salinity at the pumping wells. However, SLR causes the piezometric level to increase leading to the existence of ponded seawater in surface depressions. Moreover, due to the shape and bathymetry of the island, extreme SLR with 1 meter rise induces an inland migration of the interface on the ocean side with a movement of the freshwater lens of about 200 m at the middle of the island.
- **Inundation Events:** Inundation events caused by storm surges lead to saltwater infiltration and a temporary decrease in the volume of the freshwater lens, especially in scenarios with higher inundation heights, ranging from 30% to 99% of reduction. However, a relatively rapid recovery within 2 or 3 years is observed in all scenarios, highlighting the system's ability to recover from such events.
- **Impact on Pumping Wells from Inundation:** Inundation events impact salinities at the pumping wells, especially in scenarios with higher column heights, exceeding the drinking water limits in all of them. However, same as for the freshwater lens, a relatively rapid recovery is observed at the wells ranging from 7 to 12 months post-inundation. The wells PW1, PW2 and PW5 are the most vulnerable in terms of

recovery presenting longer times to reach salinities below the drinking water limit after the inundation event.

Table 8-3 and Table 8-4 provide a comprehensive overview of the results across all scenarios.

In Table 8-3 the following information can be found:

Information relative to the Freshwater lens volume:

- **Starting FWL volume:** The initial volume of the freshwater lens before the scenario event.
- **Minimum FWL volume:** The lowest volume the freshwater lens reaches during the scenario.

Recovery time: Time (in months) after the scenario event for the freshwater lens to recover different volume thresholds:

- **1.5 hm³:** Time to recover a specific volume of 1.5 hm³.
- **80% reference:** Time to recover 80% of the volume of the reference simulation.
- **50% reference:** Time to recover 50% of the volume of the reference simulation.
- **100% reference:** Time to recover the volume of the reference simulation.

Percent precipitation (relative to normal): This column shows the percentage of precipitation received during the scenario compared to the precipitation in the reference simulation (normal precipitation).

Table 8-4 summarizes the impacts of the scenarios on the pumping wells.

- **PW (Above potability limit by the end of the event):** Highlighted in bold are the pumping wells exceeding the potability limit by the end of the scenario event.
- **Months above potability limit due to the event:** Indicates the duration (in months) of the period that each pumping well remains above the potability limit as a result of the event.
- **Time to drop below potability limit threshold (months by the end of the event):** Shows the time (in months) after the end of the event it takes for each well to return to a concentration below the potability limit threshold.
- **Max reached EC due to event (µS/cm):** This column details the highest electrical conductivity (EC) level (in µS/cm) reached at each well due to the event.

- **Time to drop below potability limit threshold (months since last peak):** Indicates the time (in months) it takes for each well's EC to drop below the potability limit threshold since the last peak level reached during the event.

In general, the freshwater lens system on Laura Island demonstrates resilience to various environmental stresses, including droughts, sea-level rise, and inundation events, with relatively rapid recovery after extreme events. However, localized impacts around pumping wells during droughts and inundation events highlight the importance of monitoring and managing groundwater resources effectively.

Table 8-3: Summary of futures simulation scenarios results: Volume of the freshwater lens.

Scenario	Key aspects	Name	Description	Starting FWL volume	Minimum FWL Volume	Time to recover 1.5 hm ³ (months)	Time to recover 80% (months)	Time to Recover 50% (months)	Time to Recover 100% (months)	Percent precip (relative to normal)
A: Drought with Dry Recovery	Recharge function with Dec. 2008 – Nov. 2010 data replaced by data from the reference drought	A1	Reference Abstractions (calibrated model)	2.22	0.84 (42%)	9	12	2	54	55%
		A2	Increase in Abstractions of 30%	2.22	0.82 (57%)					
B: Drought with Average Recovery	Recharge function with Dec. 2014 – Nov. 2016 data replaced by data from the reference drought	B1	Reference Abstractions (calibrated model)	2.22	0.85 (46%)	8	6	1.25	5	45%
		B2	Increase in Abstractions of 30%	2.22	0.84 (45%)					
C: Extreme Double Drought	Recharge function with Dec. 2016 – Nov. 2020 data replaced by data from the reference drought (repeated)	C1	Reference Abstractions (calibrated model)	2.22	0.48 (24%)	6	15	8.5	Not reached by the end of the simulation (28 month later)	42%
		C2	Increase in Abstractions of 30%	2.22	0.47 (24%)					
D: Sea level rise (SLR)	Increase sea-level	D1	A2	2.22	-1	-	-	-	-	-
		D2	A2 + 25 cm	2.22	-1	-	-	-	-	-
		D3	A2 + 50 cm	2.22	-0.99	-	-	-	-	-

Scenario	Key aspects	Name	Description	Starting FWL volume	Minimum FWL Volume	Time to recover 1.5 hm3 (months)	Time to recover 80% (months)	Time to Recover 50% (months)	Time to Recover 100% (months)	Percent precip (relative to normal)	
		D4	A2 + 100 cm	2.22	-0.963	-	-	-	-	-	
E: Inundation	Inundation event with a return period of 25 years combined with SLR	E1	SLR +0.25 m	E1.1 - Wet condition	2.10	1.47 (70%)	-	7	Don't go below 50%	55	-
				E1.2 - Dry condition	1.28	0.81 (79%)	-	1	Don't go below 50%	33	-
		E2	SLR +0.5 m	E2.1 - Wet condition	2.10	0.27 (13%)	-	28	11	53	-
				E2.2 - Dry condition	1.28	0.086 (7%)	-	21	15	52	-
		E3	SLR +1.0 m	E3.1 - Wet condition	2.10	0.005 (0.24%)	-	32	13	59	-
				E3.2 - Dry condition	1.28	0.0002 (0.01%)	-	22	18	51	-

Table 8-4: Summary of futures simulation scenarios results: Salinity at the pumping wells.

Scenario	Key aspects	Name	Description	PW (Above potability limit by the end of the event)	Months above potability limit due to the event	Time to drop below potability limit threshold (months by the end of the event)	Max reached EC due to event (µS/cm)	Time to drop below potability limit threshold (months since last max)		
A: Drought with Dry Recovery	Recharge function with Dec. 2008 – Nov. 2010 data replaced by data from the reference drought	A1	Reference Abstractions (calibrated model)	PW1	32	3	6800	5.4		
				PW2	10	<1	3736	<1		
				PW3	0	-	2326	-		
				PW5	0	-	1190	-		
				PW6	0	-	1364	-		
				PW7	32	8	8285	10		
				A2	Increase in Abstractions of 30%	PW1	36	11	8862	13
		PW2	26			3	5017	5		
		PW3	6			<1	2915	<1		
		PW5	0			-	1499	-		
		PW6	0			-	1720	-		
		PW7	36			11	10872	13		
		B: Drought with Average Recovery	Recharge function with Dec. 2014 – Nov. 2016 data replaced by data from the reference drought			B1	Reference Abstractions (calibrated model)	PW1	1	-
				PW2	7			-	5068	1
PW3	0			-	1531			-		
PW5	4			-	3758			2.8		
PW6	2			-	4613			1		
PW7	12			-	5191			2.4		
B2	Increase in Abstractions of 30%			PW1	7			<1	3978	<1
				PW2	20	1	6969	3.5		
				PW3	0	-	1951	-		

Scenario	Key aspects	Name	Description	PW (Above potability limit by the end of the event)	Months above potability limit due to the event	Time to drop below potability limit threshold (months by the end of the event)	Max reached EC due to event (µS/cm)	Time to drop below potability limit threshold (months since last max)
				PW5 PW6 PW7	9 10 22	- - 1	5025 5693 6967	4 1.3 3.8
C: Extreme Double Drought	Recharge function with Dec. 2016 – Nov. 2020 data replaced by data from the reference drought (repeated)	C1	Reference Abstractions (calibrated model)	PW1	10.5	-	3969	<1
				PW2	34.5	-	5347	2
				PW3	0	-	2498	-
				PW5	32	-	5979	<1
				PW6	26	-	5418	<1
				PW7	40	-	6762	2.3
		C2	Increase in Abstractions of 30%	PW1	28	-	5026	<1
				PW2	57	1	6805	3.1
				PW3	2.5	-	2995	<1
				PW5	45	-	7113	2.2
			PW6	43.6	-	6538	2.2	
			PW7	59	1	8457	3.3	
D: Sea level rise (SLR)	Increase sea-level	D1	A2	Wells PW not affected				
		D2	A2 + 25 cm					
		D3	A2 + 50 cm					
		D4	A2 + 100 cm					
E: Inundation		E1	E1.1 - Wet condition	PW1	-	-	1139	-
	PW2			-	-	500	-	

Scenario	Key aspects	Name	Description	PW (Above potability limit by the end of the event)	Months above potability limit due to the event	Time to drop below potability limit threshold (months by the end of the event)	Max reached EC due to event (µS/cm)	Time to drop below potability limit threshold (months since last max)	
Inundation event with a return period of 25 years combined with SLR		SLR +0.25 m		PW3	-	-	388	-	
				PW5	-	-	236	-	
				PW6	-	-	134	-	
				PW7	-	-	1094	-	
			E1.2 – Dry condition	PW1	-	-	947	-	
				PW2	-	-	1908	-	
				PW3	-	-	1492	-	
				PW5	-	-	2895	0.9	
		E2	SLR +0.5 m	E2.1 – Wet condition	PW1		9.3	11290	8.7
					PW2		9.3	10374	8.7
					PW3		3.6	6300	3.6
				PW5		9.5	12912	9.5	
				PW6		4.5	13514	4.5	
				PW7		9.7	20496	9.4	
			E2.2 - Dry condition	PW1		7.5	12151	7.2	
				PW2		9.1	10548	7.2	
				PW3		5.5	6620	4.3	
				PW5		10.9	14131	9.1	
				PW6		7.4	16278	7.0	
				PW7		9.2	32636	9.7	

Scenario	Key aspects	Name	Description	PW (Above potability limit by the end of the event)	Months above potability limit due to the event	Time to drop below potability limit threshold (months by the end of the event)	Max reached EC due to event (µS/cm)	Time to drop below potability limit threshold (months since last max)
		E3	SLR +1.0 m	E3.1 - Wet condition	PW1	11.9	22067	11
					PW2	10.7	21715	9.14
					PW3	10.2	26939	9.10
					PW5	10.9	17680	10.2
					PW6	8.2	24076	7.7
					PW7	11.3	23306	9.4
					E3.2 - Dry condition	PW1	8.5	19910
			PW2	10		15008	7.7	
			PW3	8.4		14677	8	
			PW5	12.1		18886	8.7	
			PW6	7.4		20932	7	
			PW7	8.9		17715		

9 Management strategies and conclusions

The Laura Island freshwater lens system exhibits limited reserves with a finite volume of freshwater that fluctuates around 2 hm³ annually. However, these resources are ample relative to the system's dimensions. This characteristic implies two key aspects: The first one is the sensitivity to extreme conditions, where the lens is susceptible to rapid changes in response to external stress like drought or inundations. However, the lens is quite resilient and has rapid recovery. By integrating simulation results into management frameworks, stakeholders can devise effective measures to mitigate the extreme conditions effect on the lens while ensuring the sustainable utilization of groundwater resources for present and future generations.

9.1 To drought

- **Improve pumping strategy:** Distribute abstraction throughout time to avoid intense pumping peaks. The objective is to extract the same volume of water but with lower continuous pumping. Nevertheless, the extracted volume per well should not exceed 150 or 200 m³/day. In addition, spatial redistribution of pumping rates according to the well vulnerability during droughts is advisable. Extraction from wells located in the inner part of the island (e.g., PW 3) could be increased while reducing that from those closer to the coast (PW 7 and PW2) is advised.
- **New wells** located in the innermost part of the inland, and, therefore in the least vulnerable areas, can be a source of water during droughts and inundation periods. Specifically, the area between PW 3 and PW5 is proposed as a favourable location. However, it is important that these new wells should be positioned far enough to the existing ones, to avoid the combination of upconing effects (as simulated for PW1 and PW2 with high pumping rates).
- **Enhance Recharge Infrastructure:** Invest in infrastructure for artificial recharge of groundwater after drought periods to accelerate the recovery of the freshwater lens volume and to enhance groundwater storage and resilience for future droughts. Abarca et al. (2006) demonstrated that the efficiency of artificial recharge in coastal areas is greater than that belief (i.e., the allowable increase in inland pumping might exceed the recharged flow rate). This is because artificial recharge not only increases available resources but also protects inland wells from salinization.

9.2 To Sea Level Rise

- **No particular management strategies** are needed for managing pumping and the freshwater lens volume since neither of them are affected by SLR without inundation events.

- **Land Use Planning:** Due to the increasing groundwater base level (sea level), the groundwater will rise above the ground elevation in some low topographic areas, producing their inundation by fresh groundwater. Therefore, controlling the land use planning will be necessary, avoiding new constructions and promoting their use as freshwater management areas. One option is to use these areas as freshwater reservoirs, e.g., green -blue nature-based structures that can be used as temporary flooding parks that serve as discharge groundwater areas during high waters and recharge ponds during low water seasons.

9.3 To inundation events

- **Coastal Protection Measures:** Implement coastal protection measures to avoid inland inundation such as seawalls, dikes, and beach nourishment to mitigate the impacts of inundations.
- **Well protection measures:** The vulnerability of the wells depends on the susceptibility of inundation of the area around the well. Therefore, any measurements to protect pumping wells area from inundation would be beneficial.
- **Pumping strategy:** After an inundation event, in order to satisfy the demand of freshwater, pumping should shift to non-inundated areas, i.e., to the innermost wells like PW 3. On the other hand, pumping from wells might be effective to remove saltwater and restore drinking water quality in areas near the coastline, where the freshwater lens is more disturbed.
- **New wells** located in the innermost part of the inland can be a less vulnerable source of resources during draughts and inundation periods. A location between PW3 and PW5 is considered the most favourable area.
- **Groundwater monitoring:** Continuous monitoring of groundwater levels and salinity is essential for early detection of saltwater intrusion following storm surges. Real-time data can help authorities take prompt action to mitigate impacts.
- **Diversify Water Sources:** Rainwater harvesting for demand during the recovery period and artificial recharge to accelerate the recovery of the lens.

9.4 Other improvements

- **Groundwater monitoring** A detailed record of abstractions, together with continuous monitoring of groundwater levels and salinity can be used to better calibrate the numerical model and even to train artificial intelligence algorithms that may be used as early warning systems to immediately modify pumping strategies.
- **Enhance Early Warning Systems:** Implement a robust early warning system that integrates meteorological data by calculating monthly water balance, salinity measurements, etc.

- **Implement Water Conservation Measures:** Develop and promote water conservation practices, water-efficient technologies and implement policies and regulations to manage groundwater abstraction during droughts to reduce overall water demand during drought periods.
- **Diversify Water Sources:** Explore alternative water sources such as rainwater harvesting, desalination, and wastewater recycling to supplement groundwater during droughts.

10 References

- Abarca, E., Vázquez-Suñé, E., Carrera, J., Capino, B., Gámez, D., Batlle, F., 2006. Optimal design of measures to correct seawater intrusion. *Water resources research* 42.
- Anthony, S.S., 1985. Preliminary findings of the near surface geology of Laura, Majuro atoll, Marshall Islands:
- Antoniou, E.A., 2008.
- Bear, J., 1972. Dynamics of fluids in porous media. Elsevier Scientific Publishing.
- Channel, P., Godín, G., 1972. The analysis of tides. University of.
- Darcy, H., 1856. Les fontaines publiques de la ville de Dijon. Exposition et application des principes à suivre et des formules à employer dans les questions de distribution d'eau: ouvrage terminé par un appendice relatif aux fournitures d'eau de plusieurs villes au filtrage des eaux et à la fabrication des tuyaux de fonte, de plomb, de toile et de bitume. Dalmont.
- Ferris, J.G., 1952. Cyclic fluctuations of water level as a basis for determining aquifer transmissibility. US Geological Survey.
- Goyetche, T., Pool, M., Carrera, J., Diego-Feliu, M., Perez, L.M., Folch, A., Luquot, L., 2023. Using the tidal method to develop a conceptual model and for hydraulic characterization at the Argentona research site, NE Spain. *Hydrogeology Journal* 31, 2099–2114.
- Hamlin S. N., Anthony , S. S., 1987. Ground-water resources of the Laura area, Majuro Atoll, Marshall Islands.
- Jacob, C., 1950. Flow of groundwater. *Engineering hydraulics* 321–386.
- Jansen S.W., 2021. Quantifying fresh groundwater lens behaviour for Laura island.
- Koda, K., 2018. Freshwater Lens Conservation during Drought. *Journal of Rainwater Catchment Systems* 24, pp.15-21.
- Koda, K., Kobayashi, T., Lorennj, R., Robert, A., DeBrum, H., Lucky, J., Paul, P., 2017. Freshwater Lens Observation: Case Study of Laura Island, Majuro Atoll, Republic of the Marshall Islands. *World Academy of Science, Engineering and Technology International Journal of Agricultural and Biosystems Engineering* 11.
- Neuman, S.P., 1972. Theory of flow in unconfined aquifers considering delayed response of the water table. *Water Resources Research* 8, 1031–1045.
- Palaseanu-Lovejoy, M., Poppenga, S.K., Danielson, J.J., Tyler, D.J., Gesch, D.B., Kottermair, M., Jalandoni, A., Carlson, E., Thatcher, C.A., Barbee, M.M., 2018. One-meter topobathymetric digital elevation model for Majuro Atoll, Republic of the Marshall Islands, 1944 to 2016 (Report No. 2018–5047), Scientific Investigations Report. Reston, VA. <https://doi.org/10.3133/sir20185047>

- Presley, T.K., 2005. Effects of the 1998 Drought on the Freshwater Lens in the Laura Area, Majuro Atoll, Republic of the Marshall Islands (Report No. 2005–5098), Scientific Investigations Report. <https://doi.org/10.3133/sir20055098>
- Werner, A.D., Sharp, H.K., Galvis, S.C., Post, V.E.A., Sinclair, P., 2017. Hydrogeology and management of freshwater lenses on atoll islands: Review of current knowledge and research needs. *Journal of Hydrology* 551, 819–844. <https://doi.org/10.1016/j.jhydrol.2017.02.047>
- White, I., Falkland, T., Crennan, L., Jones, P., Metutera, T., Etuati, B., Metai, 1999. Groundwater recharge in low coral islands: Bonriki, South Tarawa, Kiribati; issues, traditions and conflicts in groundwater use and management.

Appendix

A. Conceptual Model

A.1 Monitoring wells

The piezometers used for the HYCOS campaign, MCAP campaigns and manual measurements, as well as the period of measurements, frequency and number of records are shown in Table 10-1, Table 10-2, Table 10-3 and Table 10-4.

Table 10-1: Monitoring wells short term data for the HYCOS campaign.

Site	Bore name (Depth ft)	Start time (dd/mm/yy hh:mm)	End time (dd/mm/yy hh:mm)	Frequency (min)	Duration (h)	Records
1	33	03/02/2008 14:40	04/02/2008 15:25	5	24.8	297
	43	03/02/2008 14:35	05/02/2008 14:05	5	47.5	570
2	23	02/02/2008 15:10	03/02/2008 13:15	5	22.1	265
	33	02/02/2008 15:00	03/02/2008 13:10	5	22.2	266
	43	02/02/2008 15:05	03/02/2008 13:15	5	22.2	266
3	18	05/02/2008 15:40	06/02/2008 17:10	5	25.5	306
	28	05/02/2008 15:45	06/02/2008 16:20	5	24.6	295
	38B	05/02/2008 15:50	06/02/2008 17:10	5	25.3	304
	48	05/02/2008 15:55	06/02/2008 17:10	5	25.3	303
4	18	29/01/2008 16:10	30/01/2008 16:25	5	24.3	291
	48	29/01/2008 16:04	30/01/2008 16:34	5	24.5	294
	58	29/01/2008 15:50	30/01/2008 16:40	5	24.8	298
	68	29/01/2008 15:39	30/01/2008 16:44	5	25.1	301
5	18	30/01/2008 17:45	31/01/2008 14:20	5	20.6	247
	28	30/01/2008 17:50	31/01/2008 14:25	5	20.6	247
	33	30/01/2008 18:00	31/01/2008 14:30	5	20.5	246
	48	30/01/2008 18:10	31/01/2008 14:35	5	20.4	245
6	33	07/02/2008 14:50	08/02/2008 12:05	5	21.2	255
	43	07/02/2008 14:55	08/02/2008 12:10	5	21.2	255
	48	07/02/2008 15:00	08/02/2008 12:15	5	21.2	255
7	18	31/01/2008 15:40	01/02/2008 14:30	5	22.8	274
	53	31/01/2008 15:35	01/02/2008 14:30	5	22.9	275
	63	31/01/2008 15:30	01/02/2008 14:25	5	22.9	275
8	28	06/02/2008 18:20	07/02/2008 13:10	5	18.8	226
	38	06/02/2008 18:25	07/02/2008 13:05	5	18.7	224
	48	06/02/2008 18:30	07/02/2008 13:10	5	18.7	224
	58	06/02/2008 18:40	07/02/2008 13:10	5	18.5	222
9	33	04/02/2008 16:55	05/02/2008 14:35	5	21.7	260
	43	04/02/2008 17:05	05/02/2008 14:40	5	21.6	259
	53	04/02/2008 16:45	05/02/2008 14:35	5	21.8	262
10	13	01/02/2008 15:45	02/02/2008 13:05	5	21.3	256
	43	01/02/2008 16:05	02/02/2008 13:05	5	21.0	252

Site	Bore name (Depth ft)	Start time (dd/mm/yy hh:mm)	End time (dd/mm/yy hh:mm)	Frequency (min)	Duration (h)	Records
	53	01/02/2008 15:55	04/02/2008 15:45	5	71.8	862
PW	1	28/01/2008 18:15	29/01/2008 14:02	1	19.8	1187
	2	28/01/2008 18:45	29/01/2008 14:20	1	19.6	1175

Table 10-2: Monitoring wells long term data for the HYCOS campaign

Site	Bore name (Depth ft)	Start time (dd/mm/yy hh:mm)	End time (dd/mm/yy hh:mm)	Frequency (min)	Duration (Day)	Records
1	43	08/02/2008 14:20	14/05/2008 16:20	10	96	13836
		22/07/2008 13:15	07/11/2008 16:35	10	108	15572
		07/11/2008 16:45	25/02/2009 11:55	10	110	15811
		25/02/2009 12:15	16/06/2009 13:25	10	111	15991
3	38A	22/11/2007 16:30	20/12/2007 17:45	5	28	8079
4	48	08/02/2008 14:25	14/05/2008 16:05	10	96	13834
		22/07/2008 14:20	07/11/2008 16:50	10	108	15567
		07/11/2008 16:55	25/02/2009 12:35	10	110	15814
		25/02/2009 13:05	16/06/2009 15:35	10	111	15999
9	43	08/02/2008 14:25	14/05/2008 15:45	10	96	13832
		22/07/2008 15:05	07/11/2008 17:05	10	108	15564
		07/11/2008 17:10	25/02/2009 13:30	10	110	15818
		25/02/2009 13:50	16/06/2009 16:20	10	111	15999

Table 10-3: Monitoring wells data for the MCAP campaign

Site	Bore name (Depth ft)	Start time (dd/mm/yy hh:mm)	End time (dd/mm/yy hh:mm)	Frequency (min)	Duration (Day)	Records
1	33	06/05/2022 16:56	11/06/2022 15:06	10	36	5173
		11/06/2022 15:16	03/11/2022 13:16	60	145	3478
3	28	07/05/2022 12:18	11/06/2022 13:38	10	35	5048
		11/06/2022 13:52	03/11/2022 14:52	60	145	3481
	38B	07/05/2022 12:44	11/06/2022 13:34	10	35	5045
		11/06/2022 13:43	03/11/2022 14:43	60	145	3481
4	48	11/06/2022 12:16	05/11/2022 11:16	60	147	3527
6	33	07/05/2022 15:46	11/06/2022 12:36	10	35	5021
		11/06/2022 12:44	05/11/2022 14:44	60	147	3530
	43	07/05/2022 15:58	11/06/2022 12:38	10	35	5020
		11/06/2022 12:55	07/11/2022 15:55	60	149	3579
9	33	11/06/2022 11:32	05/11/2022 15:32	60	147	3532

Site	Bore name (Depth ft)	Start time (dd/mm/yy hh:mm)	End time (dd/mm/yy hh:mm)	Frequency (min)	Duration (Day)	Records
10	13	11/06/2022 11:56	05/11/2022 13:56	60	147	3530
	43	09/05/2022 14:36	11/06/2022 10:36	10	33	4728
		11/06/2022 11:06	05/11/2022 14:16	10	147	21187
PW	2	17/05/2022 16:48	11/06/2022 16:38	10	25	3599
		11/06/2022 16:50	05/11/2022 13:50	60	147	3525
	3	17/05/2022 17:21	11/06/2022 13:01	10	25	3574
		11/06/2022 13:15	05/11/2022 13:15	60	147	3528
	6	17/05/2022 15:56	11/06/2022 14:06	10	25	3589
		11/06/2022 14:19	05/11/2022 12:19	60	147	3526
	7	17/05/2022 15:33	11/06/2022 15:13	10	25	3598
		11/06/2022 15:28	05/11/2022 12:28	60	147	3525

Table 10-4: Counts of manual measurements and measured parameters.

Site	Bore name	Water level	EC Bottom	EC Surface	Temp. bottom	Temp. surface	E.Coli	First measure (dd/mm/yy)	Last measure (dd/mm/yy)
1	23	5	3	-	-	-	-	06/1998	31/05/2016
	33	18	10	7	3	4	2	06/1998	31/05/2016
	43	17	9	6	3	3	1	06/1998	31/05/2016
2	23	18	7	7	2	4	3	06/1998	31/05/2016
	28	1						22/11/2007	22/11/2007
	33	16	10	7	4	5	3	06/1998	31/05/2016
	43	18	11	7	3	3	3	06/1998	31/05/2016
3	17	3	3	4	1	1	3	02/09/2008	24/02/2009
	18	15	8	4	4	3		06/1998	31/05/2016
	28	17	9	6	3	2	3	06/1998	31/05/2016
	38					1		24/02/2009	24/02/2009
	38A	14	9	7	4	3	3	15/11/2007	31/05/2016
	38B	16	8	5	3	2	2	06/1998	31/05/2016
	48	15	7	4	1	1	3	06/1998	31/05/2016
4	18	18	10	7	4	4	3	06/1998	31/05/2016
	48	18	10	7	5	4	2	06/1998	31/05/2016
	58	18	10	7	4	4	3	06/1998	31/05/2016
	68	18	10	7	4	4	3	06/1998	31/05/2016
5	18	10	4	2	1	1	1	06/1998	04/03/2016
	28	13	6	2	1	1	1	06/1998	31/05/2016
	33	8	3	1			1	06/1998	09/03/2016

Site	Bore name	Water level	EC Bottom	EC Surface	Temp. bottom	Temp. surface	E.Coli	First measure (dd/mm/yy)	Last measure (dd/mm/yy)
	38	1						04/12/2007	04/12/2007
	48	12	5	1	1	1		06/1998	31/05/2016
6	13	2	2					06/1998	09/03/2016
	33	13	5	2	2	2		06/1998	31/05/2016
	43	12	5	1	1	1		06/1998	31/05/2016
	48	13	6	2	2	2		06/1998	31/05/2016
	18	12	5	7	2	4	3	06/1998	26/08/2009
7	28					1		25/02/2009	25/02/2009
	53	11	6	5	2	2	3	06/1998	05/2014
	63	10	5	4	1	1		06/1998	26/08/2009
	68	1	1	1	1	1		05/2014	05/2014
	28	17	7	7	4	7	1	06/1998	31/05/2016
8	38	15	8	4	3	3	1	06/1998	31/05/2016
	48	10	3					06/1998	31/05/2016
	58	13	6	2	1	1	1	06/1998	31/05/2016
	28	14	11	10	5	7	3	06/1998	31/05/2016
9	33	20	11	9	4	5	4	06/1998	31/05/2016
	43	15	7	4	3	1	1	06/1998	31/05/2016
	53	6						16/11/2007	19/12/2007
	13	13	7	3	2	2	1	06/1998	31/05/2016
10	43	13	7	3	2	2	1	06/1998	31/05/2016
	53	9	3					06/1998	31/05/2016

A.2 Recarge estimation

Figure 10-1 shows the daily soil water balance obtained from the precipitation and evapotranspiration information.

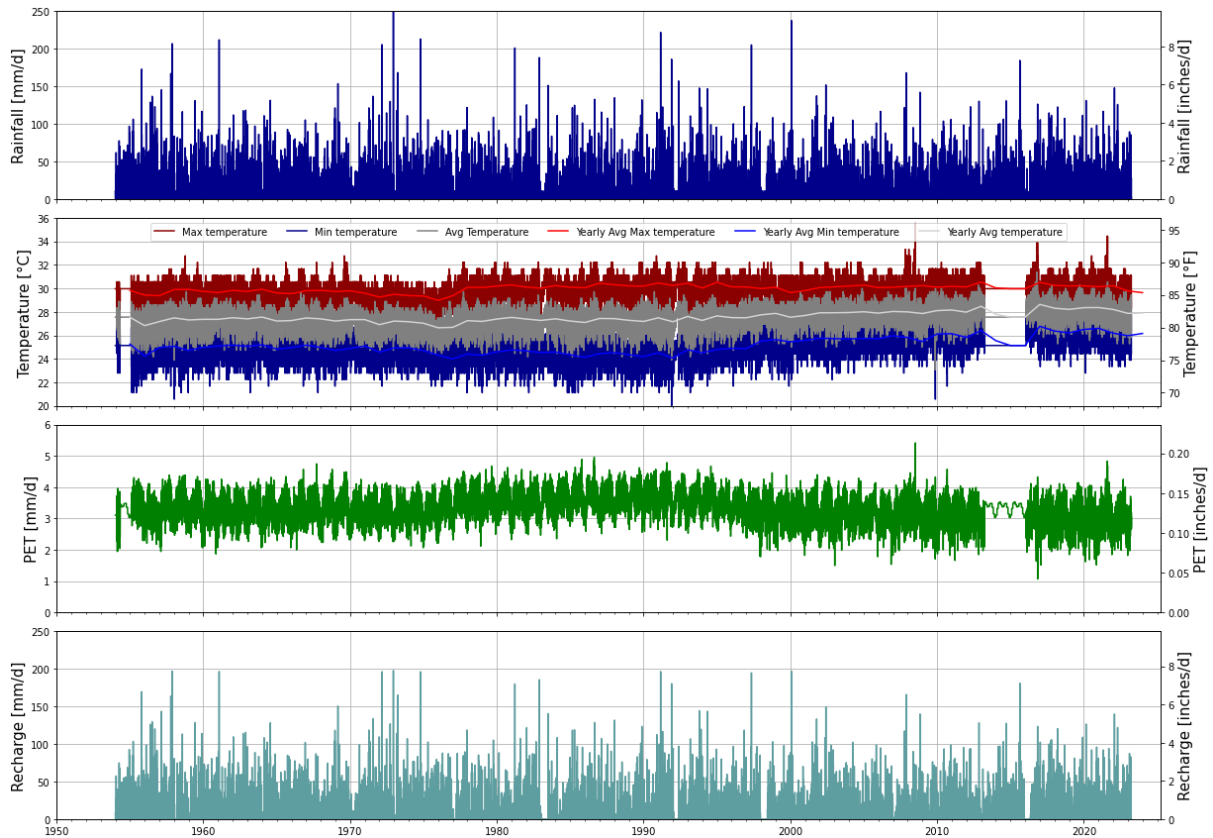


Figure 10-1: Completed rainfall series, temperature, PET and Calculated Recharge.

A.3 Hydraulic Parameters

Table 10-5 presents the hydraulic parameters found in the literature for the different hydrogeological units, including hydraulic conductivity, porosity, unit thickness, storage coefficient, and longitudinal and transversal dispersivities.

Table 10-5: Hydraulic and transport parameters extracted from the literature.

Reference		Griggs and Peterson (1993)	Mink (1996)	Koda (2018)	Jansen (2021)	
Parameters	Upper Sediment/Upper Holocene	Kxy [m/d]	60.48	60.48	31.104	30-80
		Kz [m/d]	-	6.096	1.9872	15
		n [-]	0.2	-	-	0.2
		b [m]		-	-	6-12
	Lower Sediment/Lower Holocene	Kxy [m/d]	604.8	-	354.24	350
		Kz [m/d]	-	-	44.928	45
		n [-]	0.2	-	-	0.2
		b [m]		-	-	6-15
	Upper Limestone	Kxy [m/d]	0.100224	-	-	-
		Kz [m/d]	-	-	-	-
		n [-]	0.3	-	-	-
		b [m]		-	-	-
	Lower Limestone/Pleistocene	Kxy [m/d]	6048	609.6	501.12	500
		Kz [m/d]	-	60.96	50.112	50
		n [-]	0.3	-	-	0.3
		b [m]		-	-	23-38
Storage	Sy	0.18	-	-	0.15	
	Ss	-	-	-	1.00E-05	
Dispersivity	α_L [m]	0.4-8	-	-	1.7	
	α_{th} [m]	-	-	-	0.39	
	α_{tv} [m]	0.05	-	-	0.39	

B. Numerical Model

B.1 Governing Equations

- Flow equation.

Flow in porous media is described by combining Darcy's law (Darcy, 1856) with the continuity equation and the equation of state for the pore fluid (Bear, 1972). Darcy's law is a phenomenological law that relates the specific discharge, or the Darcy velocity, to the hydraulic gradient and the hydraulic conductivity. The resulting equation governs the fluid pressure.

The equation for the Darcy velocity can be written as:

$$\vec{u} = -\frac{\vec{k}}{\mu}(\vec{\nabla}p + \rho g \vec{\nabla}z) \quad \text{Eq 10-1}$$

where \vec{u} is the Darcy velocity or the specific discharge vector [$L^3L^{-2}T^{-1}$], \vec{k} is the permeability of the porous medium [L^2], μ is the fluid dynamic viscosity [$ML^{-1}T^{-1}$], p is the fluid pressure [$ML^{-1}T^{-2}$], ρ is the fluid density [ML^{-3}], g is the gravitational acceleration [LT^{-2}] and z [L] refers to the elevation.

The continuity equation for saturated flow in a porous medium is:

$$\frac{\partial(\rho\phi)}{\partial t} + \vec{\nabla} \cdot (\rho\vec{u}) = Q_m \quad \text{Eq 10-2}$$

where, ϕ is the porosity [-] and Q_m is a mass source term [$ML^{-3}T^{-1}$]. By combining equations 9-1 and 9-2, the generalized governing equation leads to:

$$\frac{\partial(\rho\phi)}{\partial t} + \vec{\nabla} \cdot \left[-\frac{\vec{k}\rho}{\mu}(\vec{\nabla}p + \rho g \vec{\nabla}z) \right] = Q_m \quad \text{Eq 10-3}$$

The time derivative can be expanded. By defining porosity and density as function of pressure and applying the chain rule, the first term can be written as:

$$\frac{\phi\partial\rho}{\partial t} + \frac{\rho\partial\phi}{\partial t} = \phi \frac{\partial\rho}{\partial p} \frac{\partial p}{\partial t} + \rho \frac{\partial\phi}{\partial p} \frac{\partial p}{\partial t}, \quad \text{Eq 10-4}$$

where the first term is due to compressibility of the fluid in the pores and the second is due to compressibility of the bulk aquifer material. By inserting the definition of fluid compressibility ($X_f = (1/\rho)(\partial\rho/\partial p)$) and rearranging, the generalized equation is written as

$$\rho S \frac{\partial p}{\partial t} + \vec{\nabla} \cdot \left[-\frac{\vec{k}\rho}{\mu} (\vec{\nabla}p + \rho g \vec{\nabla}z) \right] = Q_m, \quad \text{Eq 10-5}$$

where S is the storage coefficient [$M^{-1}L^1T^2$], which includes contributions due to compressibility of the bulk aquifer material and the fluid in the pores.

- Transport equation.

Solute transport is described by the advective-dispersive transport equation (Bear, 1972) that reads as:

$$(\phi) \frac{\partial c_i}{\partial t} + \vec{u} \cdot \nabla c_i = \nabla \cdot [(\mathbf{D}_{D,i} + D_m) \nabla c_i], \quad \text{Ec.4}$$

where c_i is the concentration of species i , $\mathbf{D}_{D,i}$ [L^2T^{-1}] is the dispersion tensor in terms of the longitudinal (α_L) and transverse transversal (α_T) dispersivities [L] and D_m is the molecular diffusion coefficient [L^2T^{-1}].

The coupling between the flow and salt transport equations is achieved through a linear equation that relates the fluid density to the concentration of dissolved salts, given by.

$$\rho = \rho_0 + \beta c_i \quad \text{Ec.5}$$

where ρ_0 is the freshwater density (1,0 kg/l) and β is defined as $\beta = (\rho_s - \rho_0)/(c_s - c_0)$ with ρ_s and c_s the density and concentration of seawater, respectively.

B.2 Pumping wells

Table 10-6 shows the coordinates of the pumping wells included in the numerical model, as well as their pumping rate considered for the steady state simulation.

Table 10-6: Pumping wells coordinates and pumping rates considered for the steady state simulation.

PW		West Arm Coordinates	North Arm Coordinates	East Arm Coordinates	South Arm Coordinates	Centre Coordinates	Elevation (m)	Steady-State pumping rate (m ³ /d)
1	X	503959.9	504005.6	504051.8	504006.2	504005.8	-3.26	142.01
	Y	789745.4	789792.4	789744.5	789700.9	789744.8		
2	X	503923.6	503970.2	504016.5	503970.2	503970.1	-2.62	50.81
	Y	789875.6	789921.2	789875.1	789831.4	789875.5		
3	X	503782.4	-	503872.2	-	503826.7	-2.81	59.24
	Y	790072.4		790073.2		790072.5		
5	X	503848.7	503895.4	503939.7	503895.3	503895.3	-2.49	82.33
	Y	790727.5	790771.5	790727.7	790682.8	790727.4		
6	X	503908.8	503954.5	503999.1	503954.9	503954.7	-2.25	47.92
	Y	790940.7	790986.3	790940.4	790895.8	790940.7		
7	X	503964.1	504010.8	504058.3	504011.3	504010.8	-2.69	75.07
	Y	790553.2	790598.7	790553.5	790509.8	790553.4		

B.3 Observation wells

Table 10-7 illustrates the names, coordinates and depth of the observation wells included in the numerical model.

Table 10-7: Observation wells details.

MW	X Coordinates	Y Coordinates	Elevation from DEM (m)	Depth (ft)	Depth (m)	Z Coordinates model
1	503966.057	790963.747	1.62	33	10.1	-8.48
				43	13.1	-11.48
2	504073.045	790572.667	2.23	23	7.0	-4.77
				33	10.1	-7.87
				43	13.1	-10.87

MW	X Coordinates	Y Coordinates	Elevation from DEM (m)	Depth (ft)	Depth (m)	Z Coordinates model
3	503733.924	790585.478	1.55	18	5.5	-3.95
				28	8.5	-6.95
				38B	11.6	-10.05
				48	14.6	-13.05
4	504022.369	790245.731	2.12	18	5.5	-3.38
				48	14.6	-12.48
				58	17.7	-15.58
				68	20.7	-18.58
5	503759.555	790137.755	1.34	18	5.5	-4.16
				28	8.5	-7.16
				33	10.1	-8.76
				48	14.6	-13.26
6	503618.215	790147.856	1.76	43	13.1	-11.34
7	504033.448	789971.797	1.87	18	5.5	-3.63
				53	16.2	-14.33
				63	19.2	-17.33
8	503730.106	789905.606	1.43	28	8.5	-7.07
				38	11.6	-10.17
				48	14.6	-13.17
				58	17.7	-16.27
9	504133.624	789550.113	1.49	33	10.1	-8.61
				43	13.1	-11.61
				53	16.2	-14.71
10	504132.408	790228.726	2.28	13	4.0	-1.72
				43	13.1	-10.82
				53	16.2	-13.92

C. Model Calibration

C.1 Daily Transient Model

In this Appendix, the comparison between measured and computed normalized heads and concentrations at different observation wells for the HYCOS and MCAP daily campaigns is illustrated.

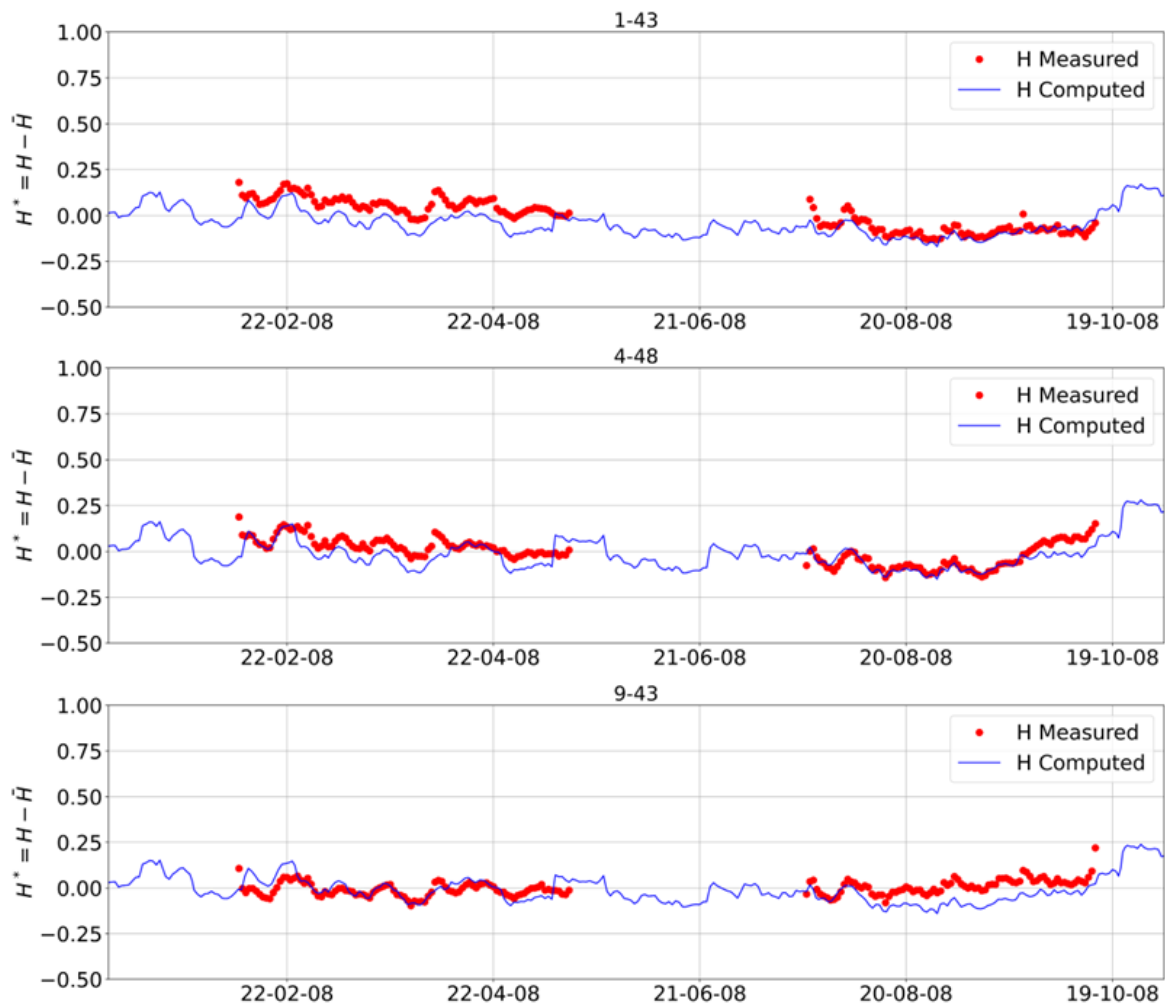


Figure 10-2: Calculated (blue line) and measured (red dots) normalized heads at three multi-level observation wells (1-43, 4-48 and 9-43) for the HYCOS (left) and MCAP (right) campaigns from the calibrated Daily Transient Model.

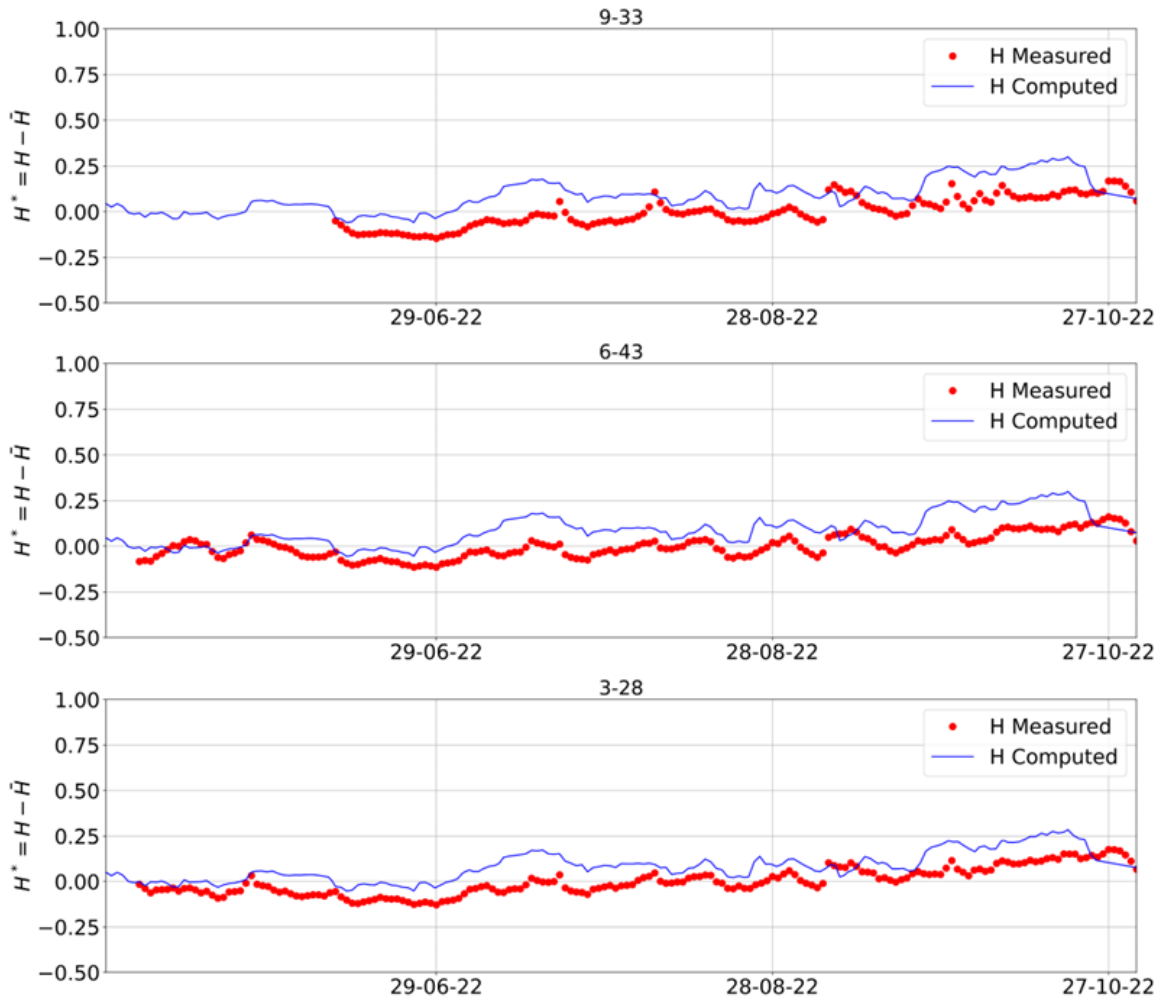


Figure 10-3: Calculated (blue line) and measured (red dots) normalized heads at three multi-level observation wells (9-33, 6-43 and 3-28) for the HYCOS (left) and MCAP (right) campaigns from the calibrated Daily Transient Model.

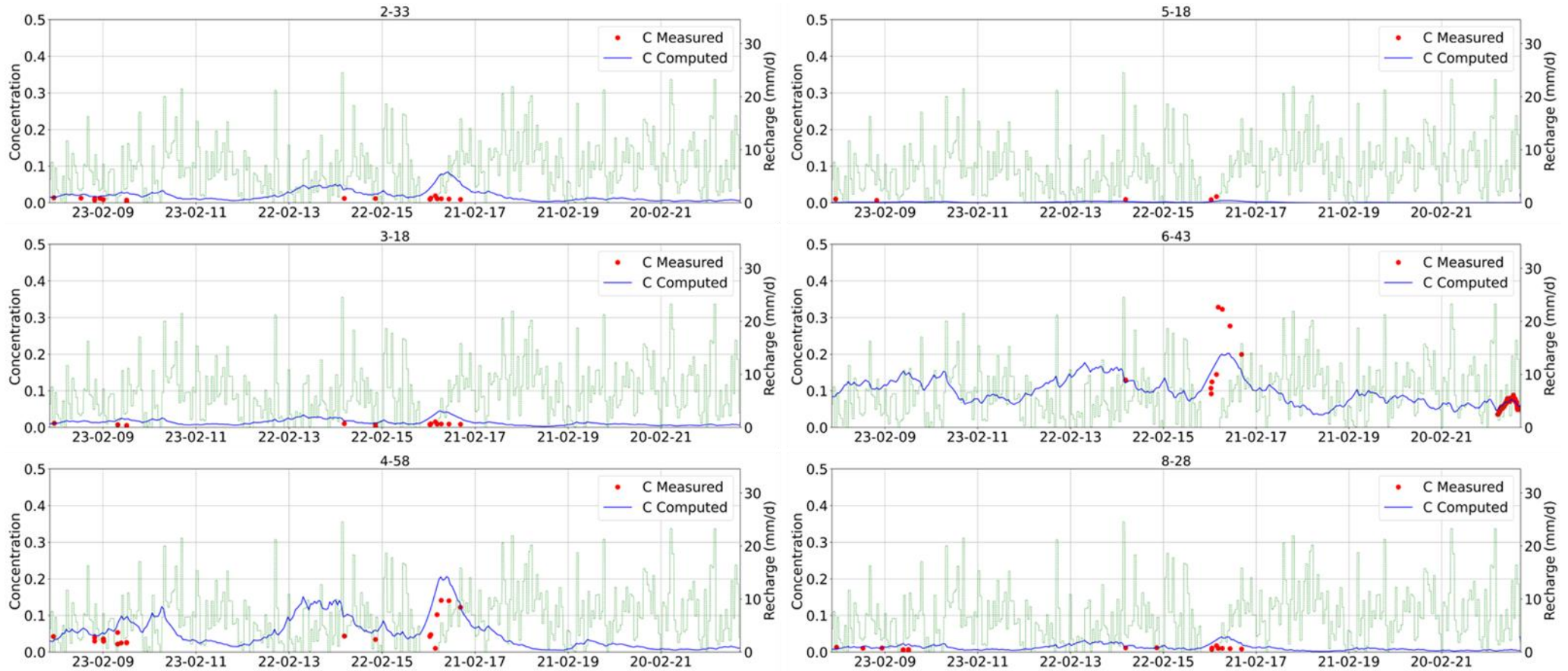


Figure 10-4: Calculated (blue line) and measured (red dots) normalized concentration at six multi-level observation wells (2-33, 3-18, 4-58, 5-18, 6-43 and 8-28) from the calibrated Daily Transient Model.

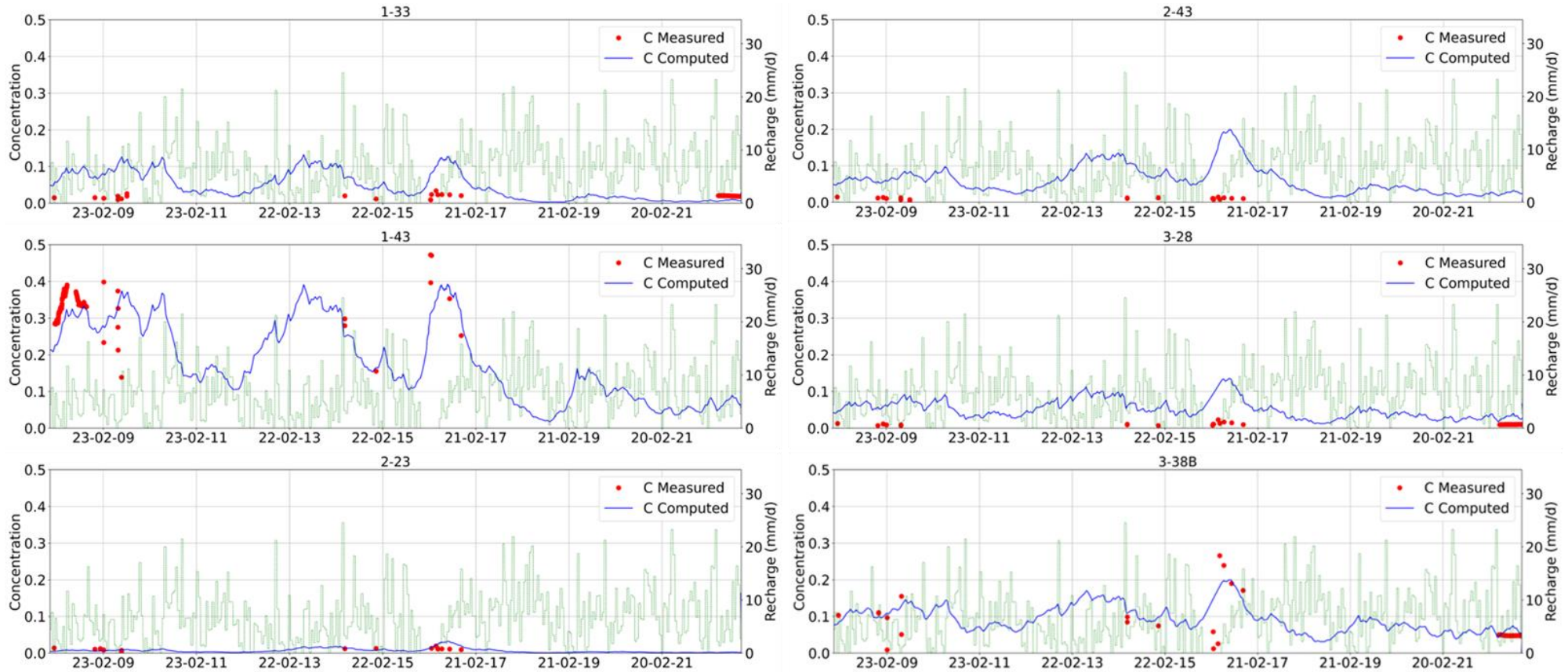


Figure 10-5: Calculated (blue line) and measured (red dots) normalized concentration at six multi-level observation wells (1-33, 1-43, 2-23, 2-43, 3-28, 3-38B) from the calibrated Daily Transient Model.

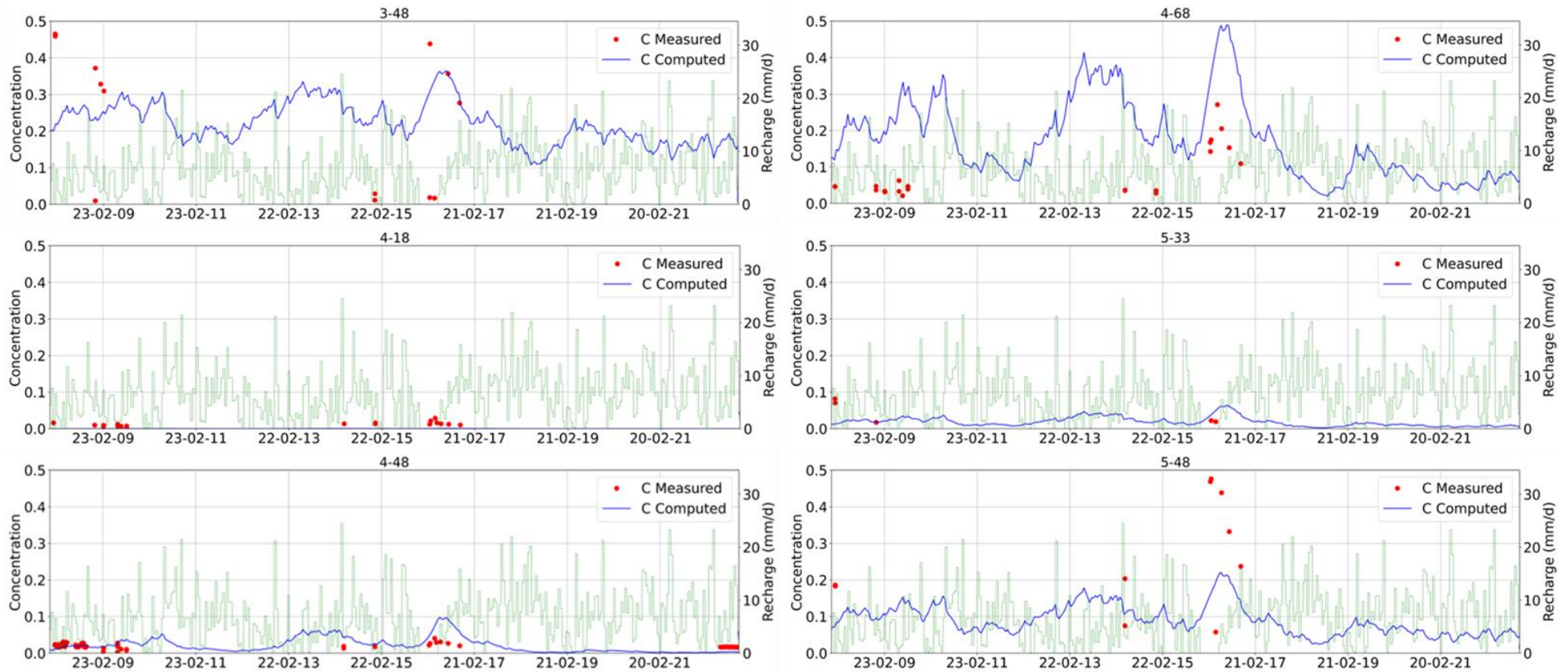


Figure 10-6: Calculated (blue line) and measured (red dots) normalized concentration at six multi-level observation wells (3-48, 4-18, 4-48, 4-68, 5-33, 5-48) from the calibrated Daily Transient Model.

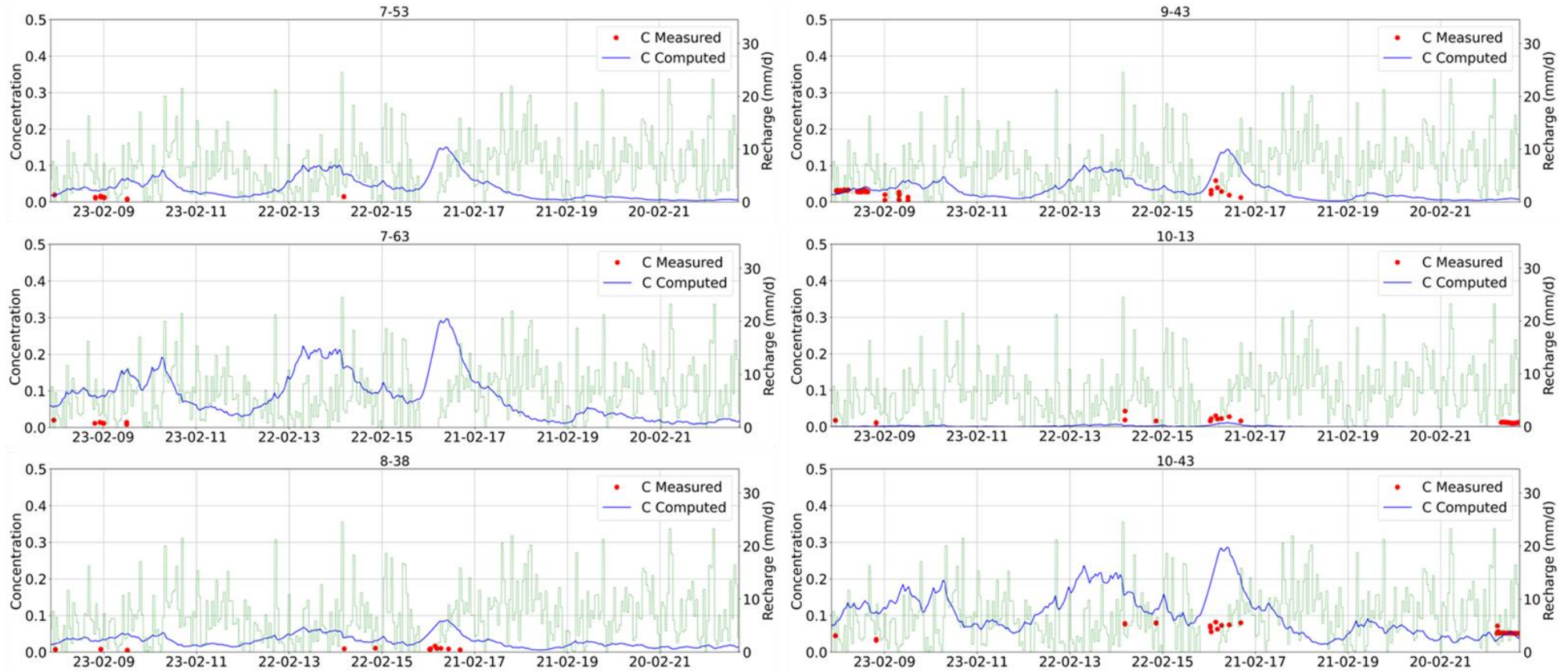


Figure 10-7: Calculated (blue line) and measured (red dots) normalized concentration at six multi-level observation wells (7-53, 7-63, 8-38, 9-43, 10-13, 10-43) from the calibrated Daily Transient Model.

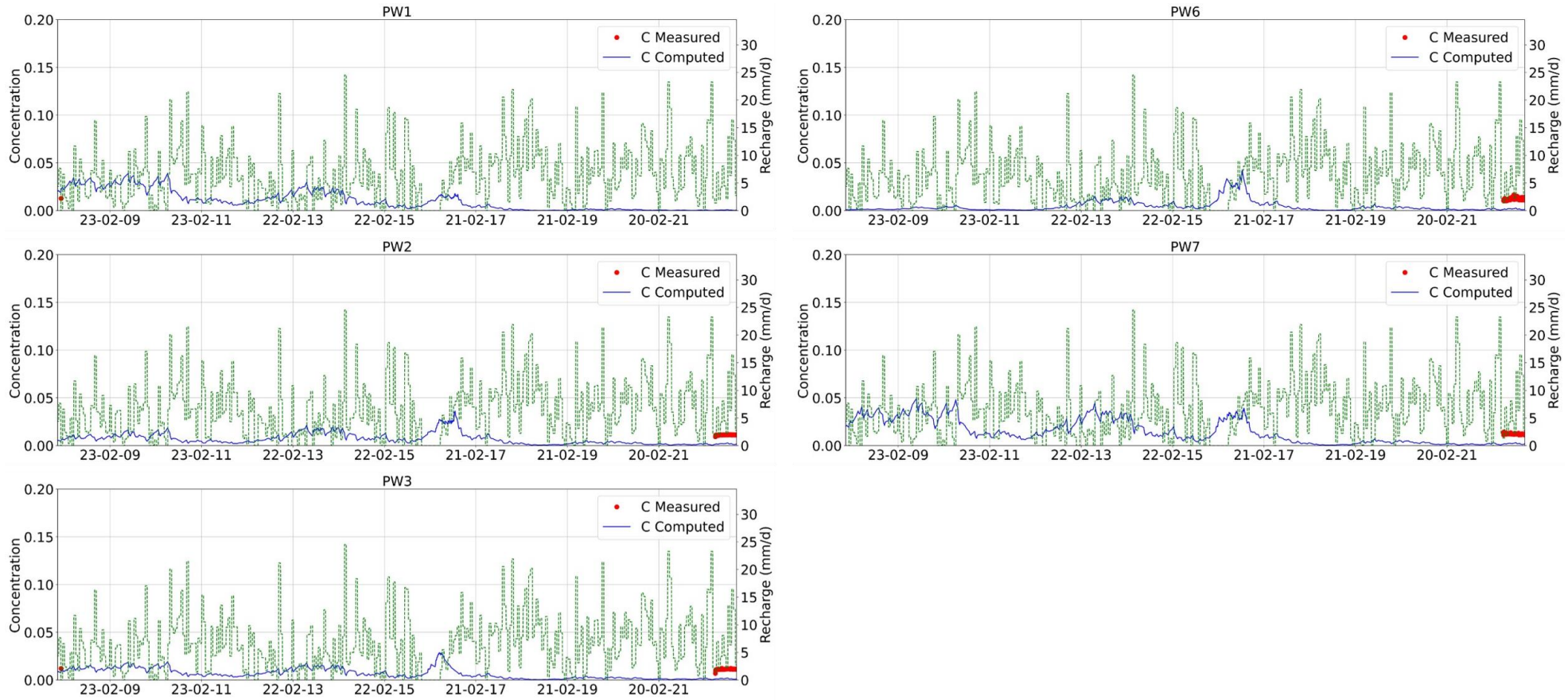


Figure 10-8: Calculated (blue line) and measured (red dots) normalized concentration at the pumping wells from the calibrated Daily Transient

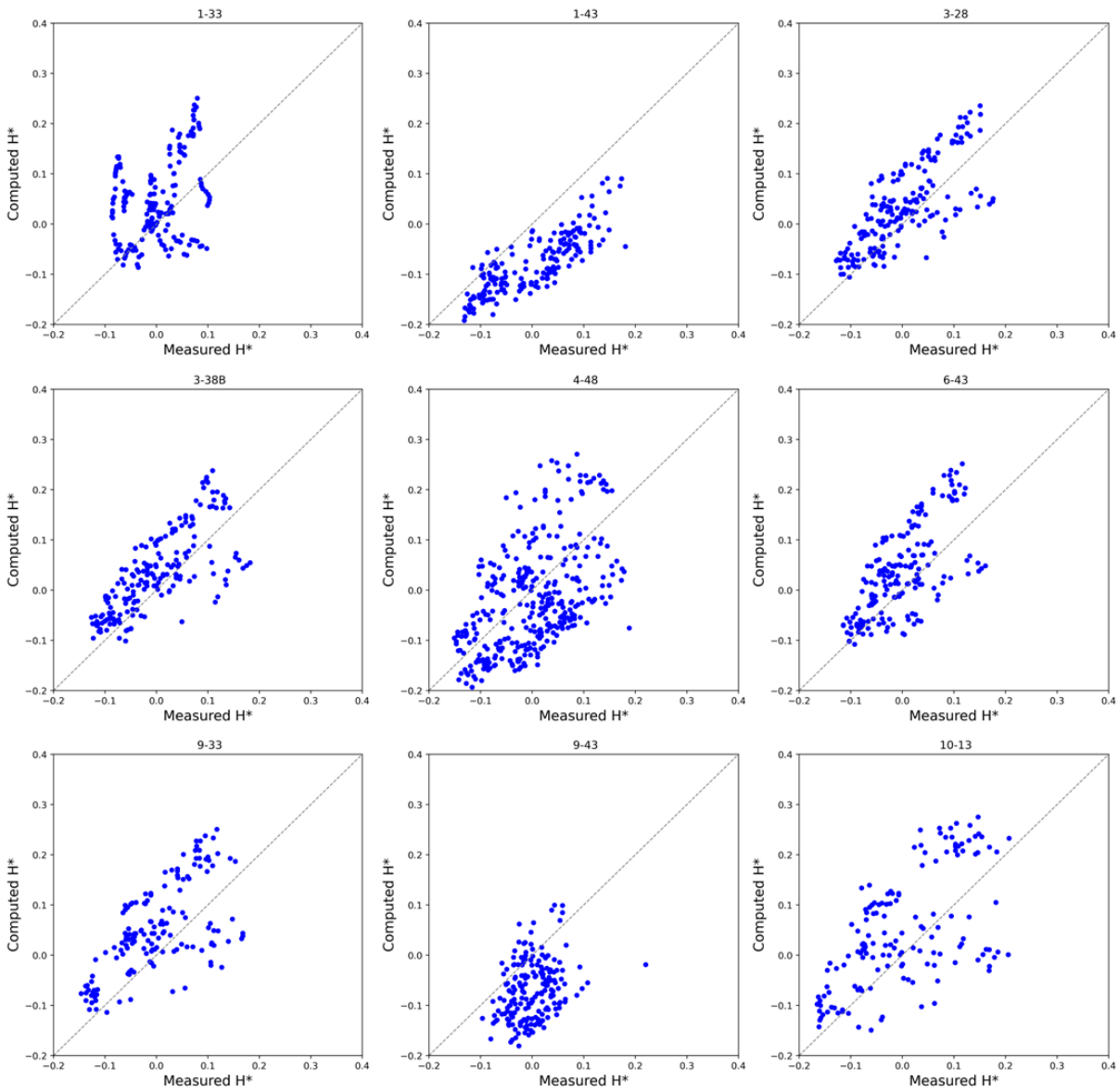


Figure 10-9: Calculated and measured normalized heads obtained from the calibration of the Daily Transient model.

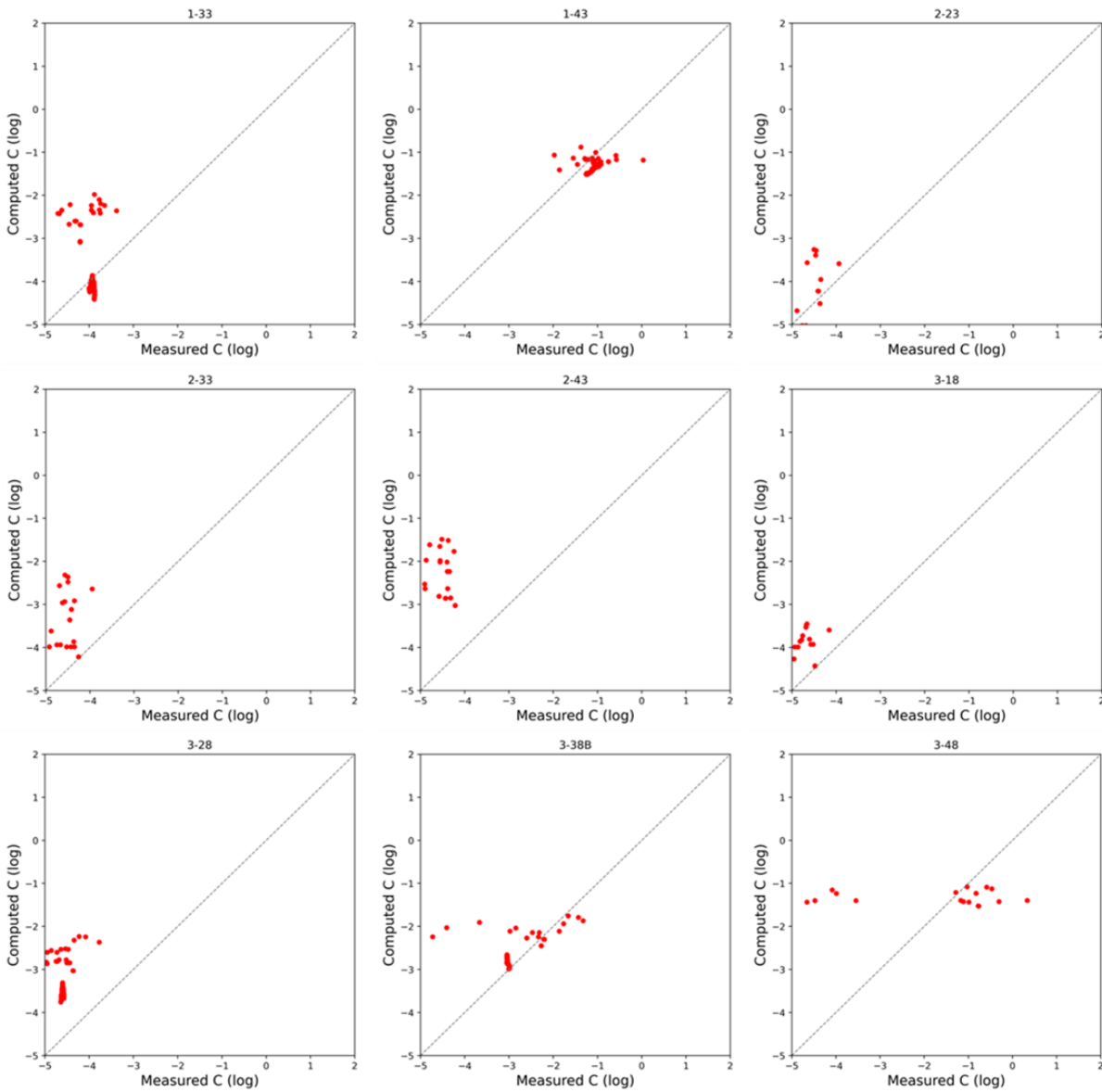


Figure 10-10: Calculated and measured concentrations obtained from the calibration of the Daily Transient model.

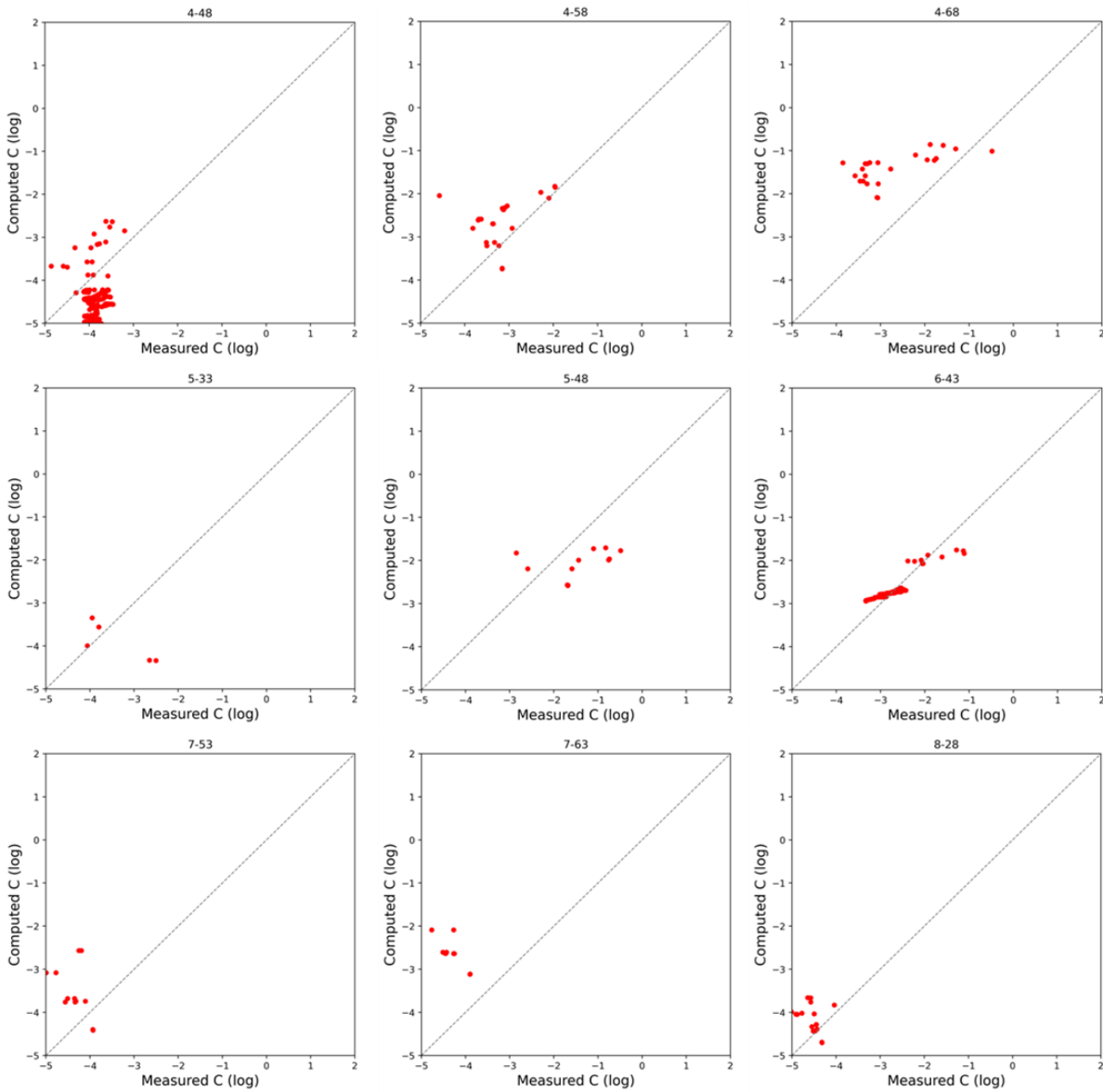


Figure 10-11: Calculated and measured concentrations obtained from the calibration of the Daily Transient model.

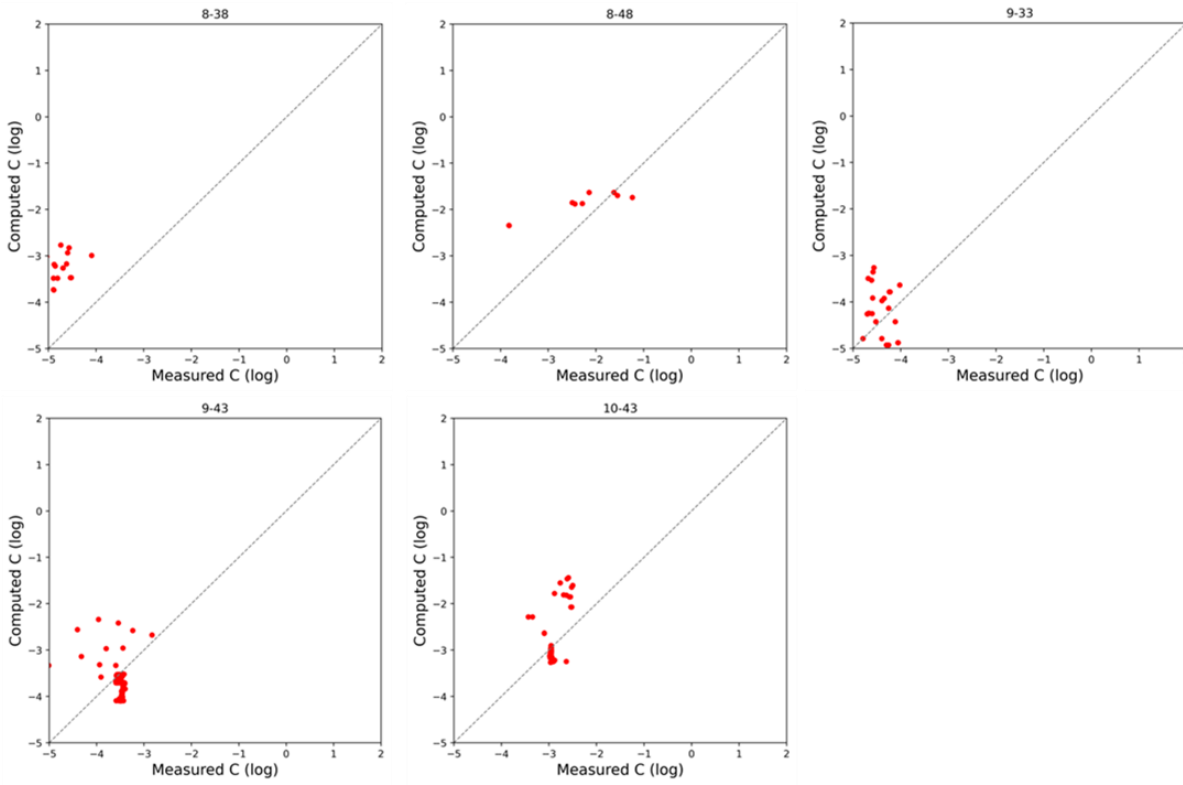


Figure 10-12: Calculated and measured concentrations obtained from the calibration of the Daily Transient model.